Charge transport in the assemblies of magnetic, non-magnetic and spin-cross over nano-structures

Suhail Usmani

Suhail Usmani. Charge transport in the assemblies of magnetic, non-magnetic and spin-cross over nano-structures. Physics [physics]. INSA de Toulouse, 2018. English. NNT : 2018ISAT0012 . tel-02917933

HAL Id: tel-02917933
https://theses.hal.science/tel-02917933

Submitted on 20 Aug 2020

THÈSE

En vue de l'obtention du

DOCTORAT DE L'UNIVERSITE DE TOULOUSE

Délivré par :

Institut National des Sciences Appliquées de Toulouse (INSA de Toulouse)

Présentée et soutenue par :

Suhail USMANI

Le vendredi 5 April 2018 *

Titre :

Charge transport in the assemblies of magnetic, non-magnetic and spin cross-over nano-structures

* Sous réserve d'acceptation du manuscrit de thèse

Ecole doctorale et discipline ou spécialité :
ED SDM : Nano-physique, nano-composants, nano-mesures

Unité de recherche :
Laboratoire de Physique et Chimie des Nano-Objets (LPCNO)

Directeurs de Thèse :
Julian CARREY

Jury :

Jean François DAYEN, *IPCMS, Strasbourg*	Rapporteur
Richard MATTANA, *CNRS, Thales*	Rapporteur
Hervé AUBIN, *ESPCI, Paris*	Examinateur
Myrtil KAHN, *LCC, Toulouse*	Examinateur
Gabor MOLNAR, *LCC, Toulouse*	Examinateur
Julian CARREY, *INSA, Toulouse*	Directeur de thèse
Marc RESPAUD, *INSA, Toulouse*	Invité
Simon TRICARD, *INSA, Toulouse*	Invité

Contents

Introduction

In 1959, the famous lecture by Richard Feynman titled "*There's plenty of room at the bottom*" provided an insight of what could be achieved by making "small materials" or so called nano-materials. After six decades, our capability of producing and exploiting these nano-materials has evolved tremendously. The second half of the last century has witnessed a revolution of downsizing the materials to nano- and sub-nano scale. However, it did not take too long to realize that materials at such a small scale behaved differently than their bulk counter-parts, and a large number of questions emerged, particularly about the magnetic and electronic properties of these materials. In the pursuit of the answers, research on these materials received tremendous amount of attention which, at the same time, led to the discovery of several novel phenomena.

One such phenomenon is Coulomb blockade, which was first observed experimentally in granular metallic nano-structures by Van Itterbeek *et al*. [1, 2] and then later explained by Gorter [3] on the basis of charging effect arising due to the small size of these nano-structures. Neugebauer and Webb proposed the theory of thermally activated charge transport mechanism in such granular materials which took into the account the charging energy; an important aspect of Coulomb blockade [4]. Later, a scaling law was proposed by Middleton and Wingreen to describe the current-voltage (*I-V)* curves in 1-D and 2-D assemblies of particles at null temperature [5], and was extended to finite temperatures by Parthasarathy *et al*. [6]. With time, the domain of Coulomb blockade expanded and it could be observed in large number of systems ranging from single particle device [7] to assemblies of particles [8].

Current research on Coulomb blockade is advancing to achieve several ultimate goals. One of the goals is to have better control over Coulomb blockade and find systems in which its tuning can be performed at room-temperature. In particular, chemically synthesized nanoparticles have offered the possibility of tuning Coulomb blockade by varying the physical parameters such as the particle size [9, 10], dimension of the assembly [11, 12], and substituents on the ligands [13]. At the *Laboratoire de physique et chimie des nano-objets* (LPCNO), previous work by Julien DUGAY has shown that inter-particles coupling can be regulated in assemblies of chemically synthesized Co particles by using alkyl ligands of different chain lengths. Control over these parameters not only allows to tune the Coulomb blockade but also provide the possibility to better understand its effects such as higher order tunneling mechanism e.g. co-tunneling. A portion of this thesis is dedicated to the study of Coulomb blockade in assemblies of nanoparticles where we shall use different parameters for its tuning at room-temperature.

Co-tunneling mechanism, in general, emerges at low temperatures due to the blockage of current as the thermal energy becomes insufficient to overcome charging energy [14-16]. In assemblies of magnetic nanoparticles, co-tunneling can significantly enhance the tunnel magnetoresistance [16-18]. However, the experimental studies on the co-tunneling enhanced magnetoresistance are only few. Black *et al*. first reported the tunnel magnetoresistance in chemically synthesized Co particles which could show amplitude up to 8% at low temperature, however, only sequential tunneling was observed in the reported assemblies [19]. At LPCNO, Reasmey TAN studied the magnetotransport properties of FeCo super-lattices which showed interesting properties such as high field magnetoresistance up to 3000%, hysteretic step jumps in the *I-V* characteristics in Coulomb blockade regime [20]. However, low field magnetoresistance remained masked by the high field magnetoresistance in these super-lattices. In the continuation of the work, Julien DUGAY observed the low field magnetoresistance in assemblies of Fe nanoparticles at the LPCNO [21]. These assemblies could show a tunnel magnetoresistance (TMR) amplitude of ~0.8% at low temperature, which vanished rapidly at higher temperatures. Despite the presence of magnetoresistance, it remained difficult to observe the effect of co-tunneling in these assemblies. It was sought that the quality of the particles (i.e. amorphous or crystalline, with or without impurities) can significantly affect the magnetoresistance in their assemblies. For example, high field magnetoresistance observed in FeCo super-lattice has been attributed to the presence of paramagnetic impurities within the barrier or at the surface of particles [22].

The chemistry team at LPCNO has recently upgraded the quality of FeCo particles with better chemical routes. The improved quality of these particles provided us the opportunity to study the TMR properties in their assemblies. In particular, we measured larger TMR amplitude than the one measured in particles synthesized in the laboratory so far, and could analyze their properties in the light of co-tunneling mechanism.

Apart from metallic nanoparticles, another class of materials known as spin cross-over (SCO) complexes displays particularly interesting properties. These complexes can show two magnetic states with a high and a low magnetic moment. The transition between these two states, often called spin-transition, can be brought about by external stimuli such as temperature, pressure, light, magnetic field, etc... Previously, at the *Laboratoire de chimie de coordination* (LCC) and LPCNO, it was shown that spin transition in these complexes can be accompanied by conductivity switching [23, 24]. However, the transport behavior in such complexes is often limited by their high resistivity. To counterfeit such problem, the chemistry teams at both laboratories have developed a synthesis procedure to chemically prepare mixed or hybrid materials of SCO complexes and metal nanoparticles. It was hypothesized that such hybrid materials could have an enhanced conductivity while maintaining switching behavior, and also that the presence of Coulomb blockade inside the assemblies might lead to interesting effect such as an enhancement of the contrast in the conductivity between the high- and the low-spin state. Experimental results on such hybrid structures are not abundant. So far, only one experimental study on a similar system reported that the effect of spin transition could be observed in the form of a minima in the resistance around room-temperature [25].

The work performed during this thesis focus on three main aspects. The first aspect is the room-temperature tuning of Coulomb blockade in assemblies of nanoparticles. Controlling Coulomb blockade is important as it can ultimately provide control over the temperature regimes where the higher order tunneling mechanism may prevail in an assembly. In this concern, systems that offer the possibility of tuning the Coulomb blockade at room-temperature are of particular interest. Assemblies of platinum nanoparticles were chosen for our study of Coulomb blockade. The small size of these particles (1.1 nm to 1.3 nm) permitted us to study and tune the Coulomb blockade at room-temperature. Several approaches were adopted for room-temperature tuning of Coulomb blockade. These approaches include: (i) tuning of inter-particle separation by coating the particles' surface with different alkyl chains, (ii) use of ligands with different dielectric constant that can affect the charging energy and Coulomb blockade, and (iii) using particles of different sizes to study its effect on Coulomb blockade.

The second aspect that remained in the focus of the thesis is the TMR in assemblies of magnetic nanoparticles, and the effects of co-tunneling mechanism at low temperatures. For this study, we used 10 nm in diameter $Fe_{50}Co_{50}$ nanoparticles coated with HDA/HCl. These particles have been synthesized by improved chemical routes compared to the particles used in LPCNO during previous studies, and showed higher TMR amplitude due to their better crystallinity.

The third aspect of the work of this thesis is to study the transport and magnetic behavior of SCO complex and its hybrid structure with metal nanoparticles. The system that we have chosen for our study of charge transport is a Fe (II) based triazole complex as well as its hybrid structure with platinum nanoparticles. The Fe (II) pure complex system is expected to show spin-transition near room-temperature which is desirable quality in many functional devices. The possibility of synthesizing hybrid structure where the spin cross-over complexes could interact with Pt nanoparticles provide an opportunity of improving the conductance of spin-cross over complexes with preserved spin transition.

Accordingly, this thesis is divided into four chapters. **Chapter 1** is dedicated to the state of the art of the research performed during the thesis. Chapter 1 is itself sub-divided into three parts. **Chapter 1.1** is dedicated to the state of the art of Coulomb blockade where the reader shall be introduced to the fundamental aspects of Coulomb blockade including some important phenomenological models and theories. **Chapter 1.2** shall be dedicated to the fundamental aspects of TMR where the relevant theories of TMR shall be discussed along with the effect of various parameters such a voltage and temperature. Besides, the TMR studies in assemblies of chemically synthesized nanoparticles shall also be presented. **Chapter 1.3** will provide the glimpse of research on spin cross-over complexes where the reader shall be introduced to the ligand field theory, thermally induced spin transition, and various charge transport experiments performed in assemblies of nano-structure spin crossover complexes showing the effects of spin transition on conductivity.

Chapter 2 of the thesis is dedicated to our studies performed on the Coulomb blockade in the assemblies of platinum nanoparticles. We shall briefly discuss the synthesis and characterization of particles showing the controllability over particles size, inter-particle distance and dielectric constant of the medium surrounding the particles. We shall then present the charge transport studies showing the effect of inter-particle distance on charging energy. Using conductive atomic force microscopy measurements, we shall show room-temperature tuning of Coulomb blockade showing the effect of dielectric constant and the particle size on the scaling exponent. Finally we shall enclose the chapter with a brief conclusion.

Chapter 3 shall be concerned with the studies of TMR phenomenon in the assemblies of FeCo nanoparticles prepared by dielectrophoresis and drop casting. We shall begin by a brief summary of synthesis and characterization of these particles and then present their magnetotransport properties. TMR in these assemblies, in the temperature range of 1.8 K to 300 K, shows an increase in amplitude with decreases in temperature. We shall interpret the temperature dependence in the light of co-tunneling mechanism which is observed to be the mode of transport in low temperature regime. The effect of voltage on TMR amplitude in the co-tunneling regime shall also be presented. Besides, we have observed high field magneto-resistance in our assemblies under low voltage and low temperature conditions that shall also be discussed. Finally, we shall conclude the results obtained on the assemblies of FeCo particles.

In **Chapter 4**, we shall present our studies on the spin cross-over complexes. After briefly presenting the synthesis and characterization of the pure complex and its hybrid structure with metal nanoparticles, we shall present the magnetic measurements performed on the pure Fe(II) complex confirming the spin transition in the presence of solvent. The effect of solvent on the spin transition shall also be. Similar magnetic measurements performed on the hybrid nano-structure of spin cross-over complex and metallic nanoparticles shall also be presented. In the later section we shall discuss the charge transport in pure complexes and hybrid structure followed by our interpretation of the different results obtained in charge transport measurements. At the end of the chapter, we shall briefly conclude our studies presented in this chapter

Finally, we shall enclose the thesis with a general conclusion of the research performed during the thesis as well as the future aspect of this work.

References: Introduction

[1] A. van Itterbeek and L. de Greve, "Measurements on the electrical resistivity of thin nickel films," *Experientia,* journal article vol. 3, no. 7, pp. 278-279, July 01 1947.

[2] R. Lambeir, A. Van Itterbeek, and G. J. Van Den Berg, "Measurements on the electrical resistivity of thin iron films at. Liquid helium temperatures," *Physica,* vol. 16, no. 11, pp. 907-914, 1950/12/01/ 1950.

[3] C. J. Gorter, "A possible explanation of the increase of the electrical resistance of thin metal films at low temperatures and small field strengths," *Physica,* vol. 17, no. 8, pp. 777-780, 1951/08/01/ 1951.

[4] C. A. Neugebauer and M. B. Webb, "Electrical Conduction Mechanism in Ultrathin, Evaporated Metal Films," *Journal of Applied Physics,* vol. 33, no. 1, pp. 74-82, 1962.

[5] A. A. Middleton and N. S. Wingreen, "Collective transport in arrays of small metallic dots," *Physical Review Letters,* vol. 71, no. 19, pp. 3198-3201, 11/08/ 1993.

[6] R. Parthasarathy, X. M. Lin, K. Elteto, T. F. Rosenbaum, and H. M. Jaeger, "Percolating through networks of random thresholds: finite temperature electron tunneling in metal nanocrystal arrays," (in eng), *Phys Rev Lett,* vol. 92, no. 7, p. 076801, Feb 20 2004.

[7] T. A. Fulton and G. J. Dolan, "Observation of single-electron charging effects in small tunnel junctions," *Physical Review Letters,* vol. 59, no. 1, pp. 109-112, 07/06/ 1987.

[8] T. Junno *et al.*, "Single-electron devices via controlled assembly of designed nanoparticles," *Microelectronic Engineering,* vol. 47, no. 1, pp. 179-183, 1999/06/01/ 1999.

[9] A. Zabet-Khosousi, Y. Suganuma, K. Lopata, P.-E. Trudeau, A.-A. Dhirani, and B. Statt, "Influence of Linker Molecules on Charge Transport through Self-Assembled Single-Nanoparticle Devices," *Physical Review Letters,* vol. 94, no. 9, p. 096801, 03/09/ 2005.

[10] A. J. Quinn *et al.*, "Manipulating the Charging Energy of Nanocrystal Arrays," *Small,* vol. 1, no. 6, pp. 613-618, 2005.

[11] C. Duan *et al.*, "Controllability of the Coulomb charging energy in close-packed nanoparticle arrays," *Nanoscale,* 10.1039/C3NR02334F vol. 5, no. 21, pp. 10258-10266, 2013.

[12] Y. Wang, C. Duan, L. Peng, and J. Liao, "Dimensionality-dependent charge transport in close-packed nanoparticle arrays: from 2D to 3D," *Scientific Reports,* Article vol. 4, p. 7565, 12/19/online 2014.

[13] G. L. Stansfield and P. J. Thomas, "Substituent Effects on Charge Transport in Films of Au Nanocrystals," *Journal of the American Chemical Society,* vol. 134, no. 29, pp. 11888-11891, 2012/07/25 2012.

[14] T. B. Tran, I. S. Beloborodov, X. M. Lin, T. P. Bigioni, V. M. Vinokur, and H. M. Jaeger, "Multiple Cotunneling in Large Quantum Dot Arrays," *Physical Review Letters,* vol. 95, no. 7, p. 076806, 08/12/ 2005.

[15] T. B. Tran, I. S. Beloborodov, J. Hu, X. M. Lin, T. F. Rosenbaum, and H. M. Jaeger, "Sequential tunneling and inelastic cotunneling in nanoparticle arrays," *Physical Review B,* vol. 78, no. 7, p. 075437, 08/26/ 2008.

[16] S. Mitani, S. Takahashi, K. Takanashi, K. Yakushiji, S. Maekawa, and H. Fujimori, "Enhanced Magnetoresistance in Insulating Granular Systems: Evidence for Higher-Order Tunneling," *Physical Review Letters,* vol. 81, no. 13, pp. 2799-2802, 09/28/ 1998.

[17] M. Pauly *et al.*, "Co-tunneling enhancement of the electrical response of nanoparticle networks," (in eng), *Small,* vol. 8, no. 1, pp. 108-15, Jan 9 2012.

[18] H. Kumar *et al.*, "Role of Coulomb blockade and spin-flip scattering in tunneling magnetoresistance of FeCo-Si-O nanogranular films," *Journal of Applied Physics,* vol. 109, no. 7, p. 073914, 2011/04/01 2011.

[19] C. T. Black, C. B. Murray, R. L. Sandstrom, and S. Sun, "Spin-dependent tunneling in self-assembled cobalt-nanocrystal superlattices," (in eng), *Science,* vol. 290, no. 5494, pp. 1131-4, Nov 10 2000.

[20] R. P. Tan, J. Carrey, M. Respaud, C. Desvaux, P. Renaud, and B. Chaudret, "3000% high-field magnetoresistance in super-lattices of CoFe nanoparticles," *Journal of Magnetism and Magnetic Materials,* vol. 320, no. 6, pp. L55-L59, 2008/03/01/ 2008.

[21] J. Dugay *et al.*, "Room-Temperature Tunnel Magnetoresistance in Self-Assembled Chemically Synthesized Metallic Iron Nanoparticles," *Nano Letters,* vol. 11, no. 12, pp. 5128-5134, 2011/12/14 2011.

[22] R. P. Tan, J. Carrey, and M. Respaud, "Voltage and temperature dependence of high-field magnetoresistance in arrays of magnetic nanoparticles," *Journal of Applied Physics,* vol. 104, no. 2, p. 023908, 2008/07/15 2008.

[23] A. Rotaru *et al.*, "Nano-electromanipulation of Spin Crossover Nanorods: Towards Switchable Nanoelectronic Devices," *Advanced Materials,* vol. 25, no. 12, pp. 1745-1749, 2013.

[24] L. Salmon *et al.*, "Re-investigation of the spin crossover phenomenon in the ferrous complex [Fe(HB(pz)3)2]," *New Journal of Chemistry,* 10.1039/B902811K vol. 33, no. 6, pp. 1283-1289, 2009.

[25] E. J. Devid *et al.*, "Spin Transition in Arrays of Gold Nanoparticles and Spin Crossover Molecules," *ACS Nano,* vol. 9, no. 4, pp. 4496-4507, 2015/04/28 2015.

Chapter 1: State of the Art

1.1 Coulomb blockade

1.1.1 Introduction

Early studies related to Coulomb blockade can be traced back to late 1940s when experimental studies by Van Itterbeek *et al*. [1, 2] showed that electrical resistance of certain granular metallic films increases significantly at low temperature and show deviation from Ohm's law. At low temperature, resistance of these films was found to be voltage dependent and showed significantly high values at low bias voltage. In 1951, Gorter [3] provided first plausible explanation for this phenomenon based on simple electrostatics while, a decade later, Neugebauer and Webb [4] used a combination of quantum and classical approach to explain the mechanism of electron transport in such films. Despite these early studies, Coulomb blockade could not gain much attention until lithography came into trend in 1980s. With the help of lithography, it became possible to observe Coulomb blockade in a single metallic island [5] rather than ensemble of metallic grains. This facilitated the observation of Coulomb blockade at room temperature [6] and attracted numerous experimental and theoretical studies. In present time, Coulomb blockade holds great importance in modern electronic devices and remains a topic of interest in various types of nanostructures [7-9]. In particular, arrays of chemically synthesized nanoparticles have been extensively used to investigate the Coulomb blockade as they offer various possible ways to tune the Coulomb blockade and other charge transport properties [10, 11].

In this chapter, we shall discuss various aspects of Coulomb blockade in nanoparticles arrays. To familiarize ourselves with the concept of Coulomb blockade, we shall begin with a simple case of an isolated metallic particle and then move our attention towards the arrays of nanoparticles. We shall present the relevant studies and models that would provide an insight to the charge transport mechanism in nanoparticle arrays. As we shall see through the course of this chapter, the essence of Coulomb blockade lies in the charging energy which depends on several physical parameters. We shall also discuss the role of these parameters in determining the charging energy.

1.1.2 Conceptual insight

1.1.2 (a) Charging effect

In order to understand the physics behind Coulomb blockade in simple terms, let us consider a single spherical metallic particle of diameter d, connected to two adjoining electrodes via a thin dielectric of relative permittivity ε_r as shown in Figure 1.1.1(a). If a voltage drop V is applied across the electrodes then the current in the device would not rise as in case of a simple ohmic-conductor. Instead, as reported in numerous experimental [12-16] studies, the current would remain blocked up to a certain minimum voltage before it starts to rise as shown in the sketch of current-voltage curve in Figure 1.1.1(b).

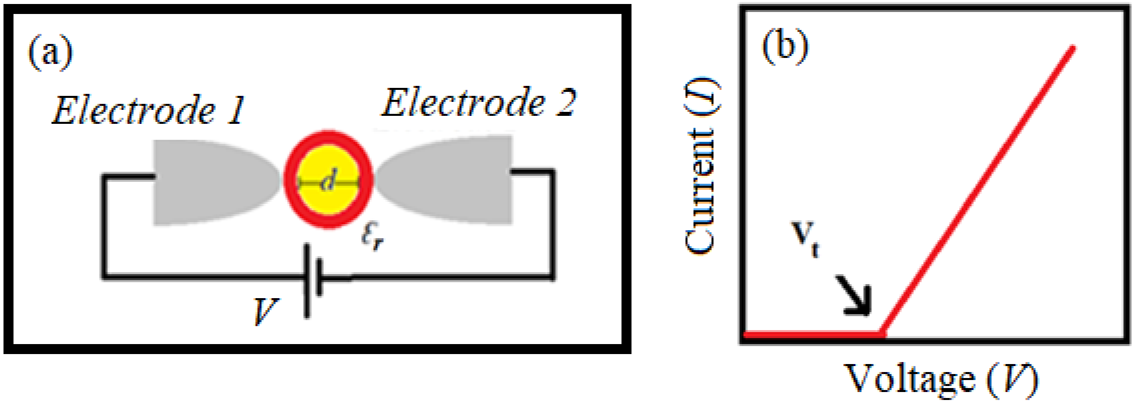

Figure 1.1.1: (a) Schematic diagram of a single particle device showing electrodes connected to the particle via a dielectric layer and (b) a typical *I-V* curve sketch for the device showing the blockage of current near zero bias.

A primitive explanation for such a behavior comes from simple electrostatics which considers the metallic particle as a capacitor with capacitance *C*, given by

$$C = 2\pi\varepsilon_o\varepsilon_r d \qquad 1.1(a)$$

where ε_o is the vacuum permittivity. If the diameter of particle is considerably small, its capacitance would be extremely low. As a result, charging it with a single electron would cost certain amount of energy known as charging energy (E_c) given as

$$E_c = \frac{e^2}{2C} = \frac{e^2}{4\pi\varepsilon_o\varepsilon_r d} \qquad 1.1(b)$$

where *e* is the electronic charge. Now, the energy E_c has to be provided by some external means in order to transfer an electron from the electrode to the particle. Most often, E_c is compensated by thermal energy provided that k_bT is greater than E_c. However, at low temperatures, E_c could be much higher than the thermal energy and it becomes impossible to add/remove an electron from the particle near zero bias voltage. As a result, the device resistance becomes significantly high and electron transport is blocked. This blocking of transport is actually referred as **Coulomb blockade**. The blockage persists up to a certain **threshold voltage V_t** (= *e/2C*) which is equivalent to E_c in terms of energy. On increasing the voltage above V_t, the conduction begins as the electron can now be transferred to the particle. The voltage interval, from $-V_t$ to V_t, where transport is blocked is called **Coulomb gap**.

1.1.2 (b) Orthodox theory

Coulomb blockade can be also understood in terms of orthodox theory which takes into account not only the charging energy but also the tunneling process which is the preferential mode of electron transfer at particle-electrode junction. In this theoretical model, a particle-electrode junction is treated as a parallel combination of a resistor (R) and a capacitor (C). Thus, the equivalent circuit of the considered device can be redrawn as shown in Figure 1.1.2.

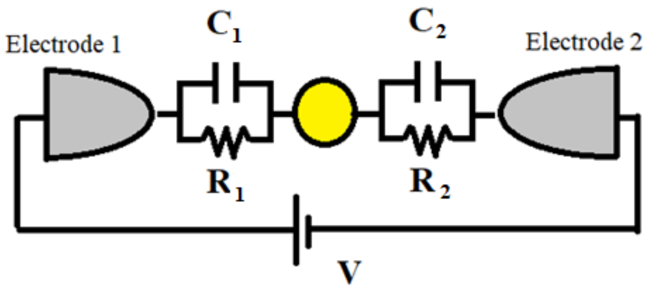

Figure 1.1.2: An equivalent circuit of a single particle device showing each particle-electrode junction as a parallel combination of a resistor and a capacitor.

The two components of the equivalent junction (i.e capacitor and resistor) play different roles in the conduction process. The voltage drop, V_j, across a junction j (=1,2) is determined by the capacitor C_j at that junction by the following equation:

$$V = \frac{C_1 C_2 V}{C_j C_\Sigma}, \qquad 1.1\,(c)$$

where C_1 and C_2 are the respective capacitances of junctions 1 and 2 while C_Σ being the sum of both. On the other hand, the rate of electron tunneling (Γ_j) at a junction j, for a given temperature and voltage, is given in terms of resistance R_j at that junction by the following equation:

$$\Gamma_j = \frac{-\Delta E_j}{e^2 R_j} \frac{1}{1 - \exp(\Delta E_j / k_b T)}, \qquad 1.1(d)$$

where ΔE_j is the change in energy at junction j before and after the tunneling of electron, and can be expressed as

$$\Delta E_j = -eV + E_c \qquad 1.1(e)$$

From equation 1.1(d), it can be deduced that at 0 K (i.e. no contribution from thermal energy) the tunneling rate would follow the condition given by equation 1.1(f).

$$\Gamma_j(0\,K) = \begin{cases} 0 \quad if\;\; \Delta E_j \geq 0 \\ \frac{-\Delta E_j}{e^2 R_j} \;\; if\;\; \Delta E_j < 0 \end{cases} \qquad 1.1(f)$$

Thus, a non-zero tunneling rate would exist only when $\Delta E_j < 0$. If we assume that both junctions are symmetric (i.e $C_1 = C_2$ and $R_1 = R_2$) and no initial charge was possessed by the particle, then from equation 1.1(f), it can be interpreted that a non-zero current would exist only when $V > 2E_c/e$, which is actually the threshold voltage (V_t) as discussed previously.

Most experimental results can be explained using orthodox approach while in some cases it can at least describe the quantitative behavior of the device. In arrays of particles, low temperature charge transport may occur by co-tunneling mechanism. An extended version of orthodox theory for such a mechanism is proposed by Averin and Nazarov [17]. More complicated version of orthodox theory, suitable for various types of systems, have been also reported [18-20].

1.1.2 (c) Conditions for Coulomb blockade

A single particle device may or may not show the Coulomb blockade behavior depending on certain conditions. The two main criteria that must be satisfied in order to observe Coulomb blockade in a device are as follows:

(a) The **charging energy** of the metallic island should be greater than thermal energy.

$$E_c >> k_b T \qquad 1.1(g)$$

A typical particle of diameter 10 nm, surrounded by a medium with relative permittivity 3.5, would have a charging energy of approximately 40 meV, while the available thermal energy at room temperature is roughly 25 meV. In order to observe a clear threshold voltage in I-V curves, the device should be cooled down. Some room-temperature devices which work on the principle of Coulomb blockade may require E_c to be as high as 100 k_bT at room temperature [21]. Such a condition has been satisfied by using particle of diameter less than 1 nm [22].

(b) The **tunneling resistance** of the dielectric should be greater than the resistance quantum.

$$R_t \gg h/e^2 \qquad 1.1(h)$$

The dielectric medium acts as a barrier for the charge. A tunneling resistance, R_t, higher than quantum resistance (h/e^2 = 25 kΩ) ensures that the charge is well quantized on the island. R_t lower than this value would result in increased coupling between the island and the electrodes, leading to leakage of charge and subsequent disappearing of Coulomb blockade. On the other hand, a very high value of R_t can make it difficult to measure the current in the device.

1.1.3 Coulomb blockade in arrays of nanoparticles

We have seen in previous section that Coulomb blockade can be observed in a single particle device. However, for practical purposes, fabrication of a single-particle device is a delicate task. Moreover, it requires a particle of diameter less than 1 nm in order to observe Coulomb blockade at room-temperature, thereby, rendering the device highly sensitive to quantum noise [23]. For these reasons, arrays of nanoparticles are often regarded as an alternate solution since they are much simpler to fabricate. The other advantage of an array over single particle device is the distribution of the applied bias over several nanoparticles junctions which results in the higher threshold voltage of the device [24, 25]. Besides, as we shall discuss later, 2D and 3D arrays of particles show much steeper rise in current above the threshold voltage compared to a single particle device. This results in high efficiency of the arrays outside the Coulomb gap.

As the electron transfer in an array occur via multi-junctions, the physics behind Coulomb blockade becomes rather complicated. Numerous factors such as size distribution of particles, inter-particle coupling, number of nearest neighbors, and dimensionality of the array can significantly influence electron transport and Coulomb blockade in arrays of particles. In the next two sub-sections, we shall present some relevant theoretical and experimental studies which have established the fundamental relationships (i.e. Current-Voltage and Resistance-Temperature) in the arrays of particles.

1.1.3 (a) Current -Voltage relationship

The *I*-*V* curve for an array of particles shows strong non-linearity and a threshold voltage similar to that of a single particle device when charging energy is higher than the thermal energy. In order to obtain *I*-*V* relationship in 1D and 2D arrays of metallic particles, Middleton and Wingreen [25] proposed a model whereby particles in an array are assumed to be linked with neighboring particles through capacitors as shown in the sketch [see Figure 1.1.3(a)]. In such an array, particles would be weakly coupled to each other, nevertheless charges could still transfer between the neighboring particles. Based on this assumption, a scaling law has been deduced for such an assembly which, at absolute zero temperature, relates the current-voltage by the following expression:

$$I \sim (V/V_t - 1))^{\xi} \qquad 1.1(i)$$

where, V_t is the threshold voltage and ξ is the scaling exponent.

Equation $1.1(i)$ is often called as Middleton-Wingreen (M-W) equation or scaling law. Experimental results [26-28] are often explained in the light of M-W equation while it remains the starting point for many simulation studies [29-31]. As evident from the equation$1.1(i)$, *I*-*V* relationship in nanoparticles arrays is largely determined by two parameters i.e. V_t and ξ. These two key factors significantly influence the conductance of an array and deserve a more detailed discussion. We discuss these factors in the subsequent sections.

(i) Threshold voltage

Threshold voltage itself depends on certain parameters. The two main factors that influence the threshold voltage in an array are temperature and the array size. We shall discuss the effect of these two parameters in the following sections.

Effect of array size: To understand the dependency of threshold voltage on array size, we consider the same system as described above where particles are capacitively coupled in an array [Figure 1.1.3(a)]. In such an array, for an electron to move from one electrode to another, it has to pass through several particles in a stepwise fashion. At each step, it requires an increment ΔV in external applied potential to advance in forward direction. Meanwhile, the current would remain blocked until the electron reaches to the other electrode. If it takes a total of N steps to span the inter-electrode distance, then V_t would be given as

$$V_t = \alpha N \Delta V \tag{1.1(j)}$$

where α is a constant that that depends on the quenched charge density stored in the array [24, 25]. It is obvious from equation 1.1(j) that an array with large size would possess a high V_t due to increase in N. In an ideal case, where all the particles are of the same size, and the array is free of any sort of defect, one expects N to be equal to the number of particles in the shortest path between the electrodes. Thus, V_t should vary rather linearly with number of particles. On the other hand, when defects and structural disorders are present in the array, electron transfer between the electrodes takes place via random paths due to which V_t may not show a linear dependency on N.

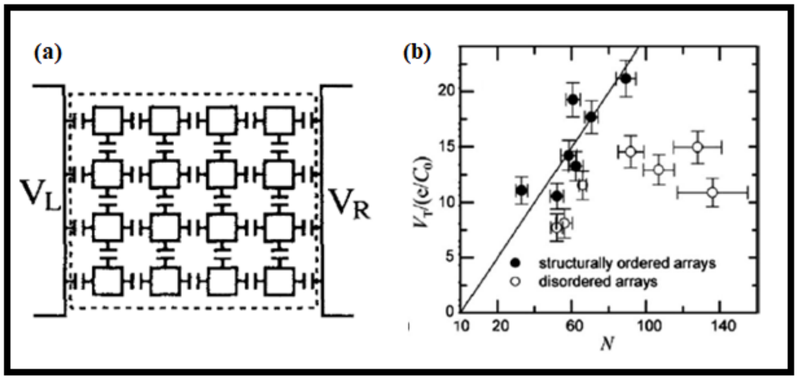

Figure 1.1.3: (a) A schematic representation of metallic particles in an array coupled through capacitors in series and parallel and (b) Variation of threshold voltage with number of particles in ordered and disordered assemblies showing a linear trend and no trend respectively:[(a): References [25] and (b): References [32]].

Parthasarathy *et al.* [32] succeeded to produce void filled monolayer and highly structured monolayers of Au nanoparticles by controlling the size of ligands. Experimental studies on these arrays showed that, indeed, ordered arrays exhibit an increasing trend in V_t with increase in number of particles between the electrodes whereas no visible trend was observed for disordered arrays as shown in Figure 1.1.3(b).

Effect of temperature: Apart from the array size, temperature can also significantly affect V_t. Parthasarathy *et al.* [24] extended the model of Middleton and Wingreen to finite temperatures. Their simulation results showed that V_t decreases with increase in temperature and may vanish completely at higher temperatures. Indeed, their experimental study on weakly coupled 2D Au nanoparticles array showed a cross-over temperature T^* such that:

i) For $T < T^*$, a clear threshold voltage is observed in *I-V* curves demonstrating a strong Coulomb blockade. Below T^*, threshold voltage continuously shifts to a lower value as the temperature increases. As a matter of fact, if this shift (V_{shift} (T)) is removed then the all the *I-V* curves below T^* could be superimposed over each other to form one master curve as shown in Figure 1.1.4(a) and (b). Thus threshold voltage at any temperature T can be related to threshold voltage at 0 K by the expression

$$V_t(T) = V_t(0) + V_{shift}(T) \qquad 1.1(k)$$

ii) For T = T*, threshold voltage first reaches zero and consequently the Coulomb blockade vanishes. This can be formulated as

$$V_{shift}(T*) = V_t(0) \qquad 1.1(l)$$

iii) For $T > T^*$, threshold voltage vanishes and a non-zero differential conductance exist even at zero bias [inset in Figure 1.1.4(a)]. As a result the *I-V* curves do not superimpose at low voltages. However, at higher voltages the curves can still be superimposed.

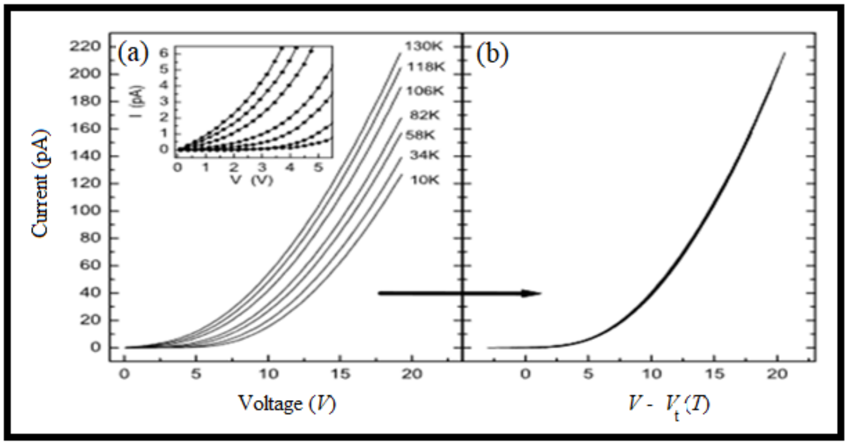

Figure 1.1.4: (a) *I-V* curves for weakly coupled Au nanoparticles 2D assembly at different temperatures showing variation in threshold voltage with temperature while the inset show non-zero differential conductance near zero bias at high temperatures . (b) Master curve obtained after superimposing all the *I-V* curves below T^*. [(a): Reference 25 and (b)]

The temperature dependency of V_t can be understood with percolation based model [24]. According to this model, at a finite temperature *T*, a fraction of junctions in the array can overcome the threshold voltage due to thermal fluctuation. As the temperature increases, the fraction of such junctions also increases eventually spanning the whole array. This results in a complete vanishing of V_t and an onset of Arrehenius behavior at zero bias voltage. A linear decrease in V_t has been reported by Drndic *et al*. [33] in PbSe array as shown in Figure 1.1.5(a).

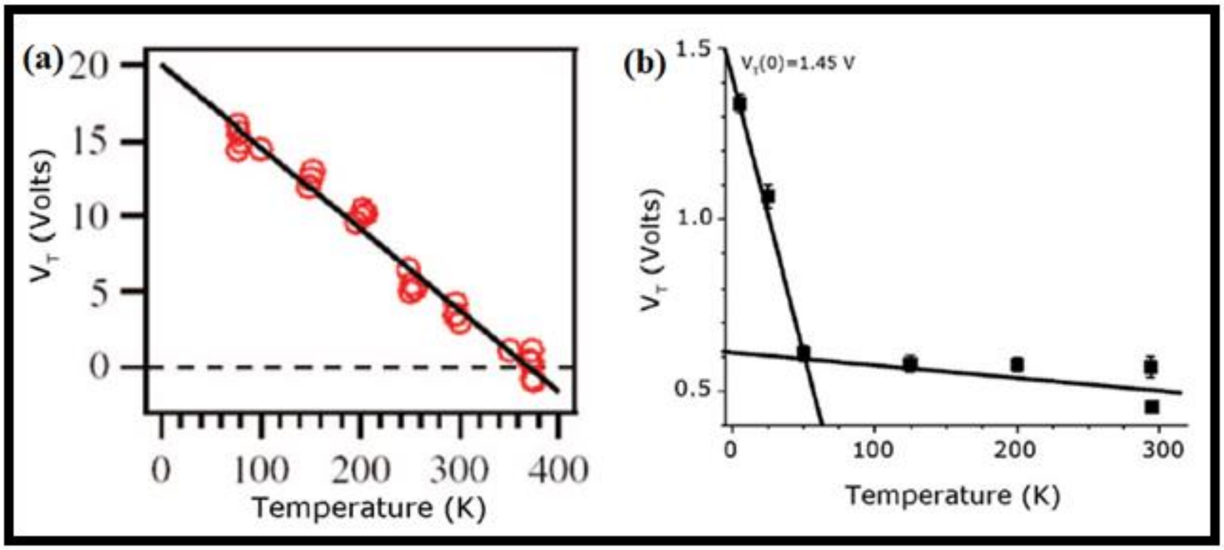

Figure 1.1.5: (a) Threshold voltage versus temperature plot for PbSe arrays showing a linear decrease in V_t with increase in temperature. (b) A non-linear decrease of V_t in quasi 1D Au nanoparticle array. [(a): References [33] and (b): Reference [28]]

Recent experimental studies have shown that a non-linear decrease in V_t could also be obtained in quasi 1D arrays of gold nanoparticles as shown in Figure 1.1.5(b). This non-linear variation is attributed to the structure of the array which has charge trapping sites where distributions of trapped charges vary with temperature resulting in a non-linear variation of V_t [28].

(ii) Scaling exponent ξ

Effect of dimension: The rise of current above threshold voltage depends on the nature of the branching of the percolation paths within the array which, in turn, depends on its dimensionality. In 1D arrays, current has essentially a single path to flow between the electrodes whereas in higher dimension arrays, percolation between the layers can occur and current flows through less resistive paths. This is taken into the account by the exponential ξ in M-W equation. The analytical values reported for ξ are 1 and 5/3 for 1D and 2D arrays respectively [25]. For 2D arrays, a broad spectrum varying from 5/3 to 4 has been reported [26, 27, 32]. This disagreement in the values of ξ may arise from the imperfection in the arrays or presence of more than one layer.

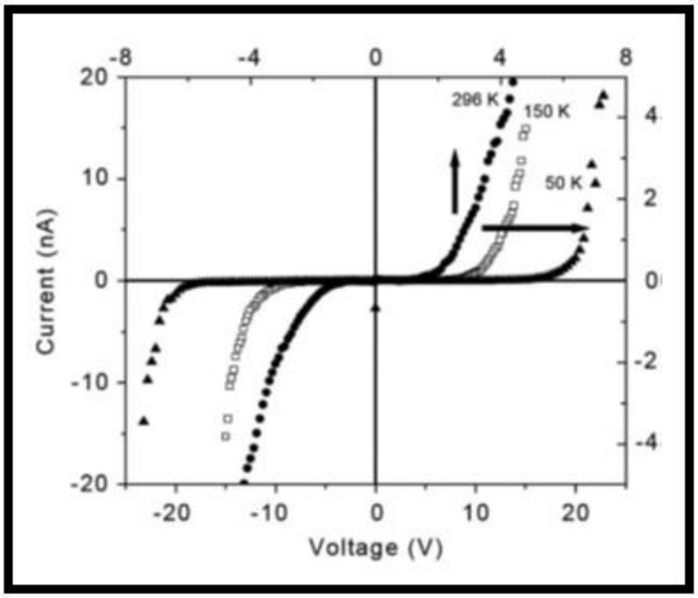

Figure 1.1.6: I-V curves for quasi 1-D CdS nanoparticles array showing different steepness of slope beyond threshold while the normalized current voltage beyond threshold show different values of ξ. [Reference [11]]

Effect of temperature: In most experimental studies and simulations, ξ is found to be independent of temperature. However, recent studies on necklace shape quasi 1D arrays of CdS nanoparticle have shown temperature dependent ξ as shown in Figure 1.1.6 [Reference [11]].
.

1.1.3 (b) Resistance - temperature relationship

In an array of nanoparticle, the variation of the resistance with temperature can be described by thermal activation theory proposed by Neugebauer and Webb [4]. As per the theory, the conduction process consists of two steps which are

(a) **Creation of charge carriers** which occur by transfer of an electron from one neutral particle to another neutral particle. This is an activated process and requires energy.. At any given temperature the equilibrium concentration (n) of charge carriers can be given as

$$n = N\mathrm{e}^{-E_a/k_bT} \qquad 1.1(m)$$

where N is the total number of particle in an array and E_a is the effective activation energy require to transfer a charge from one neutral nanoparticle to another neutral nanoparticle.

(b) **Drifting of charge carriers** from one charged particle to another neutral particle in the presence of an applied field. This is not considered as an activated process as no significant increase in energy takes place. However, this step is responsible for the conduction due to rapid transfer of charge carriers among the particles.

Based on above two points, Neugebauer and Webb deduced an expression of resistance in terms of product of charge carriers and their velocity in the applied field which, in its simplest form, can be expressed as

$$R = R_o \exp(E_a/k_bT) \qquad 1.1(n)$$

where R_o is the intrinsic resistance of the array. This relation is found to be true for most assemblies of particles, in particular at high-temperature regimes. Duean et. al. [34] have observed such a relation to be valid for assemblies of gold nanoparticles with different particle sizes as shown in Figure 1.1.7.

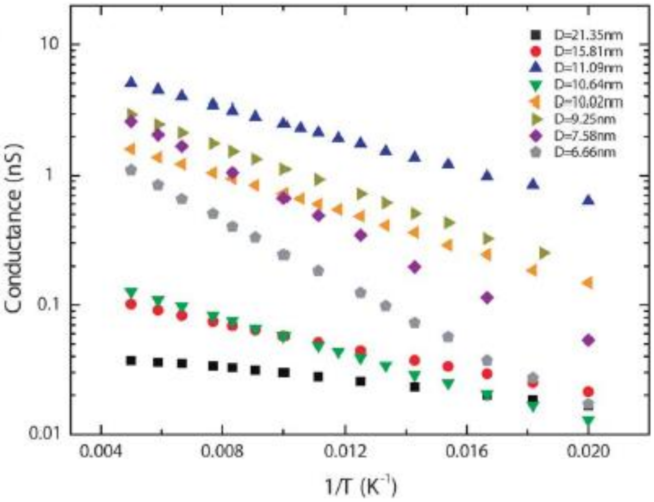

Figure 1.1.7: Log scale variation of conductance with 1/T for assemblies of gold nanoparticles of different sizes.

Note that the resistance of an array is largely determined by the ratio of activation energy to the thermal energy. Since charging energy can be considered constant for a given array, it is mainly temperature that governs the resistance.

Several experimental studies have shown deviation from the inverse temperature relationship. Instead, $T^{-1/2}$ could be followed due to the higher order charge transport mechanism [35]. Due to the discrepancies, a general resistance-temperature relationship can be written as

$$R = A \exp(E_a/k_bT)^{\alpha} \qquad 1.1(n)$$

where the value of α could be 1 or 0.5 depending on the mechanism of transport in the assembly.

1.1.4 Charging Energy: A Tool to tune Coulomb blockade

Tuning of Coulomb blockade in NPs arrays is of great interest for their application in electronic devices. Since the transport in arrays is mainly governed by charging energy, it has become the theme of numerous studies to manipulate the charging and use it as a tool to tune the Coulomb blockade. Various routes have been demonstrated where charging energy is tailored by controlled variation of one or more physical parameter of the array or of its constituents. These parameters include size of the particle, dimension of assembly, inter-particle separation, inter-particle coupling, number of nearest neighbor, dielectric material etc.

Different approaches have been used to determine the charging energy of nanoparticle arrays as well. However, due to its complex nature, discrepancies exit between these methods. While one approach could be well suited for one type of assembly, it might not provide a decent estimate for others. Some of the common approaches used to obtain charging energy of a nanoparticle array which are as follows:

1) **Isolated particle approach**

   In this method, the charging energy of an isolated single nanoparticle is considered. Here, only the self-capacitance of the particles is taken into account while the capacitances between the neighboring particles are neglected. Thus charging energy is simply given by

   $$E_c = \frac{e^2}{2C} = \frac{e^2}{4\pi\varepsilon_o\varepsilon_r d} \qquad 1.1(o)$$

   where d is the diameter of the nanoparticle, ε_r is the dielectric constant of the surrounding medium and ε_o the permittivity of the free space. Since the capacitance between the neighboring nanoparticles is ignored, the charging energy obtained by this method is overestimated. Though not very precise, this method can be quite handy for quick estimation of charging energy.

2) **Using Abeles model**

   Most suitable for 2D assemblies, this approach takes into account the contribution of inter-particle capacitance to the charging energy by considering the surrounding particles as a concentric metal layer. The expression of charging energy is given as

   $$E_c = \frac{e^2}{2C} = \frac{e^2 s}{4\pi\varepsilon_o\varepsilon_r d(d+s)} \qquad 1.1(p)$$

   where s is the edge to edge distance between the two neighboring particles. Since, the neighboring particles are replaced by an infinite metallic layer, this method overestimates the mutual capacitance between the particles, consequently the obtained charging energy is lower.

3) **Using Laikhtman model**

This can be considered as the improvised version of method 2. In this model, the total capacitance of the particle (C_Σ) in an array is defined as the sum of self-capacitance (C_{self}) and pairwise capacitance (C_{NN}) with all the neighboring particles which can be formulated as

$$E_c = \frac{e^2}{2\,C_\Sigma}$$

where,

$$C_\Sigma = 2N\pi\varepsilon_o\varepsilon_r r \ln\left(1 + \frac{2r}{s}\right) \qquad 1.1(q)$$

where, *N* is the number of nearest neighbor.

1.1.4 (a) Effect of Nanoparticle size

We have discussed previously that for an isolated metallic particle, an increase in size increases the self-capacitance of the particle thus decreasing its charging energy. However, for an array of fixed dimension and number of particles, size of the particle not only affects its self-capacitance but also the inter-particle capacitance which can significantly alter the charging energy. For a 2D assembly, relation between charging energy (*E*$_c$) and diameter (*D*) of a particle has been established by Abeles *et al*. [36]. Originally, the relation was established for granular film with random shape particle as shown in Figure 1.1.8 (a), nevertheless, it holds good for any 2D arrays. The proposed model assumes that the particle is perfectly spherical and replaces the surrounding particles by a continuous metallic layer as shown in Figure 1.1.8 (b).

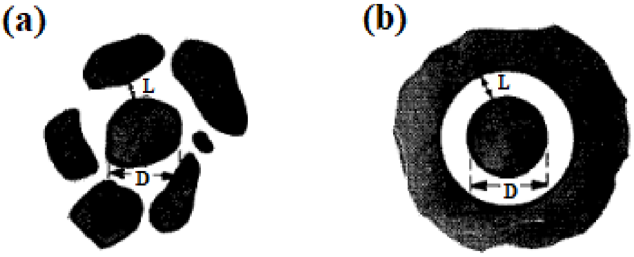

Figure 1.1.8: (a) Actual configuration of a metallic particle surrounded by its neighbors in a 2D array (b) Assumed configuration of the array where neighbors are replaced by continuous metal sheet. Reference [36].

Using the elementary electrostatic theory for the assumed configuration, the relation between the particle diameter (D) and charging energy (E_c) is found to be

$$E_c = (1/2)\, e^2 \frac{e^2}{4\pi\epsilon_o\epsilon_r}\ \left[r^{-1} - (r+s)^{-1}\right] \tag{1.1 (r)}$$

Duan *et al*.[34] have compared different methods used to extract the value of charging energy for assemblies of gold nanoparticles of different sizes as shown in Figure 1.1.9. As the size of the particle decreases, the charging energy increases. However, as mentioned before, they found overestimated value of charging energy by adopting isolated particle .approach and underestimated values by using Abeles model.

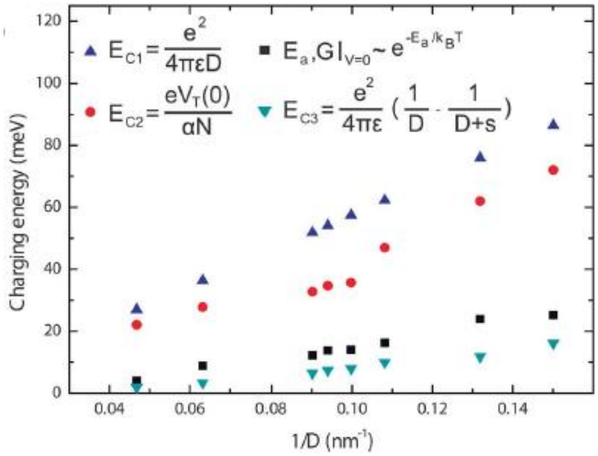

Figure 1.1.9: Charging energy obtained by different approaches showing the overestimated value by isolated model approach and underestimated values by using equation 1.1 (r). [Referene [34]]

1.1.4.(b) Effect of inter-particle spacing

One approach which is often used to vary the inter-particle spacing in Nps assemblies is using alkyl ligands of different chain lengths. Ligands with functional groups at both of their terminal (cross-linkers), usually connect to particles at both ends and effectively separate the particles by a distance proportional to their length. On the other hand, a mono-functional ligand attaches to a single Np thus separating the Nps by twice of its effective length. Tan *et al.* [37] have used this approach to study the effect of inter-particle spacing on electron transport and charging energy in assemblies of Co Nps of fixed metallic core diameter (10.3 nm). Among the three different alkyl chains used in the study, nanoparticle assemblies with alkyl chain having 18 carbons (C18) was found to be least conducting followed by the one with 12 carbon (C12) and four carbon (C4). As shown in Figure 1.10 (a), threshold voltage at low temperatures also follows the order V_t (C18) > V_t(C12)> V_t (C4). Charging energy in these assemblies was found to be dependent on inter-particle separations such that increase in interparticle separation led to an increase in Coulomb blockade. Duan *et al*. [34] have also studied the effect of inter-particle separation on charging energy in assemblies of gold nanoparticles. The variation in charging energy as a function of inter-particle separation as shown in Figure 1.1.10(b)

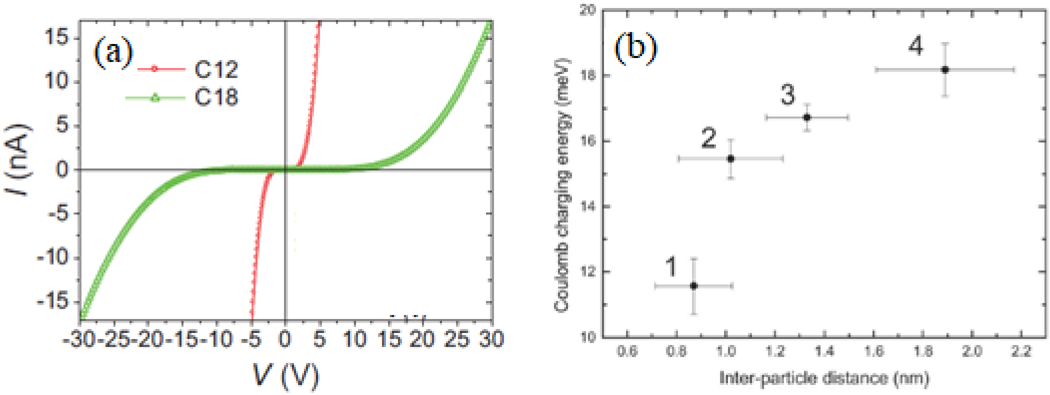

Figure 1.1.10**:** (a) *I-V* curves for Co Np arrays with different alkyl ligands at 2 K showing higher Coulomb gap for higher inter-particle spacing. Reference [37]. (b) Charging energy as a function of inter-particle separation for gold Nps assemblies showing a positive trend with interparticle distance Reference [34].

References: Chapter 1.1 Coulomb blockade

[1] A. van Itterbeek and L. de Greve, "Measurements on the electrical resistivity of thin nickel films," *Experientia,* journal article vol. 3, no. 7, pp. 278-279, July 01 1947.

[2] R. Lambeir, A. Van Itterbeek, and G. J. Van Den Berg, "Measurements on the electrical resistivity of thin iron films at. Liquid helium temperatures," *Physica,* vol. 16, no. 11, pp. 907-914, 1950/12/01/ 1950.

[3] C. J. Gorter, "A possible explanation of the increase of the electrical resistance of thin metal films at low temperatures and small field strengths," *Physica,* vol. 17, no. 8, pp. 777-780, 1951/08/01/ 1951.

[4] C. A. Neugebauer and M. B. Webb, "Electrical Conduction Mechanism in Ultrathin, Evaporated Metal Films," *Journal of Applied Physics,* vol. 33, no. 1, pp. 74-82, 1962.

[5] T. A. Fulton and G. J. Dolan, "Observation of single-electron charging effects in small tunnel junctions," *Physical Review Letters,* vol. 59, no. 1, pp. 109-112, 07/06/ 1987.

[6] K. Yano, T. Ishii, T. Hashimoto, T. Kobayashi, F. Murai, and K. Seki, "Room-temperature single-electron memory," *IEEE Transactions on Electron Devices,* vol. 41, no. 9, pp. 1628-1638, 1994.

[7] V. Krstić, S. Roth, M. Burghard, and K. Kern, "Carbon Nanotubes in the Coulomb-Blockade regime connected to superconducting leads," *AIP Conference Proceedings,* vol. 591, no. 1, pp. 405-408, 2001.

[8] C. Stampfer, J. Güttinger, F. Molitor, D. Graf, T. Ihn, and K. Ensslin, "Tunable Coulomb blockade in nanostructured graphene," *Applied Physics Letters,* vol. 92, no. 1, p. 012102, 2008.

[9] S. Huang, N. Fukata, M. Shimizu, T. Yamaguchi, T. Sekiguchi, and K. Ishibashi, "Classical Coulomb blockade of a silicon nanowire dot," *Applied Physics Letters,* vol. 92, no. 21, p. 213110, 2008/05/26 2008.

[10] A. Zabet-Khosousi and A.-A. Dhirani, "Charge Transport in Nanoparticle Assemblies," *Chemical Reviews,* vol. 108, no. 10, pp. 4072-4124, 2008/10/08 2008.

[11] J. Kane, J. Ong, and R. F. Saraf, "Chemistry, physics, and engineering of electrically percolating arrays of nanoparticles: a mini review," *Journal of Materials Chemistry,* 10.1039/C1JM12005K vol. 21, no. 42, pp. 16846-16858, 2011.

[12] H. van Kempen, J. G. A. Dubois, J. W. Gerritsen, and G. Schmid, "Small metallic particles studied by scanning tunneling microscopy," *Physica B: Condensed Matter,* vol. 204, no. 1, pp. 51-56, 1995/01/01/ 1995.

[13] D. L. Klein, R. Roth, A. K. L. Lim, A. P. Alivisatos, and P. L. McEuen, "A single-electron transistor made from a cadmium selenide nanocrystal," *Nature,* vol. 389, p. 699, 10/16/online 1997.

[14] S. H. M. Persson, L. Olofsson, and L. Gunnarsson, "A self-assembled single-electron tunneling transistor," *Applied Physics Letters,* vol. 74, no. 17, pp. 2546-2548, 1999.

[15] H. Park, A. K. L. Lim, A. P. Alivisatos, J. Park, and P. L. McEuen, "Fabrication of metallic electrodes with nanometer separation by electromigration," *Applied Physics Letters,* vol. 75, no. 2, pp. 301-303, 1999.

[16] B. Wang, H. Wang, H. Li, C. Zeng, J. G. Hou, and X. Xiao, "Tunable single-electron tunneling behavior of ligand-stabilized gold particles on self-assembled monolayers," *Physical Review B,* vol. 63, no. 3, p. 035403, 12/22/ 2000.

[17] D. V. Averin and Y. V. Nazarov, "Virtual electron diffusion during quantum tunneling of the electric charge," (in eng), *Phys Rev Lett,* vol. 65, no. 19, pp. 2446-2449, Nov 5 1990.

[18] M. Amman, R. Wilkins, E. Ben-Jacob, P. D. Maker, and R. C. Jaklevic, "Analytic solution for the current-voltage characteristic of two mesoscopic tunnel junctions coupled in series," (in eng), *Phys Rev B Condens Matter,* vol. 43, no. 1, pp. 1146-1149, Jan 1 1991.

[19] A. E. Hanna and M. Tinkham, "Variation of the Coulomb staircase in a two-junction system by fractional electron charge," *Physical Review B,* vol. 44, no. 11, pp. 5919-5922, 09/15/ 1991.

[20] R. L. Kautz, G. Zimmerli, and J. M. Martinis, "Self-heating in the Coulomb-blockade electrometer," *Journal of Applied Physics,* vol. 73, no. 5, pp. 2386-2396, 1993/03/01 1993.

[21] K. K. Likharev, "Single-electron devices and their applications," *Proceedings of the IEEE,* vol. 87, no. 4, pp. 606-632, 1999.

[22] C. A. Berven, L. Clarke, J. L. Mooster, M. N. Wybourne, and J. E. Hutchison, "Defect-Tolerant Single-Electron Charging at Room Temperature in Metal Nanoparticle Decorated Biopolymers," *Advanced Materials,* vol. 13, no. 2, pp. 109-113, 2001.

[23] C. A. Berven, M. N. Wybourne, L. Clarke, L. Longstreth, J. E. Hutchison, and J. L. Mooster, "Background charge fluctuations and the transport properties of biopolymer-gold nanoparticle complexes," *Journal of Applied Physics,* vol. 92, no. 8, pp. 4513-4517, 2002/10/15 2002.

[24] R. Parthasarathy, X. M. Lin, K. Elteto, T. F. Rosenbaum, and H. M. Jaeger, "Percolating through networks of random thresholds: finite temperature electron tunneling in metal nanocrystal arrays," (in eng), *Phys Rev Lett,* vol. 92, no. 7, p. 076801, Feb 20 2004.

[25] A. A. Middleton and N. S. Wingreen, "Collective transport in arrays of small metallic dots," *Physical Review Letters,* vol. 71, no. 19, pp. 3198-3201, 11/08/ 1993.

[26] M. O. Blunt *et al.*, "Charge transport in cellular nanoparticle networks: meandering through nanoscale mazes," (in eng), *Nano Lett,* vol. 7, no. 4, pp. 855-60, Apr 2007.

[27] M. G. Ancona, W. Kruppa, R. W. Rendell, A. W. Snow, D. Park, and J. B. Boos, "Coulomb blockade in single-layer Au nanocluster films," *Physical Review B,* vol. 64, no. 3, p. 033408, 06/22/ 2001.

[28] J. Kane, M. Inan, and R. F. Saraf, "Self-Assembled Nanoparticle Necklaces Network Showing Single-Electron Switching at Room Temperature and Biogating Current by Living Microorganisms," *ACS Nano,* vol. 4, no. 1, pp. 317-323, 2010/01/26 2010.

[29] C. Reichhardt and C. J. Olson Reichhardt, "Temperature and ac effects on charge transport in arrays of metallic dots," *Physical Review B,* vol. 68, no. 16, p. 165305, 10/08/ 2003.

[30] R. W. Rendell *et al.*, "Electron transport in nanocluster films with random voids," *IEEE Transactions on Nanotechnology,* vol. 2, no. 2, pp. 75-81, 2003.

[31] C. Reichhardt and C. J. Olson Reichhardt, "Charge Transport Transitions and Scaling in Disordered Arrays of Metallic Dots," *Physical Review Letters,* vol. 90, no. 4, p. 046802, 01/28/ 2003.

[32] R. Parthasarathy, X.-M. Lin, and H. M. Jaeger, "Electronic Transport in Metal Nanocrystal Arrays: The Effect of Structural Disorder on Scaling Behavior," *Physical Review Letters,* vol. 87, no. 18, p. 186807, 10/16/ 2001.

[33] H. E. Romero and M. Drndic, "Coulomb Blockade and Hopping Conduction in PbSe Quantum Dots," *Physical Review Letters,* vol. 95, no. 15, p. 156801, 10/03/ 2005.

[34] C. Duan *et al.*, "Controllability of the Coulomb charging energy in close-packed nanoparticle arrays," *Nanoscale,* 10.1039/C3NR02334F vol. 5, no. 21, pp. 10258-10266, 2013.

[35] T. B. Tran, I. S. Beloborodov, J. Hu, X. M. Lin, T. F. Rosenbaum, and H. M. Jaeger, "Sequential tunneling and inelastic cotunneling in nanoparticle arrays," *Physical Review B,* vol. 78, no. 7, p. 075437, 08/26/ 2008.

[36] B. Abeles, P. Sheng, M. D. Coutts, and Y. Arie, "Structural and electrical properties of granular metal films," *Advances in Physics,* vol. 24, no. 3, pp. 407-461, 1975/05/01 1975.

[37] J. Dugay *et al.*, "Charge transport and interdot coupling tuned by the tunnel barrier length in assemblies of nanoparticles surrounded by organic ligands," *Physical Review B,* vol. 89, no. 4, p. 041406, 01/23/ 2014.

1.2 Tunnel magnetoresistance

In the first part of this chapter, we focussed our attention on the charge transport properties of nanoparticle arrays which involved electron tunneling through metal/insulator/metal junctions. However, throughout section 1, we did not consider the effects of spin on electron transport as we discussed only the non-magnetic tunnel junctions. In case of magnetic tunnel junctions (MTJs), role of spin becomes significantly important and gives rise to novel phenomenon of magnetoresistance. In MTJs, where two ferromagnetic (FM) layers are separated by an optimally thin insulating barrier, the tunneling resistance depends on the relative orientation of the magnetization in the two FM layers. A low tunneling resistance is observed when the direction of magnetization in both layers are parallel to each other, whereas reverse is true for the antiparallel alignment. Application of an external magnetic field can change the direction of the magnetization and consequently, the tunneling resistance. This change in resistance with magnetization orientation of the two magnetic layers is called tunnel magneto-resistance (TMR) effect. Figure 1.2.1 shows a schematic representation of MTJs and variation in its resistance with magnetic field. In order to quantify the TMR effect, the TMR ratio can be calculated by using one of the two following equations:

$$\mathrm{TMR} = \frac{R_{AP} - R_P}{R_P} \qquad 1.2\,(a)$$

$$\mathrm{TMR} = \frac{R_{AP} - R_P}{R_{AP}} \qquad 1.2\,(b)$$

where R_{AP} and R_{P} are the junction resistances when the magnetization of the two magnetic layers are anti-parallel and parallel repectively. In the first case, the maximum TMR tends toward infinity whereas, in the second case, it is tend toward 1.

In 1975, Julliere first reported the phenomenon of TMR in Fe/Ge/Co MTJs at low temperature [1]. However, it gained only little attention due to technologically demanding fabrication process of MTJs, and low TMR ratio observed at room temperature. In 1995, Miyazaki and Tezuka [2], and Moodera *et al*. [3] reported the large values of TMR ratio at room temperature using Al_2O_3 barrier. Since then, a large number of studies have been dedicated to TMR effect in tunnel junctions with inorganic and organic barriers.

TMR effect has been also studied in granular magnetic films where magnetic particles are embedded in an insulating matrix [4-8]. These films are often considered as an assembly of nano-sized sandwich-type tunnel junctions connected in a network [7]. Besides, in granular magnetic films, an interplay between Coulomb blockade and spin dependent tunneling gives rise to interesting charge transport and magneto-resistive properties. At low temperatures, enhanced TMR ratios attributed to co-tunneling mechanism have been observed in several studies [9-11].

Today, TMR holds great importance in the field of spintronics and remains the underlying principle of various modern functional devices such as sensors and memory devices [12, 13]. In order to study the influence between Coulomb blockade properties and TMR, assemblies of chemically prepared magnetic nanoparticles (MNps) coated with organic barriers have gained significant attention [14-19] as they offer better control over the shape and size of the particles compared to MNps prepared by physical methods. The core shell structure of these particles allows the formation of a tunnel junction between the two particles much in a similar way as in granular films prepared by physical methods. Assemblies of these particles have promising magnetoresistive properties which could makes them suitable candidate for various applications, in particular the elaboration of cheap on-chip sensors, which would be elaborated by drop casting of colloidal solutions.

The objective of this chapter is to build up our understanding of magnetotransport properties which would help us to explain the results obtained on assemblies of chemically synthesized FeCo MNps during the course of this thesis. Since the physics of TMR is very vast, it is beyond the scope of this chapter to capture all its aspects. Thus, we shall restrict ourself to the selective aspects of TMR. Here, we shall present the basic concepts of TMR and discuss the role of various parameters such as temperature, voltage, and magnetic field. We shall also discuss the higher order co-tunneling mechanism and its effects on TMR. Originally, these studies have been obtained either for conventional MTJs or for granular films prepared by physical methods, nevertheless they are frequently used to explain the magnetotransport properties in assemblies of chemically synthesized MNps.

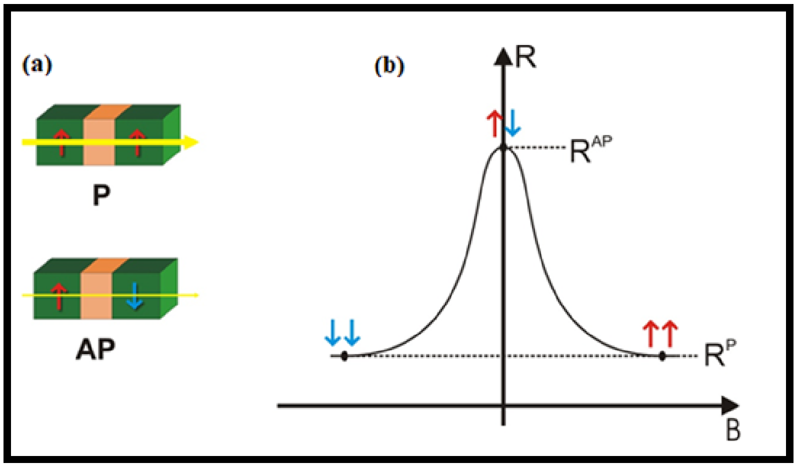

Figure 1.2.1: (a) Sketch of magnetic tunnel junctions showing magnetic layers (in green) having parallel (P) and anti-parallel (AP) direction of magnetization. The thickness of horizontal arrow corresponds to the magnitude of tunneling current. (b) Sketch of a TMR curve showing variation in resistance as a function of field. [Reference [20]].

1.2.1 TMR in MTJs: Julliere's Model

In the first TMR experiment, Julliere oberved a TMR ratio of about 14% in Fe/Ge/Co MTJ at 4.2 K [1]. At that time, the concept of spin dependent tunneling was already established which suggested that probability of an electron to tunnel through a barrier depends on its spin [21]. Julliere proposed a phenomenological model of TMR effect based on spin dependent tunneling. The two main assumptions of this model are as follows:

i) **Spin conservation during tunneling**
This assumption implies that tunneling of up spins and down spins occur via two separate channels. Further, if the two FM layers have parallel magnetizations, then minority spins tunnel to the minority states while majority spins tunnel to majority states. In case of anti-parallel magnetization, reverse in true. This is depicted by using a schematic diagram in Figure 1.2.2.

ii) **Conductance and density of states relation**
Julliere proposed that the product between the effective density of states of the two ferromagnetic layer should determine the conductance of a particular spin orientation. Thus, conductance for the parallel configuration (G_p) and antiparallel configuration (G_AP) can be formulated as

$$G_p \propto \rho_1^{\uparrow}\rho_2^{\uparrow} + \rho_1^{\downarrow}\rho_2^{\downarrow} \qquad 1.2\,(c)$$

$$G_{Ap} \propto \rho_1^{\uparrow}\rho_2^{\downarrow} + \rho_1^{\downarrow}\rho_2^{\uparrow} \qquad 1.2\,(d)$$

where $\rho_i^{\uparrow}$ is the density of states of up spin and $\rho_i^{\downarrow}$ be the density of states of down spin in i$^{\mathrm{th}}$ ferromagnetic layer (i =1,2).

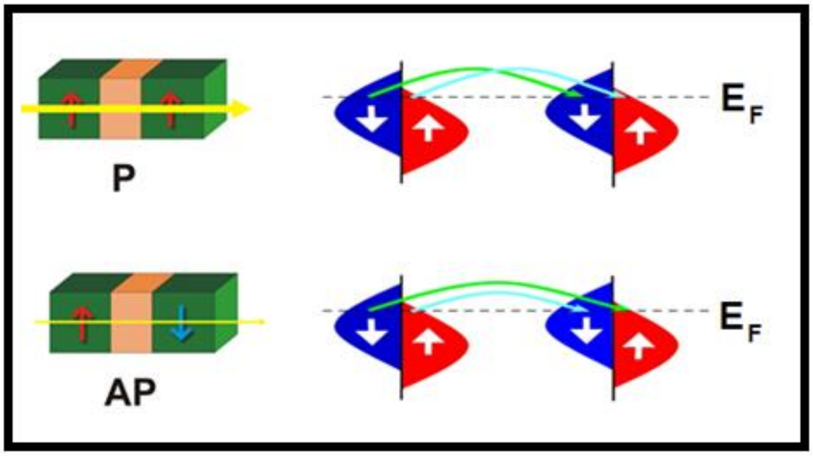

Figure 1.2.2: Schematic representation of density of states of two FM layers showing spin dependent tunneling when the magnetization of the two layers are parallel (above) and anti-parallel (below) to each other.Reference [20].

Julliere expressed TMR in terms of spin polarizations P_1 and P_2 of the two FM layers which is given by equation 1.2 (e).

$$TMR = \frac{2P_1P_2}{1 - P_1P_2} \qquad 1.2\ (e)$$

where, $P_i = \frac{\rho_i^{\uparrow} - \rho_i^{\downarrow}}{\rho_i^{\uparrow} + \rho_i^{\downarrow}} \qquad (i = 1,2) \qquad 1.2(f)$

From equation 1.2 (e),it is evident that spin polarization governs the TMR in the MTJs. Values of spin polarization can be obtained experimentally from tunneling measurements using superconducting electrodes. Experimentally observed polarization values for Fe, Co and Ni are 0.44, 0.34 and 0.11 respectively [21]. The TMR ratios predicted by equation 1.2 $(e)$for these values are 0.48 for Fe, 0.26 for Co, and 0.1 for Ni. These values are in good agreement with experimentally observed TMR values for these materials with Al_2O_3 barrier [22, 23].

Although Julliere's model provide a good explanation of TMR effect, it is rather a simplified model. It does not take into account the structure of the junction and consider the spin polarization to be the intrinsic property of the FMs. Consequently, it fails to describe the higher TMR ratios observed in MTJs with MgO barrier. Moreover, Slonczewski provided an improved model of TMR where he could show that TMR amplitude may vary depending on the barrier height and thickness [24].

1.2.2 TMR in granular magnetic films

In case of granular magnetic films composed of particles embedded in an insulating matrix, tunneling resistance depends on the magnetization direction of the individual grains involved in the tunneling. In comparison to conventional MTJs, there exists two main differences in granular films which are as follows:

i) In typical samples, the easy axis of the MNps are randomly oriented in space. If magnetic interactions between MNps is negligible, this is thus also true for the orientation of their magnetization in the absence of external magnetic field.

ii) Due to their granular nature, charging energy needs to be taken into account. Therefore, an additional term of e^{-E_c/k_bT} should be incorporated in the expression of conductance.

Taking above two points into the account, Maekawa *et al*. [4] derived an expression for conductance and TMR ratio for granular magnetic films which are given by equation 1.2 (g) and 1.2 (h) respectively.

$$G = G_o(1 + P^2m^2)e^{-2\sqrt{\frac{2\kappa C}{k_bT}}} \qquad 1.2\ (g)$$

and,

$$TMR = \frac{m^2P^2}{1 + m^2P^2} \qquad 1.2\ (h)$$

where C is the product of barrier length (s) and charging energy (E_c), and assumed to be constant, m is the relative magnetization given by the ratio of magnetic moment to the saturated moment (i.e. M/M_s).

For small values of P, TMR should vary as ~ m^2P^2 which becomes P^2 for $m = 1$. Experimental results from Mitani *et al*. [7] showed m^2 dependence of TMR in granular Co Al-O film [as shown in Figure 1.2.3 (a) and (b)] ,which is in good agreement with the equation 1.2 (h).

1.2.3 Effect of magnetic field

(a) Low field TMR

At low field values, TMR curve of granular films can be related to the magnetization reversal of the grains. Mitani *et al*. [7] reported the magnetization reversal and TMR curves for Co-Al-O granular films at low-temperature and room-temperature as shown in Figure 1.2.3 (a) and (b) respectively. At low temperature, magnetic moment and resistance both showed a hysteresis with respect to the applied field. The hysteresis in the resistance could be understood in terms of the alignment of magnetic moment of the grains. At saturation field, magnetic moments of the grains are aligned in the direction of the field up to the maximum extent. In this state, the tunneling resistance is minimum which can be seen in the TMR curve. Decreasing the field causes randomization of the moments and consequently an increase in the resistance. When the field passes through zero and reaches the coercive field of the film, the magnetic moment of the grains attain a maximum randomization. As a result, peak in the resistance is observed at the coercive field, as shown in Figure 1.2.3 (a).

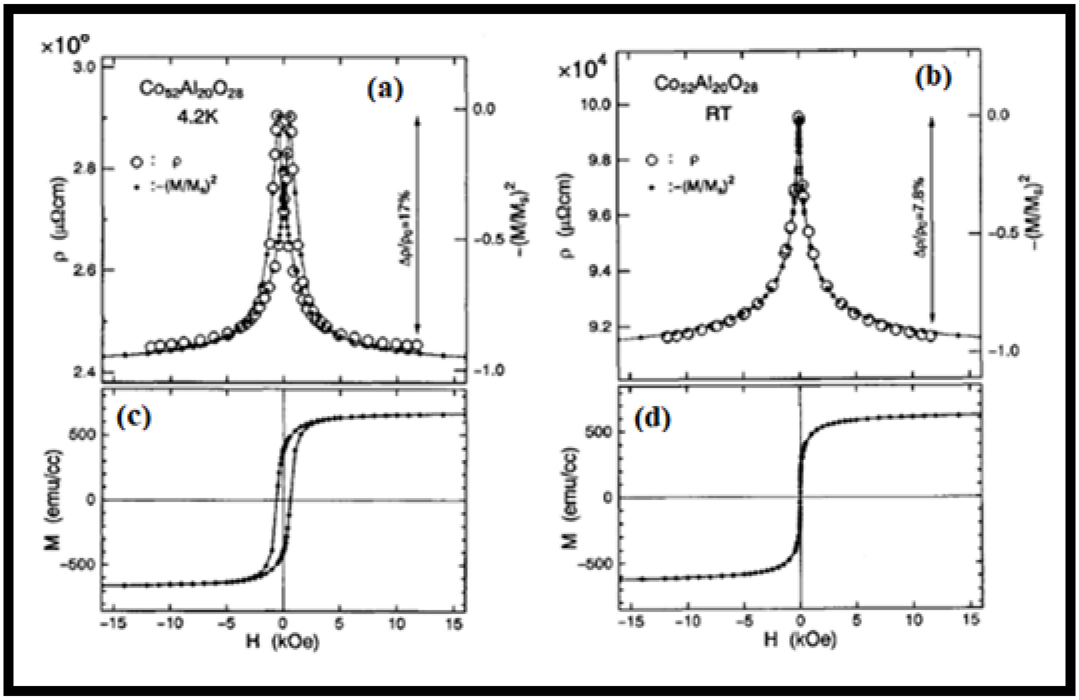

Figure 1.2.3: TMR curves for Co-Al-O granular film showing the change in resistance as a function of external applied field at (a) low-temperature (4.2 K), and (b) room-temperature. Magnetization reversal of the films at (c) low temperature, and (d) room temperature. The TMR curves can be related to magnetization reversal in both cases. [Reference [7]].

At room temperature, no hysteresis appears in the magnetization reversal curve, a signature that the MNps are superparamagnetic.In this case, the direction of the moments are in maximum random state at zero field. Consequently, no hysteresis appears in the TMR curve as well, and a maximum resistance occurs at zero field as shown in Figure 1.2.3 (b).

(b) High field TMR

We have seen in the previous section that TMR curves can be related to the magnetization reversal such that a maximum value of resistance occurs at the coercive field and a minimum value at the saturation field. It is intuitive to conclude that beyond saturation field, no further change in the resistance should take place. However, several studies have reported high field magneto-resistance in granular [25, 26] , polycrystalline [27, 28] and nanoparticle [15, 29, 30] films.

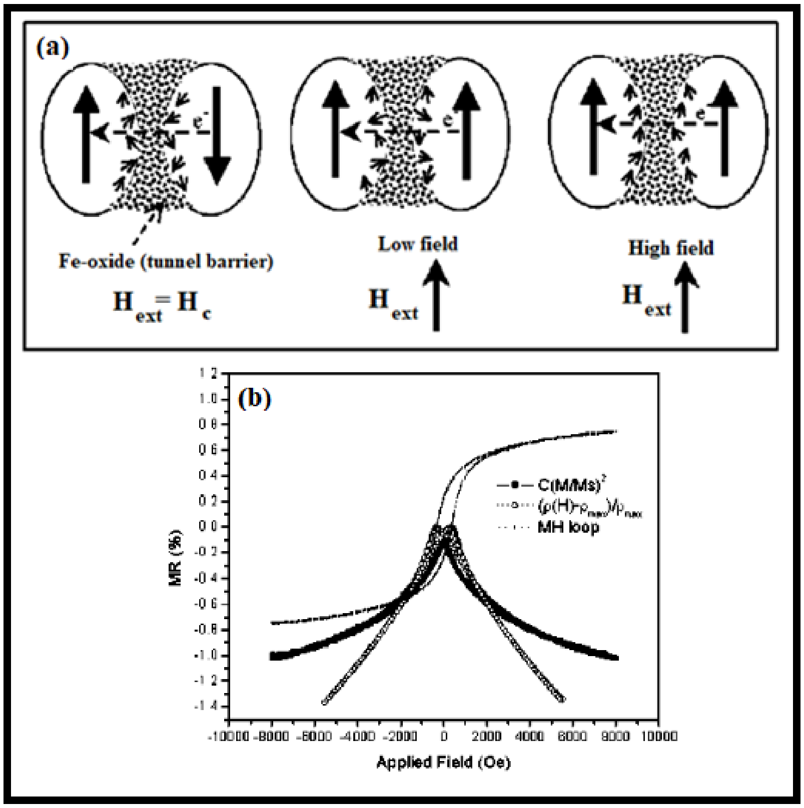

Figure 1.2.4: (a) Schematic representation of the grains and grain boundary of Fe_3O_4 granular film showing spins in the core and at the grain boundary. While the spins in the core saturates at low field, the spins at the boundary needs higher field for alignment. (b) TMR curve of the same film (dotted –dot line) showing peaks in the resistance at coercive field as shown in M-H loop (dotted line) . TMR curve follows $(M/M_s)^2$ (dotted-dash line) behavior at low field. At high field values, TMR curve deviates from $(M/M_s)^2$ behavior. [Reference [27]].

Park *et al*. [27] have reported high field TMR in polycrystalline Fe_3O_4 grains with amorphous grain boundaries. The spins at these boundaries have different local enviroment and saturate at higher field values compared to the spins in the core as shown in Figure 1.2.4 (a). Park *et al.* suggested that significant contribution in tunneling comes from these spins. As shown in Figure 1.2.4 (b) , room temperature TMR curve exhibits a maximum resistance at coercive field and follows $-(M/M_s)^2$ at low field values. However, at higher field values, deviation from $-(M/M_s)^2$ behavior is observed where the resistance does not reach saturation. This is attributed to the different saturation field for the spin at the boundaries and in the core. At low field values, spins in the core allign in the direction of field giving rise to low field magneto-resistance while the spins at the bondaries remain randomly oriented. On further increasing the field, spins at the boundries starts to align as well, giving rise to high field magnetoresistance.

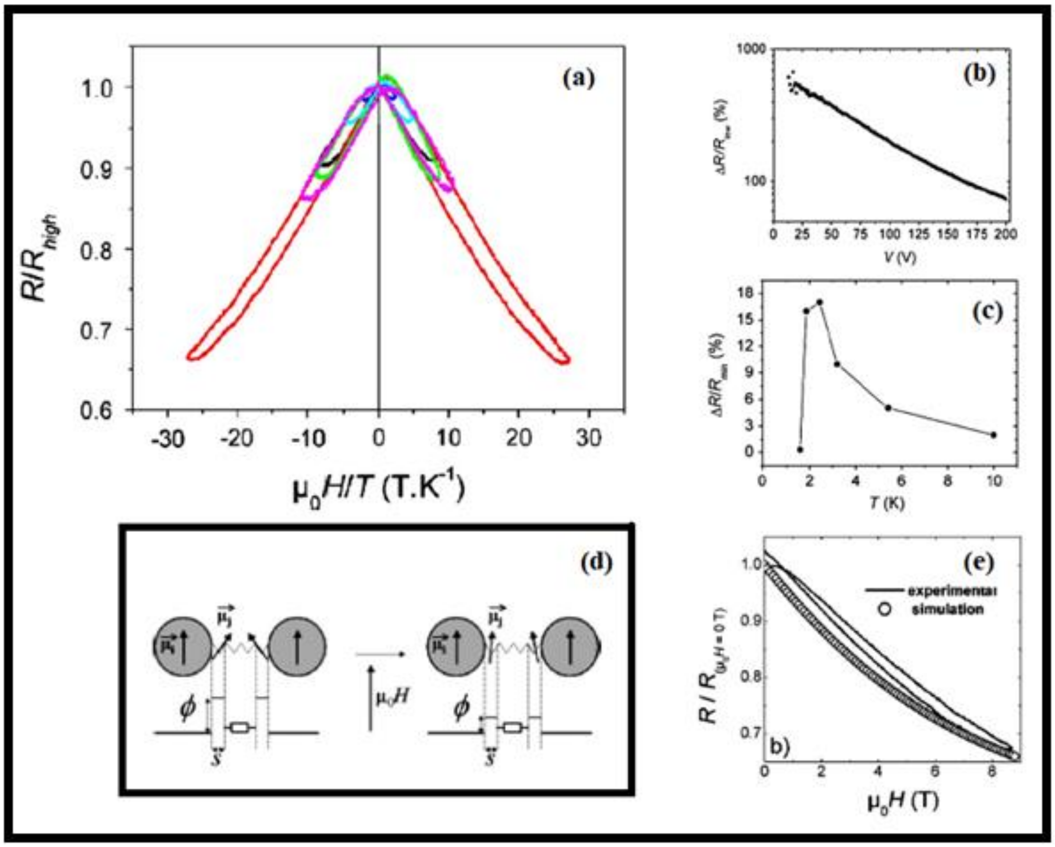

Figure 1.2.5 : (a) High field magnetoresistance in FeCo super lattice showing a scaling behavior with field/ temperature ratio for different temperatures (ranging between 3.1 and 10 K) and maximum magnetic field values (ranging between 1.5 and 8.6 T). (b) High field magnetoresistance as a function of voltage, and (c) High field MR showing a rapid decrease with temperature (d) schematic representation of effective tunnel barrier showing the high tunnel barrier when impurity spins are randomly aligned at low field (left) and low efective tunnel barrier when impurity spins are aligned at high field (e) experimental and simulation (based on the proposed model) data for high field magnetoresistance showing good agreement at T= 3.15 K, and V= 200 V. [Figure (a), (b) and (c) are taken from reference [31] ,and figure (d) and (e) are from reference [30]].

In our laboratory, Tan *et al*. observed the presence of a high field magneto-resistance in FeCo superlattices and nanoparticle assemblies in low temperature range (~ 2K-10K) [30-32]. The amplitude of the high field TMR scaled with magnetic field/temperature ratio [Figure 1.2.5 (a)] and decreased with an increase in voltage or temperature conditions as shown in Figure 1.2.5 (b) and (c) respectively. Tan *et al*. attributed this to the presence of paramagnetic impurites that could be present on the surface of the particles or within the barrier. It was proposed that individual magnetic moments of the impurities create an effective tunnel barrier which is removed progressively as the field is increased [Figure 1.2.5 (e)]. Starting with this hypothesis, Tan *et al*. [30] proposed a model for high field magnetresistance which described well the observed experimental results [Figure 1.2.5 (d)].

1.2.4 Effect of temperature

TMR amplitude can be significantly influenced by temperature. Several studies have reported temperature dependent TMR in conventional MTJs as well as in granular magnetic films [15, 17, 33-38]. In most cases, TMR amplitude decreases with increase in temperature. Such a temperature dependence is attributed to various physical phenomena. Here, we shall discuss the temperature dependence arising due to spin polarization and spin flipping process.

(a) Spin polarization

Shang *et al*. [33] proposed that the temperature dependency of TMR amplitude could arise due to the variation in spin polarization (P) with temperature. It was already known that, in the case of alloys, spin polarization scales approximately with the magnetic moment of the alloy as its concentration is varied [39]. As an extention of this proportionality, Shang et *al*. argued that spin polarization should follow the same temperature dependence as the one of the magnetic moment. Thus the polarization as a function of temperaure can be given as

$$P(T) = P_o\left(1 - \alpha T^{3/2}\right) \qquad 1.2(i)$$

where α is a material dependent constant.

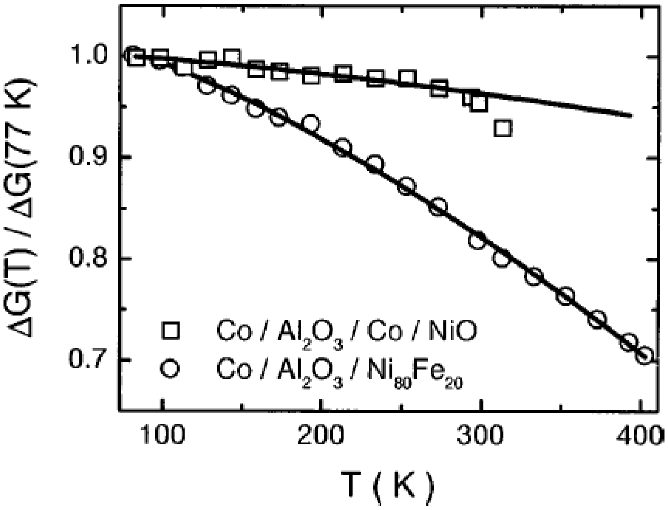

Figure 1.2.6: Temperature dependence of TMR in different magnetic tunnel junctions. Solid line represents the fit obtained by the model of Shang *et al*. [Reference [33]].

Using this model, they could successfully describe the temperature variation of TMR in $Co/Al_2O_3/Co/NiO$ and $Co/Al_2O_3/Ni_{80}Fe_{20}$ MTJs observed in their experimental studies as shown in Figure 1.2.6.

(b) Spin flipping:

We recall that in Julliere's model, spin of the tunneling eletron is assumed to be conserved during the tunneling process. However, this might not always be the case. When there exist an impurity in the barrier, tunneling electron may interact with the impurity and reverse its spin. Such a spin-flip process may suppress the TMR ratio. Vedyayev *et al*. [34] investigated the TMR in MTJs with ferromagnets and an oxide barrier containing paramagnetic impurities. They assumed that the spin of the paramagnetic impurity is magnetically coupled to the spin of the magnetization in both the ferromagnets as well as with the spin of the tunneling electron. It was observed that a temperature increase causes a decrease in TMR amplitude due to the excitation of spin flip processes resulting in mixing of spin up and spin down channels. In the presence of spin-flip scattering, TMR is reported to vary as $exp\,(-k_bT/E_{mr})$, where E_{mr} is the energy associated with spin flip scattering, though its exact cause remains unclear.

Zhu *et al*. [40] have measured a temperature dependent TMR in Fe-Al_2O_3 granular films. At low temperature, TMR dependence could be described by using co-tunneling model, however at high temperatures it failed to describe the decrease in TMR. By incorporating the spin flip scattering term into a co-tunneling model, Zhu *et al.* could describe the temperature dependence of TMR in high and low temperature regimes as shown in Figure 1.2.7.

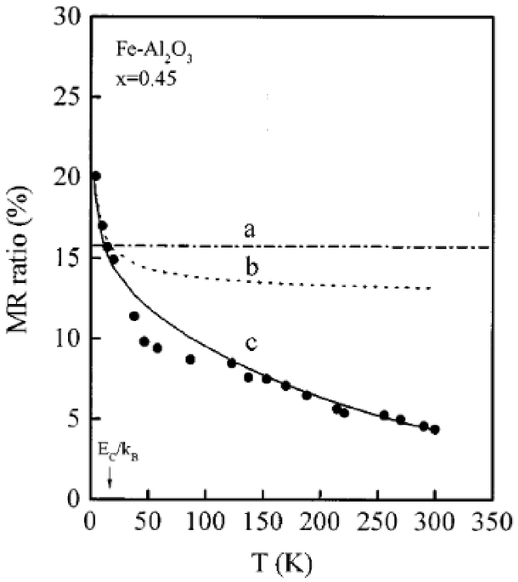

Figure 1.2.7: Temperature variation of magnetoresistance in Fe-Al$_2$O$_3$ granular film showing experimentally observed data (black dots), TMR value predicted from $P^2/\ 1{+}P^2$, with P = 0.44 for iron (dot-dashed line), TMR predicted by cotunneling model (dotted line), and TMR predicted by combining spin flip scattering term with cotunneling model (solid line). [Reference [40]].

1.2.6 Effect of voltage

A general trend observed in most studies is a decrease of TMR amplitude with an increase of the applied voltage. To explain the decrease in TMR with increase in voltage, Zhang *et al*. [41] proposed a model in which the reduction in TMR at high voltages was attributed to the magnons. It was assumed that at a non zero voltage, when an electron from one FM layer crosses the barrier and reaches the other FM layer, it has energy higher than Fermi energy. These electrons, termed as hot electron, lose the energy by emitting a magnon which results in flipping of the spin. An increase in voltage causes more magnons to be emitted, thus reducing the TMR. Experimental studies in agreement with this model have been reported by Moodera *et al.* [42].

Zhang and White [43] proposed a model in which the voltage dependency of TMR was attributed to trap states present in the insulating barrier. This model was backed up by experimental studies performed by Wulfhekel *et al*. [44], in which TMR was investigated between the tip of a scaning tunneling microscope and a Co layer. Such an experiment allows one to avoid the imperfections of a barrier as vacuum itself act as a barrier in this case. It was found that in the presence of vacuum as a barrier, the dependency of TMR on voltage was quite low, indicating that impurities in barriers are responsible for the voltage dependency.

1.2.7 Co-tunneling and its effect on TMR

We have seen previously that at low temperature, charging energy becomes dominant over thermal energy and Coulomb gap starts to appear in the *I-V* curves. In the Coulomb gap, the sequential tunneling between the neighboring particles could be blocked due to the high charging energy required. However, a small current could still flow via the mechanism of co-tunneling.

In arrays of particles, there exists a distribution of particles size, and it is highly probable that larger particles are well separated from each other due to their low number density while the smaller particles occupy the space between them. It has been proposed that such a condition can give rise to a tunneling mechanism known as co-tunneling, whereby Coulomb blockade can be surpassed due to cooperative electron transfer through several neighbor particles [45, 46]. At low temperature, tunneling of an electron from larger particle to a smaller particle is inhibited as it requires higher energy. However, electron can tunnel from one larger particle to another with the help of successive tunneling between the smaller particles as shown in Figure 1.2.8(a). It is worth mentioning that the charge transfer from the initial particle to the final one takes place through virtual states and is thus counted as a single quantum event.

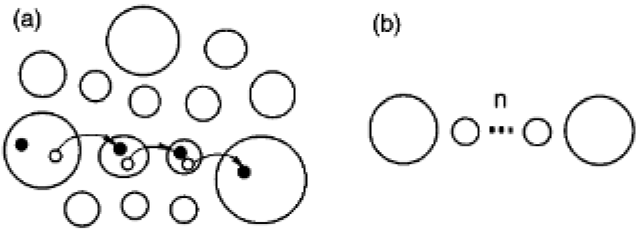

Figure 1.2.8: (a) Sketch of particles in an assembly showing the distribution of size, and the cotunneling process where electron transfer takes place via successive tunneling between neighboring particles (b) Model adopted by Mitani *et al*. showing two identical large particles separated by smaller identical particles.[Reference [46].

In the cotunneling regime, it is very difficult to obtain an exact analytical expression between the current and voltage. Middleton-Wingreen equation can no longer be applied since it is based on the assumption that tunneling occurs only between the neighboring particles. Tran *et al*. [47] [48] have proposed an approximate formula relating the *I-V* curves in the inelastic cotunneling regime which is given as

$$I \sim V_j \left[\frac{g}{g_j}\right]^j e^{\frac{jeV_j - E}{k_b T}} \left[\frac{\left(eV_j\right)^2 + \left(k_b T\right)^2}{E_c^2}\right]^{j-1} \qquad 1.2\,(j)$$

where V_j is the voltage drop across each junction, E_c is the charging energy, g_j is the junction's tunnel conductane, and j being the number of juctions involved in the cotunneling.

It has been shown that co-tunneling mechanism can significantly enhance the TMR amplitude at low temperatures [10]. Mitani *et al.* [46] used co-tunneling phenomenon to explain the anomalously high values of TMR at low temperatures in granular Co–Al-O films as shown in Figure 1.2.9. They proposed a model for TMR based on the assumption of a perfectly bimodal distribution of particle sizes, in which the large particles are monodisperse as well as the smaller ones, as shown in [Figure 1.2.8(b)] . Using this assumption, they derived a relation between TMR and temperature which is given by equation 1.2 (j) .

$$\Delta\rho/\rho_o \approx P^2 m^2 \left(1+\sqrt{\frac{C}{T}}\right) \qquad 1.2\ (j)$$

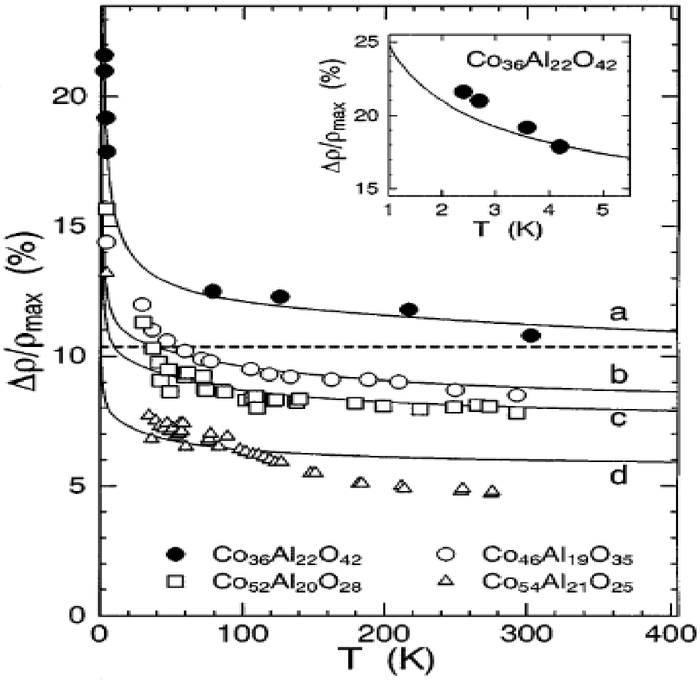

Figure 1.2.9 Anomalous increase in the TMR at low temperature in Co-Al-O films with different metal concentration. Sharp increase in TMR at low temperatures is attributed to cotunneling. Solid line is the fit given using the model proposed by Mitani *et al.* [Reference [46]].

1.2.8 TMR in assemblies of chemically synthesized nanoparticles

Black *et al*. [14] first reported TMR in self-assembled Co particles coated with oleic acid. At low temperature, they observed TMR amplitude ranging from 5-12% in different devices which dropped down rapidly with temperature. The TMR curve could be clearly related to the magnetization reversal in the assembly, showing peaks in the resistance at the coercive field [see Figure 1.2.10 (b)].

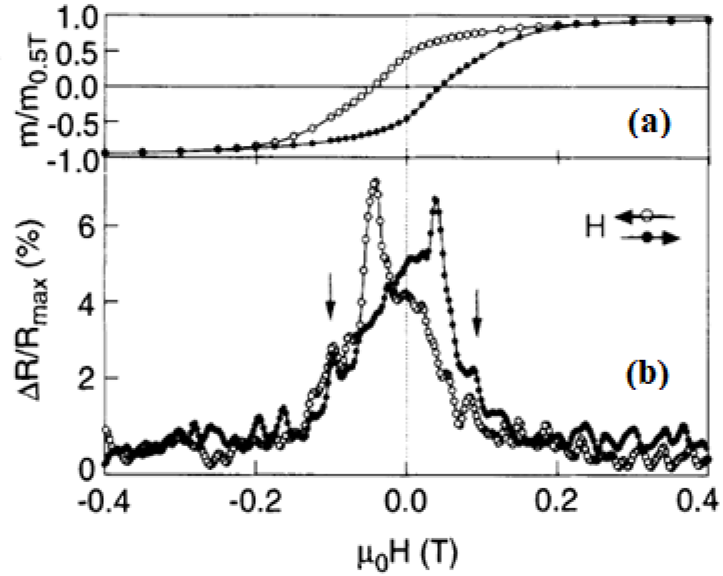

Figure 1.2.10: (a) Magnetic hysteresis loop observed for chemically prepared Co nanoparticles at low-temperature and (b) TMR curve obtained for the self-assembly of the same particles showing hysteresis in resistance at low temperature. [Reference [14]]

In our laboratory, Dugay *et al*. [15] reported the TMR in arrays of cubic Fe nanoparticles coated with hexadecyl amine /Hexadecyl ammonium and spherical Fe particles coated with hexadecyl amine/palmitic acid. These particles were assembled between the interdigitated electrodes using dielectrophoresis. At low temperatures, a TMR amplitude ranging from 0.6 -1.6 % was observed in the assembly of these particles which reduced to 0.3% at room temperature. Inset of Figure 1.2.11 (a) shows the TMR curve obtained in Fe nanocubes at 4 K. The typical shape of the TMR related to magnetization reversal could be observed at low field values. Beside, a high-field magnetoresistance could also be observed as shown in Figure 1.2.11(a). Similar high field magnetoresistance has been also reported in our lab in superlattices of FeCo, however, in that case high field magnetoresistance could reach up to 3000% [31].

The TMR in Fe nanocubes was found to be temperature dependent and decreased down by a factor of ~3 at room-temperature as evident from the Figure 1.2.11(b) and (d). On the other hand no significant difference was observed in the MR curves when the field was applied parallel and perpendicular to the plane as shown in Figure 1.2.11(c). With these results, the above mentioned organic ligands could be shown as effective tunnel barrier.

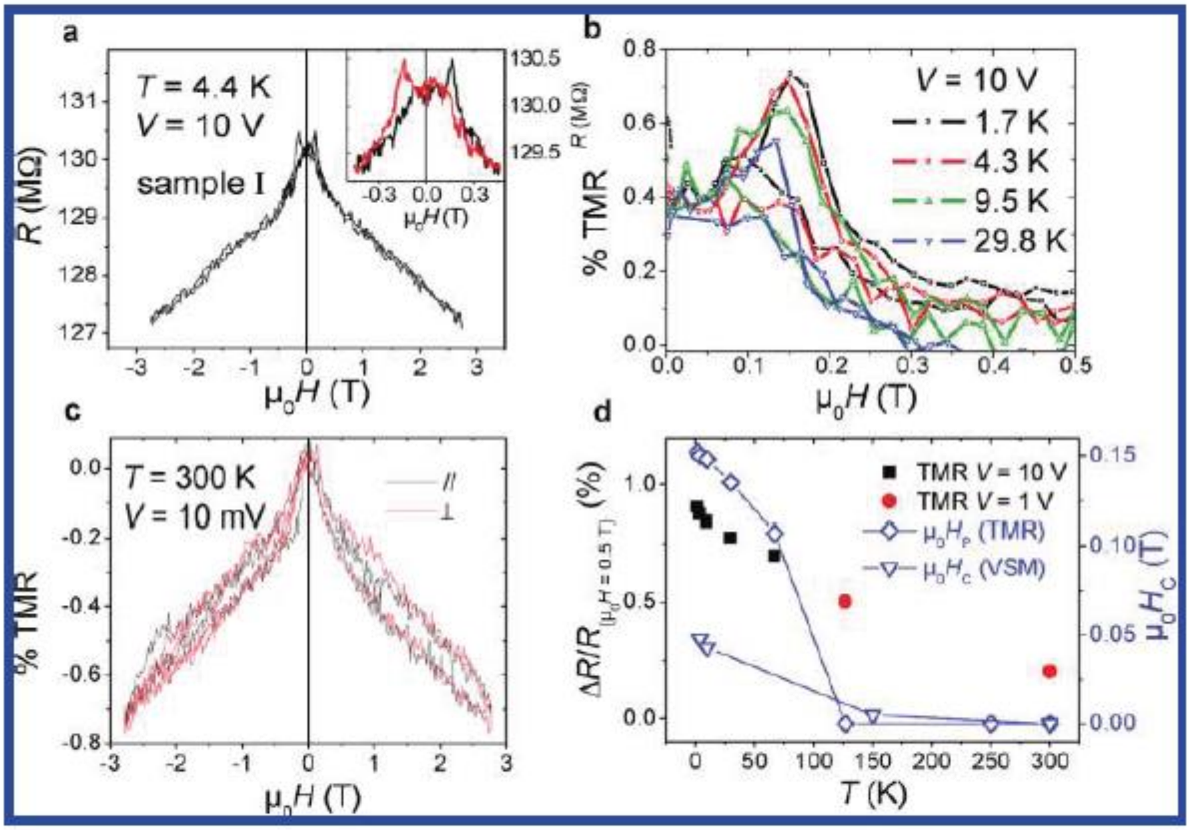

Figure 1.2.11: (a) TMR curve obtained in the case of Fe nanocubes at 4.4 K. Inset of the figure shows the low field region. (b) TMR curve at different temperature showing variation in amplitude. (c) TMR curve under the applied field direction plane and parallel to the plane of the assembly and (d) variation in the amplitude of TMR, TMR peaks and coercive field as a function of temperature. Reference [15].

During the course of this thesis, we have tried to improve on these results. As we shall present in chapter 3, our new results on FeCo particles have shown higher TMR ratio, which allowed us to study the effect of various parameter such as temperature, voltage, field direction and the mechanism of co-tunneling. However, we have observed some common features that has been shown in these previous studies. For example, presence of high-field MR that has been reported in assemblies of Fe and FeCo that were reported in previous studies has also been observed in our recent study. However, as we would show, the TMR amplitude is quite improved in new FeCo particles.

References: Chapter 1.2 Tunnel magnetoresistance

[1] M. Julliere, "Tunneling between ferromagnetic films," *Physics Letters A,* vol. 54, no. 3, pp. 225-226, 1975/09/08/ 1975.

[2] T. Miyazaki and N. Tezuka, "Giant magnetic tunneling effect in Fe/Al2O3/Fe junction," *Journal of Magnetism and Magnetic Materials,* vol. 139, no. 3, pp. L231-L234, 1995/01/02/ 1995.

[3] J. S. Moodera, L. R. Kinder, T. M. Wong, and R. Meservey, "Large Magnetoresistance at Room Temperature in Ferromagnetic Thin Film Tunnel Junctions," *Physical Review Letters,* vol. 74, no. 16, pp. 3273-3276, 04/17/ 1995.

[4] J. Inoue and S. Maekawa, "Theory of tunneling magnetoresistance in granular magnetic films," *Physical Review B,* vol. 53, no. 18, pp. R11927-R11929, 05/01/ 1996.

[5] J. S. Helman and B. Abeles, "Tunneling of Spin-Polarized Electrons and Magnetoresistance in Granular Ni Films," *Physical Review Letters,* vol. 37, no. 21, pp. 1429-1432, 11/22/ 1976.

[6] J. I. Gittleman, Y. Goldstein, and S. Bozowski, "Magnetic Properties of Granular Nickel Films," *Physical Review B,* vol. 5, no. 9, pp. 3609-3621, 05/01/ 1972.

[7] S. Mitani, H. Fujimori, and S. Ohnuma, "Spin-dependent tunneling phenomena in insulating granular systems," *Journal of Magnetism and Magnetic Materials,* vol. 165, no. 1, pp. 141-148, 1997/01/01/ 1997.

[8] M. Ohnuma, K. Hono, E. Abe, H. Onodera, S. Mitani, and H. Fujimori, "Microstructure of Co–Al–O granular thin films," *Journal of Applied Physics,* vol. 82, no. 11, pp. 5646-5652, 1997/12/01 1997.

[9] S. Takahashi and S. Maekawa, "Effect of Coulomb Blockade on Magnetoresistance in Ferromagnetic Tunnel Junctions," *Physical Review Letters,* vol. 80, no. 8, pp. 1758-1761, 02/23/ 1998.

[10] M. Pauly *et al.*, "Co-tunneling enhancement of the electrical response of nanoparticle networks," (in eng), *Small,* vol. 8, no. 1, pp. 108-15, Jan 9 2012.

[11] K. J. Dempsey *et al.*, "Cotunneling enhancement of magnetoresistance in double magnetic tunnel junctions with embedded superparamagnetic NiFe nanoparticles," *Physical Review B,* vol. 82, no. 21, p. 214415, 12/13/ 2010.

[12] S. S. P. Parkin *et al.*, "Exchange-biased magnetic tunnel junctions and application to nonvolatile magnetic random access memory (invited)," *Journal of Applied Physics,* vol. 85, no. 8, pp. 5828-5833, 1999/04/15 1999.

[13] S. Tehrani *et al.*, "Recent developments in magnetic tunnel junction MRAM," *IEEE Transactions on Magnetics,* vol. 36, no. 5, pp. 2752-2757, 2000.

[14] C. T. Black, C. B. Murray, R. L. Sandstrom, and S. Sun, "Spin-dependent tunneling in self-assembled cobalt-nanocrystal superlattices," (in eng), *Science,* vol. 290, no. 5494, pp. 1131-4, Nov 10 2000.

[15] J. Dugay *et al.*, "Room-Temperature Tunnel Magnetoresistance in Self-Assembled Chemically Synthesized Metallic Iron Nanoparticles," *Nano Letters,* vol. 11, no. 12, pp. 5128-5134, 2011/12/14 2011.

[16] R. P. Tan *et al.*, "Magnetoresistance and collective Coulomb blockade in superlattices of ferromagnetic CoFe nanoparticles," *Physical Review B,* vol. 79, no. 17, p. 174428, 05/21/ 2009.

[17] K. Liu, L. Zhao, P. Klavins, F. E. Osterloh, and H. Hiramatsu, "Extrinsic magnetoresistance in magnetite nanoparticles," *Journal of Applied Physics,* vol. 93, no. 10, pp. 7951-7953, 2003/05/15 2003.

[18] P. A. Kumar, S. Ray, S. Chakraverty, and D. D. Sarma, "Magnetoresistance and electroresistance effects in Fe3O4 nanoparticle system," *Journal of Experimental Nanoscience,* vol. 9, no. 4, pp. 391-397, 2014/04/01 2014.

[19] H. Zeng, C. T. Black, R. L. Sandstrom, P. M. Rice, C. B. Murray, and S. Sun, "Magnetotransport of magnetite nanoparticle arrays," *Physical Review B,* vol. 73, no. 2, p. 020402, 01/03/ 2006.

[20] C. Heiliger, P. Zahn, and I. Mertig, "Microscopic origin of magnetoresistance," *Materials Today,* vol. 9, no. 11, pp. 46-54, 2006/11/01/ 2006.

[21] P. M. Tedrow and R. Meservey, "Spin Polarization of Electrons Tunneling from Films of Fe, Co, Ni, and Gd," *Physical Review B,* vol. 7, no. 1, pp. 318-326, 01/01/ 1973.

[22] R. C. Sousa *et al.*, "Large tunneling magnetoresistance enhancement by thermal anneal," *Applied Physics Letters,* vol. 73, no. 22, pp. 3288-3290, 1998/11/30 1998.

[23] Y. Luo *et al.*, "Co-rich magnetic amorphous films and their application in magnetoelectronics," *Physical Review B,* vol. 72, no. 1, p. 014426, 07/13/ 2005.

[24] J. C. Slonczewski, "Conductance and exchange coupling of two ferromagnets separated by a tunneling barrier," *Physical Review B,* vol. 39, no. 10, pp. 6995-7002, 04/01/ 1989.

[25] O. Chayka, L. Kraus, P. Lobotka, V. Sechovsky, T. Kocourek, and M. Jelinek, "High field magnetoresistance in Co–Al–O nanogranular films," *Journal of Magnetism and Magnetic Materials,* vol. 300, no. 2, pp. 293-299, 2006/05/01/ 2006.

[26] B. J. Hattink, M. García del Muro, Z. Konstantinović, X. Batlle, A. Labarta, and M. Varela, "Tunneling magnetoresistance in $\mathrm{Co}\text{\ensuremath{-}}{\mathrm{ZrO}}_{2}$ granular thin films," *Physical Review B,* vol. 73, no. 4, p. 045418, 01/18/ 2006.

[27] C. Park, Y. Peng, J.-G. Zhu, D. E. Laughlin, and R. M. White, "Magnetoresistance of polycrystalline Fe3O4 films prepared by reactive sputtering at room temperature," *Journal of Applied Physics,* vol. 97, no. 10, p. 10C303, 2005/05/15 2005.

[28] D. D. Sarma *et al.*, "Intergranular Magnetoresistance in ${\mathrm{Sr}}_{2}{\mathrm{FeMoO}}_{6}$ from a Magnetic Tunnel Barrier Mechanism across Grain Boundaries," *Physical Review Letters,* vol. 98, no. 15, p. 157205, 04/12/ 2007.

[29] L. Savini *et al.*, "Observation of magnetoresistance in core–shell Fe–Fe oxide systems," *Journal of Applied Physics,* vol. 91, no. 10, pp. 8593-8595, 2002/05/15 2002.

[30] R. P. Tan, J. Carrey, and M. Respaud, "Voltage and temperature dependence of high-field magnetoresistance in arrays of magnetic nanoparticles," *Journal of Applied Physics,* vol. 104, no. 2, p. 023908, 2008/07/15 2008.

[31] R. P. Tan, J. Carrey, M. Respaud, C. Desvaux, P. Renaud, and B. Chaudret, "3000% high-field magnetoresistance in super-lattices of CoFe nanoparticles," *Journal of Magnetism and Magnetic Materials,* vol. 320, no. 6, pp. L55-L59, 2008/03/01/ 2008.

[32] R. P. Tan, J. Carrey, M. Respaud, C. Desvaux, P. Renaud, and B. Chaudret, "High-field and low-field magnetoresistances of CoFe nanoparticles elaborated by organometallic chemistry," *Journal of Applied Physics,* vol. 103, no. 7, p. 07F317, 2008/04/01 2008.

[33] C. H. Shang, J. Nowak, R. Jansen, and J. S. Moodera, "Temperature dependence of magnetoresistance and surface magnetization in ferromagnetic tunnel junctions," *Physical Review B,* vol. 58, no. 6, pp. R2917-R2920, 08/01/ 1998.

[34] A. Vedyayev, D. Bagrets, A. Bagrets, and B. Dieny, "Resonant spin-dependent tunneling in spin-valve junctions in the presence of paramagnetic impurities," *Physical Review B,* vol. 63, no. 6, p. 064429, 01/24/ 2001.

[35] A. H. MacDonald, T. Jungwirth, and M. Kasner, "Temperature Dependence of Itinerant Electron Junction Magnetoresistance," *Physical Review Letters,* vol. 81, no. 3, pp. 705-708, 07/20/ 1998.

[36] S. G. Wang, R. C. C. Ward, G. X. Du, X. F. Han, C. Wang, and A. Kohn, "Temperature dependence of giant tunnel magnetoresistance in epitaxial Fe/MgO/Fe magnetic tunnel junctions," *Physical Review B,* vol. 78, no. 18, p. 180411, 11/17/ 2008.

[37] H. Kumar *et al.*, "Role of Coulomb blockade and spin-flip scattering in tunneling magnetoresistance of FeCo-Si-O nanogranular films," *Journal of Applied Physics,* vol. 109, no. 7, p. 073914, 2011/04/01 2011.

[38] A. Sarkar, R. Adhikari, N. Behera, and A. K. Das, "Self-grown core/shell nanoparticles of cobalt: Correlation of structure, transport and magnetism," *Journal of Magnetism and Magnetic Materials,* vol. 339, no. Supplement C, pp. 20-29, 2013/08/01/ 2013.

[39] R. Meservey and P. M. Tedrow, "Spin-polarized electron tunneling," *Physics Reports,* vol. 238, no. 4, pp. 173-243, 1994/03/01/ 1994.

[40] T. Zhu and Y. J. Wang, "Enhanced tunneling magnetoresistance of ${\mathrm{F}\mathrm{e}\ensuremath{-}\mathrm{A}\mathrm{l}}_{2}{\mathrm{O}}_{3}$ granular films in the Coulomb blockade regime," *Physical Review B,* vol. 60, no. 17, pp. 11918-11921, 11/01/ 1999.

[41] S. Zhang, P. M. Levy, A. C. Marley, and S. S. P. Parkin, "Quenching of Magnetoresistance by Hot Electrons in Magnetic Tunnel Junctions," *Physical Review Letters,* vol. 79, no. 19, pp. 3744-3747, 11/10/ 1997.

[42] J. S. Moodera, J. Nowak, and R. J. M. van de Veerdonk, "Interface Magnetism and Spin Wave Scattering in Ferromagnet-Insulator-Ferromagnet Tunnel Junctions," *Physical Review Letters,* vol. 80, no. 13, pp. 2941-2944, 03/30/ 1998.

[43] J. Zhang and R. M. White, "Voltage dependence of magnetoresistance in spin dependent tunneling junctions," *Journal of Applied Physics,* vol. 83, no. 11, pp. 6512-6514, 1998/06/01 1998.

[44] W. Wulfhekel, H. F. Ding, and J. Kirschner, "Tunneling magnetoresistance through a vacuum gap," *Journal of Magnetism and Magnetic Materials,* vol. 242-245, pp. 47-52, 2002/04/01/ 2002.

[45] D. V. Averin and Y. V. Nazarov, "Virtual electron diffusion during quantum tunneling of the electric charge," (in eng), *Phys Rev Lett,* vol. 65, no. 19, pp. 2446-2449, Nov 5 1990.

[46] S. Mitani, S. Takahashi, K. Takanashi, K. Yakushiji, S. Maekawa, and H. Fujimori, "Enhanced Magnetoresistance in Insulating Granular Systems: Evidence for Higher-Order Tunneling," *Physical Review Letters,* vol. 81, no. 13, pp. 2799-2802, 09/28/ 1998.

[47] T. B. Tran, I. S. Beloborodov, X. M. Lin, T. P. Bigioni, V. M. Vinokur, and H. M. Jaeger, "Multiple Cotunneling in Large Quantum Dot Arrays," *Physical Review Letters,* vol. 95, no. 7, p. 076806, 08/12/ 2005.

[48] T. B. Tran, I. S. Beloborodov, J. Hu, X. M. Lin, T. F. Rosenbaum, and H. M. Jaeger, "Sequential tunneling and inelastic cotunneling in nanoparticle arrays," *Physical Review B,* vol. 78, no. 7, p. 075437, 08/26/ 2008.

1.3 Spin cross-over complexes

1.3.1 Introduction

In the previous section, we focused our attention on magnetic materials which find wide range of applications in spintronic devices due to their remarkable magnetic and transport properties. In this section, we shall present another class of material, known as spin cross-over (SCO) complexes which possess unique, but equally important magnetic and transport properties. SCO complexes are basically co-ordination complexes of d^4-d^7 transition metals which are capable of switching between two magnetic states known as high spin and low spin state. A high spin state is characterized by more unpaired electrons in the *d*-orbitals and consequently a higher magnetic moment; whereas a low spin state have less or no unpaired electron and thus, low magnetic moment. Due to the switching between HS and LS state, they are often categorized as molecular switches. In most cases, a reversible switching between the two states can be brought about by subjecting the SCO complexes to an external stimulus. Most commonly used stimuli are temperature, pressure, and light. The phenomenon of switching between HS and LS is referred as spin transition or spin crossover and could be gradual or abrupt depending on the SCO complex.

Early studies on SCO complexes can be traced back to early 1930s when Cambi *et al*. reported on magnetic moments of certain dithiocarbamato complexes of Fe (III). At room temperature, magnetic moment of these complexes corresponded to five unpaired electrons, while on cooling the complex, magnetic moment corresponded to only one unpaired electron [1-3]. It was suggested that Fe (III) could exhibit two magnetic states with high and low magnetic moments, which were named as high spin (HS) and low spin (LS) state respectively. Since then, a large number of SCO complexes have been reported which include complexes of Fe (II), Ni (II), Co (II), and Mn (II) coordinated to a variety of ligands [4-7]. So far, largest number of SCO complexes has been reported for Fe (II) [8, 9]. Spin transition in SCO complexes is accompanied by changes in different physical properties. It has been shown that dielectric properties [10], transport properties [11], heat capacity and optical properties [12] may also differ in HS and LS state. Due to their switching behavior, SCO complexes have been proposed for various applications in modern devices which include pressure and temperature sensors , memory devices [13], optoelectronic devices [14] etc. The trend in the miniaturization of materials down to nanoscale has gained much popularity in the family of SCO complexes, which has resulted in increased research interest. Spin transition in SCO complexes in the form of thin films and nanoparticles have been studied extensively [15].

In the following sections, we shall present the basic aspects of spin transition. We shall begin with ligand field theory, which would provide an insight to the spin transition phenomenon. We shall then move our attention to thermally induced spin transition and its magnetic detection. Although spin transition is reported in several transition metal complexes, we shall mainly focus on the complexes of Fe (II). Hybrid structures consisting of metallic nanoparticles and SCO molecules have been proposed to tailor the transport properties of SCO complexes. We shall briefly discuss the charge transport properties in such a system.

1.3.2 Ligand Field theory

We mentioned previously that SCO complexes have d^4-d^7 electronic configuration. However, not all the transition metal complexes with d^4-d^7 undergo spin transition. Complexes which remain exclusively in HS state or LS state over wide range of temperature are also known. Ligand field theory can be used to explain why certain complexes could show thermally induced switching between HS and LS state while others do not. It considers the effect of ligand field (electrostatic field exerted on the metal ion by the ligand molecules) on the *d*-orbitals of the metal ion. Let us take an example of an octahedral Fe (II) complex. Before the formation of the complex, iron would exist in the form of Fe^{+2} ion with its five degenerate *d*-orbitals i.e. d_x, d_y, d_z, d_{x2-y2} and d_{z2}. For the formation of an octahedral complex, six ligand molecules would approach towards Fe^{+2} ion. During this process, each ligand molecule exerts a field on the five 3*d*-orbitals and break their degeneracy. As a result, the 3*d*- orbital split into two energy levels: a non-bonding t_{2g} level with lower energy and an antibonding e_g level with higher energy. A schematic diagram of *d*-orbital splitting is shown in figure 1.3.1. The difference of energy between two levels depends on the nature of the ligands and the central metal ion and is determined experimentally. The energy difference is often called splitting energy denoted by 10Dq. For a given metal ion, a strong ligand field would cause larger splitting and high 10Dq value whereas for weak ligands, the opposite is true.

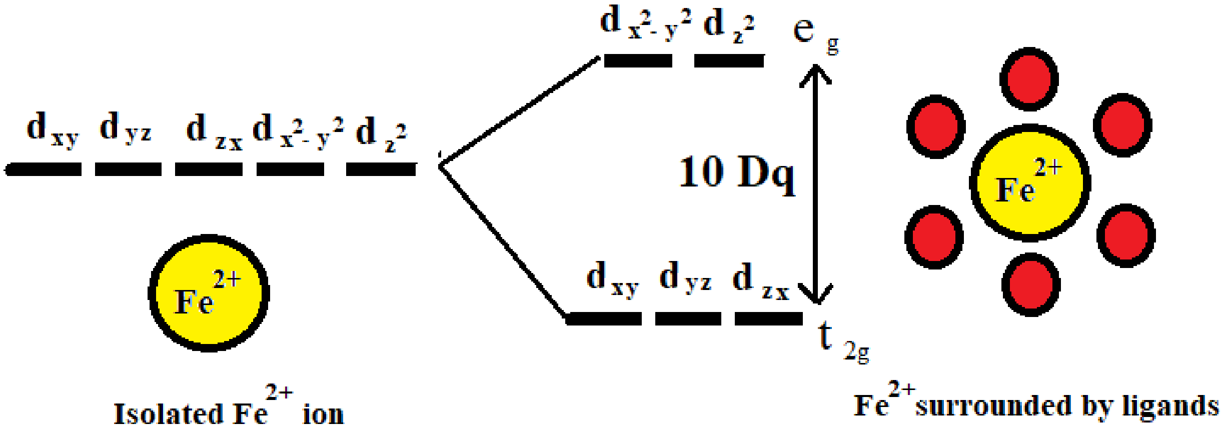

Figure 1.3.1: A schematic diagram showing degenerate *d*-orbitals in an isolated Fe^{2+} ion in the absence of ligands (left) and splitting of *d*-orbitals in t_{2g} and e_g levels in the presence of ligands (right).

The arrangement of six *3d* electrons in the two levels determines whether the complex would exhibit a HS state or a LS state at a given temperature. The first three electrons reside in t_{2g} level with each orbital occupying one electron as per Hund's rule. At this point, the role of pairing energy comes into play as the remaining electrons can occupy either t_{2g}, or e_g level depending on the competition between 10Dq and pairing energy. The two possible scenarios which occur are as follows:

(i) **When 10Dq > pairing energy**

When the splitting energy is larger than pairing energy, the remaining electron starts to pair up with electrons in t_{2g} level. As a result, all the six electrons reside in the t_{2g} level making a $t_{2g}^6\ e_g^0$ configuration as shown in figure 1.3.2. Since there is no unpaired electron, the complex would show diamagnetic nature, which is the low spin state of Fe (II) complexes. For example, $[Fe(CN)_6]^{4-}$ is diamagnetic in nature due to high 10Dq value caused by the strong CN^- ligand.

(ii) **When 10Dq < pairing energy**

When pairing energy is larger than 10Dq, occupancy of e_g level is preferred by the remaining electrons. Thus, the fourth and the fifth electron reside in the e_g levels. However, pairing is unavoidable for the sixth electron. In this case, pairing occur in one of the orbital in t_{2g} level. This results in a $t_{2g}^4\ e_g^2$ configuration as shown in figure 1.3.2. Since the final configuration has 4 unpaired electrons, the complex would show a paramagnetic nature, which is the high spin state of Fe (II) complexes. For example, $[Fe(H_2O)_6]^{2+}$ is paramagnetic in nature due to low 10Dq value caused by the weak H_2O ligand.

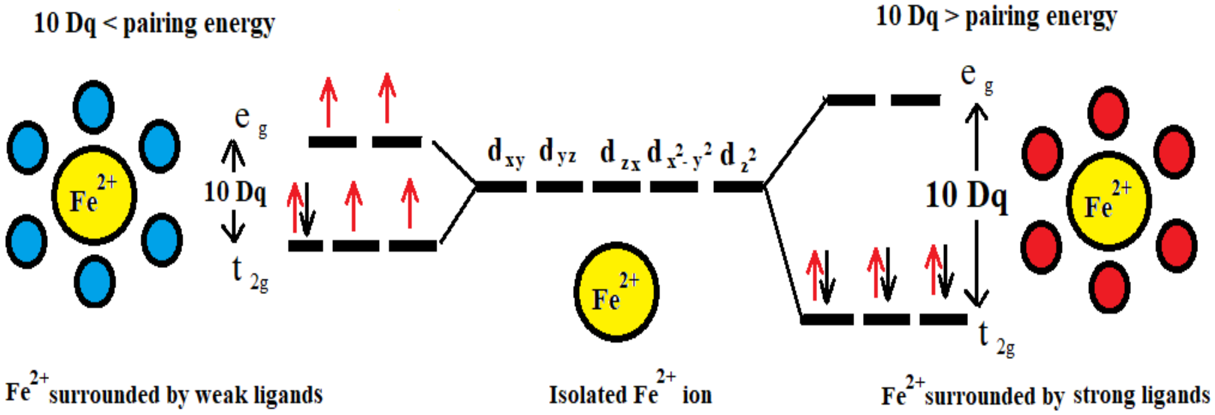

Figure 1.3.2: A schematic diagram of distribution of six *d*-orbital electron in Fe^{2+} in case of weak ligands which results in four unpaired electron (left) and strong ligands which results in zero unpaired electron.

.

1.3.2 Thermally induced spin transition

In certain SCO complexes, the difference in Gibbs free energy for the two spin states (HS and LS) is of the order of thermal energy. In such a case, a transition between HS and LS can be induced by varying the temperature [16]. In fact, it is one of the most common ways for inducing the transition and can be observed in most of the Fe (II) complexes. Several Fe (II) complexes have been reported to show spin transition near room temperature which is a desirable property for most functional devices. During a thermally induced transition, the two spin states are in thermodynamic competition with each other and an increase in temperature favors the HS state. Consequently, the mole fraction of HS state increases with increase in temperature.

(a) Types of transition

The range of temperature over which transition takes place varies significantly from complex to complex. In solid materials, electronics and structural changes accompanying the spin transition propagate throughout the materials through short and long range interactions. The extent of these effects depends on the complex and significantly influences the spin transition. One way to follow the thermally induced spin transition is to study the variation in mole fraction of HS state (γ_{HS}) as a function of temperature. Some of the observed thermal transition behaviors are as follows:

(i) **Gradual transition**: A gradual spin transition takes place over a wide range of temperature. It is often associated with low cooperativity in the complex molecule. In the absence of cooperativity, spin transition follows simple Boltzmann distribution over all of energy levels involved. Figure 1.3.3 (a) shows a typical gradual spin transition curve.

(ii) **Abrupt transition**: An abrupt transition in the complex takes place over a narrow range of temperature and is due to high cooperativity in the complex. Figure 1.3.3 (b) shows a sketch of an abrupt transition.

(iii) **Abrupt and hysterical**: A hysteresis in the spin transition could arise due to the intramolecular structural changes that takes place along with the transition and communicated to the neighboring molecules due to the high cooperativity. It is often associated with the structural phase changes in the lattice. Figure 1.3.3 (c) shows a sketch of spin transition exhibiting a hysterical behavior.

(iv) **Step-wise:** Presence of two or more chemically non-equivalent iron centers in the crystal packing can give rise to a step in the spin transition as shown in figure 1.3.3 (d). It is attributed to the different transition temperature of the non-equivalent iron centers.

(v) **Incomplete transition:** Presence of an impurity at lattice site may prevent the formation of a pure HS or LS state. This may result in an incomplete transition. Beside, an extremely low conversion rate can also result in an incomplete transition as shown in figure 1.3.3 (e).

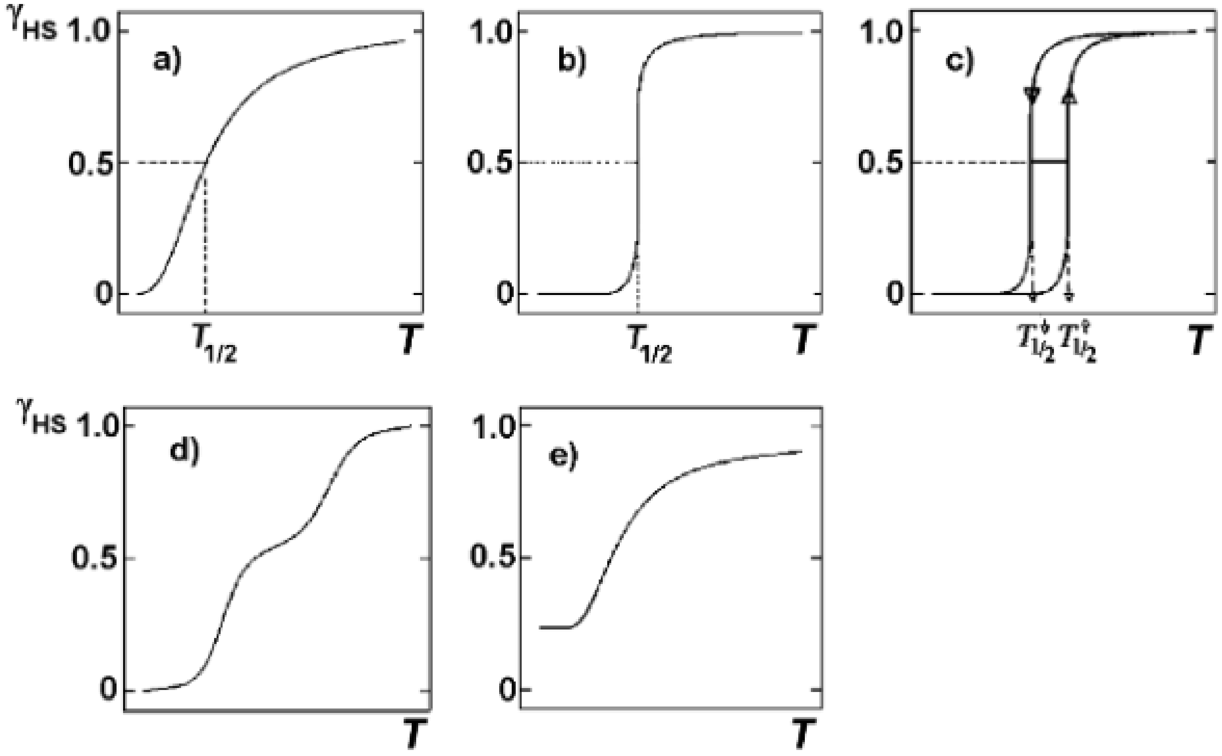

Figure 1.3.3: Thermally induced transition in SCO complexes showing (a) gradual (b) abrupt (c) hysterical (d) step-wise and (e) incomplete transition. [Reference [16]]

(b) Magnetic detection of Spin-transition

The fact that magnetic moment of HS and LS state differ from each other is exploited for the detection of thermally induced spin transition in SCO complexes. Magnetic detection is particularly suited for Fe (II) complexes as the magnetic moment of their HS state (paramagnetic) is significantly higher than the LS state (diamagnetic). As a result, a drastic change in the magnetic susceptibility occurs during the spin transition. When the susceptibilities of both spin states is known, the mole fraction of the HS state can be obtained by using the following equation

$$\chi(T) = \gamma_{HS}\chi_{HS} + (1 - \gamma_{HS})\chi_{LS} \qquad 1.3\,(a)$$

where $\chi(T)$ is the susceptibility of the SCO complex which varies with temperature, χ_{LS} and χ_{HS} being the temperature independent susceptibility of pure LS and HS state.

When the exact value of χ_{LS} and χ_{HS} are not known, a quantity of interest is the product of molar magnetic susceptibility and temperature. As per the Curie's law, the molar susceptibility should vary as *C/T* for Fe (II). Thus, the product χT should remain constant as long as the complex remains in high spin state and decrease during transition to low spin state. For Fe (II), χT varies from 3 $cm^3 K\ mol^{-1}$ for HS to close to 0 for low spin. The deviation in these values may occur due to incomplete transition or error in estimation of metal mole number in a given complex. Figure 1.3.4 (a) shows χT product as a function of temperature for a triazole based Fe (II) complex [17]. Note that the spin transition occurs near room temperature and shows a hysteresis of roughly 20 K.

Reducing a material size from bulk to nanoscale may cause changes in its spin-transition behavior. In case of the [Fe(pz) [18]] complex (pz=pyrazoly), an abrupt transition is observed for bulk whereas nanocrystals of the same complex exhibit gradual and incomplete transition without hysteresis as shown in figure 1.3.4 (b).[Reference [19]].

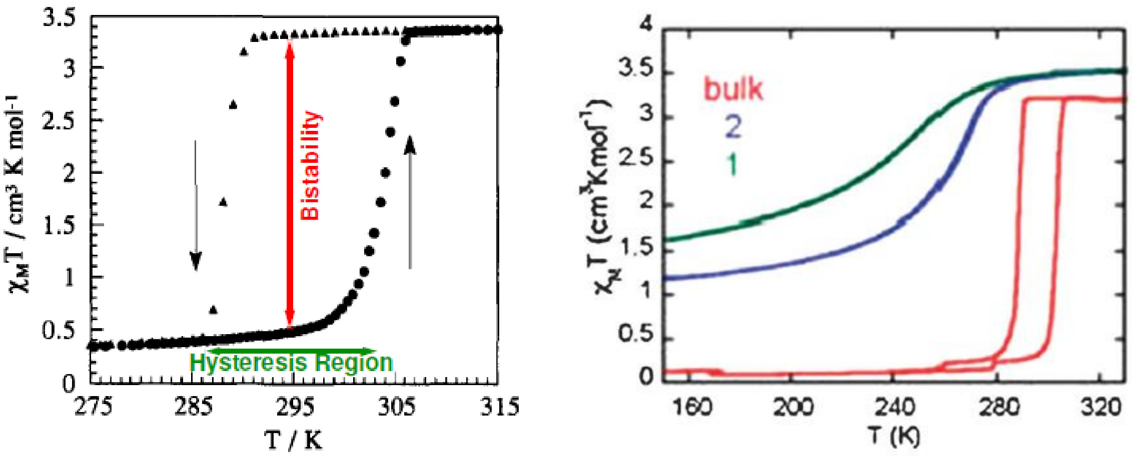

Figure 1.3.4: (a) Variation of χT product during the spin transition complex for a triazole based Fe (II) complex showing an abrupt spin-transition with hysteresis [Reference [17]]. (b) Different spin transition behavior observed in [Fe(pz) Pt{(CN)4}] for bulk (red) and nano-size crystals of dimensions 8x8x3 nm^3 (green) and 15x15x5 (blue) nm^3 [Reference [19]].

Magnetic measurements are widely used to detect the thermally induced spin transition. However, other commonly employed techniques involves optical, vibrational and Mössbauer spectroscopy. A detail insight on these methods is reviewed in reference [12]

1.3.3 Transport properties of spin cross-over complexes

The effect of switching between HS and LS can be observed in charge transport properties of SCO complexes. Several studies have reported a change in conductivity of the SCO complex as the transition takes place. Salmon *et al*. [20] have investigated the spin transition in the Fe (II) complex formed with hydrotris(1-pyrazolyl)borate ligand, $[Fe(HB(pz)_3)_2]$, where pz = pyrazolyl. The spin transition in this complex could be induced thermally in the range of 450 K to 300 K as evident from figure 1.3.5(a) which shows a decrease in χT product from approximately 3 to almost zero $cm^3mol^{-1}K$. However, the transition during the first heating was found to be partially abrupt while the following cycles showed gradual transition. Such an effect could occur due to the crystallographic changes from tetragonal to monoclinic structure. Electrical measurement performed on a powder sample showed that temperature variation of a.c. conductivity could be correlated to spin transition. As shown in figure 1.3.5 (b), during the first heating (shown in hollow red square), the conductivity increases with temperature up to approximately 360 K followed by a gradual decrease and then an abrupt drop. The subsequent cycles show different behavior compared to the first cycle as observed in magnetic measurements. It could be concluded that increasing the temperature from 250K causes the increase in the conductivity of the LS state, but above ~360K the LS to HS transition counterbalance the effect of thermal activation. For this complex, it could be shown that LS state is more conducting than HS state. Salmon *et al.* proposed that charge transport in this complex takes place through hopping mechanism.

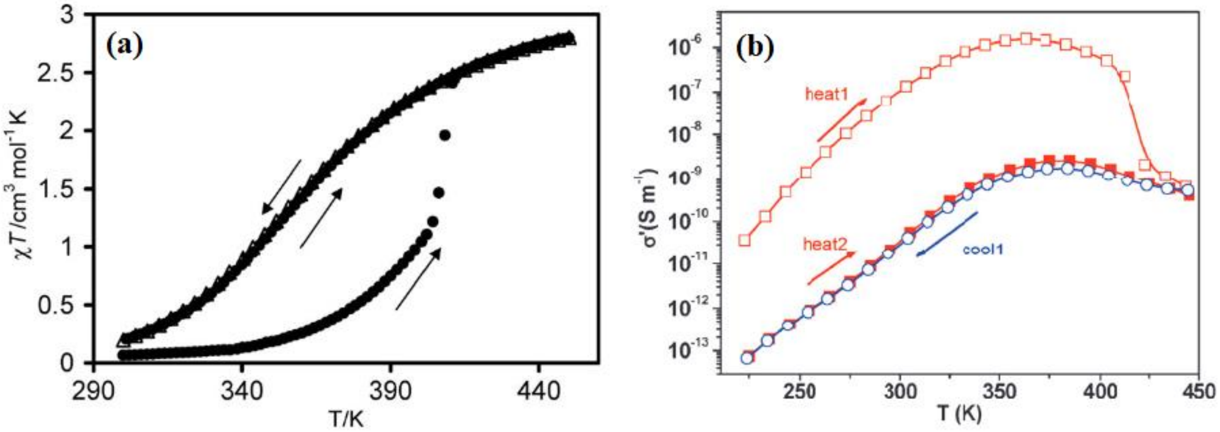

Figure 1.3.5 (a) A plot of χT versus temperature showing the partially abrupt spin transition during first heating (solid circles) and gradual spin transition in subsequent cycles (triangles) for $[Fe(HB(pz)_3)_2]$ bulk sample (b) temperature variation of a.c. conductivity of the same complex showing a spin transition related behavior. [Reference [20].

Rotaru *et al*. [21] studied the electrical conductivity in $[Fe(Htrz)_2(trz)]BF_4$ complex prepared chemically by three different ways. In one of the synthesis, they obtained micrometer size needle-like crystallite (C2) while in other two syntheses; roughly spherical (C1) and rod-like (C3) nano-size structures were obtained. In all the three samples, d.c. conductivity showed hysterical behavior with respect to temperature as shown in figure 1.3.6 (a), (b), and (c). This behavior was attributed to the spin transition which was also confirmed by optical spectroscopy. The HS state was found to be less conducting than LS state in all the cases. Ln conductance versus inverse temperature curves for C1 and C2 showed a linear behavior in both HS and LS state. This allowed the evaluation of charging energy in both cases for both states. For C1, activation energies were found to be 0.34 *eV* in LS and 0.52 *eV* for HS state. On the other hand, C2 showed 0.52 *eV* for LS and 0.87 *eV* for HS. Figure 1.3.6 (d) and (e) show the Arrhenius plot of conductivity for C1 and C2 respectively.

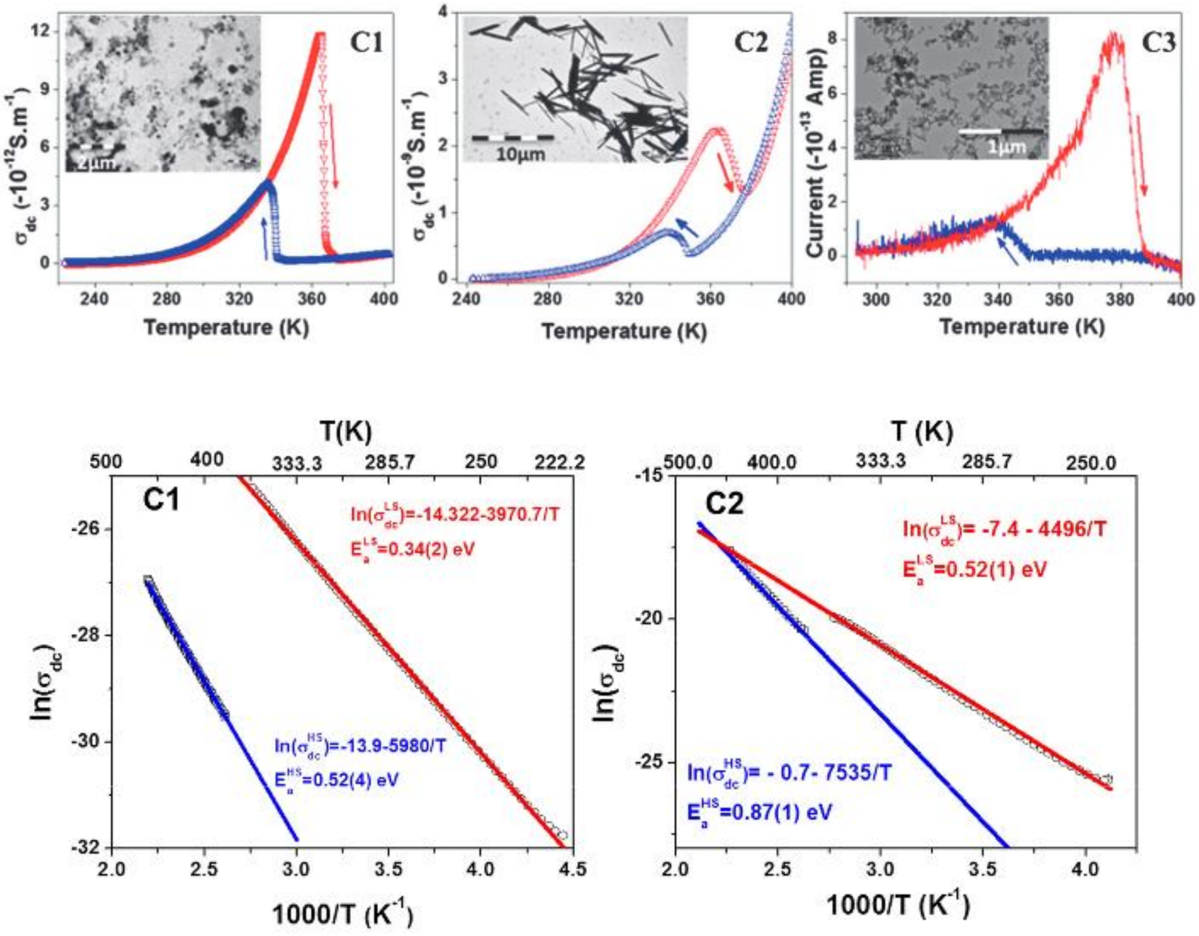

Figure 1.3.6 Temperature dependence of conductivity for the complex in the form of (a) nano-size sphere, (b) micro-meter size needles and (c) nano-size rods. The inset shows their respective TEM images. Arrhenius plots of conductivity in LS and HS state for (d) nano-size sphere and (e) mico-size needles. [Reference [21] : article and supporting information].

A major challenge faced during the investigation of electrical properties of nanostructure SCO complexes is their integration in the device. Dielectrophoresis is often used to trap various types of nanostructures between the electrodes whereby an a.c. voltage is applied while drop casting the particles. Rotaru *et al*. [22] used dielectrophoresis to organize [Fe(Htrz)$_2$ (trz)](BF$_4$) (Htrz = 1H-1,2,4-triazole) rods between interdigitated electrodes. Figure 1.3.7 (a) shows a schematic representation of the process where the micro-size rods are forced to align between the electrodes due to the field gradient. As evident from the SEM images [figure 1.3.7 (c) and (d)], the SCO rods are well aligned between the interdigitated electrodes.

Charge transport studies show a hysteresis in current with respect to temperature in the range of 350 K to 390 K approximately which is attributed to the HS↔LS switching. In agreement with their previous studies, Rotaru *et al*. observed LS state to be more conducting than HS state.

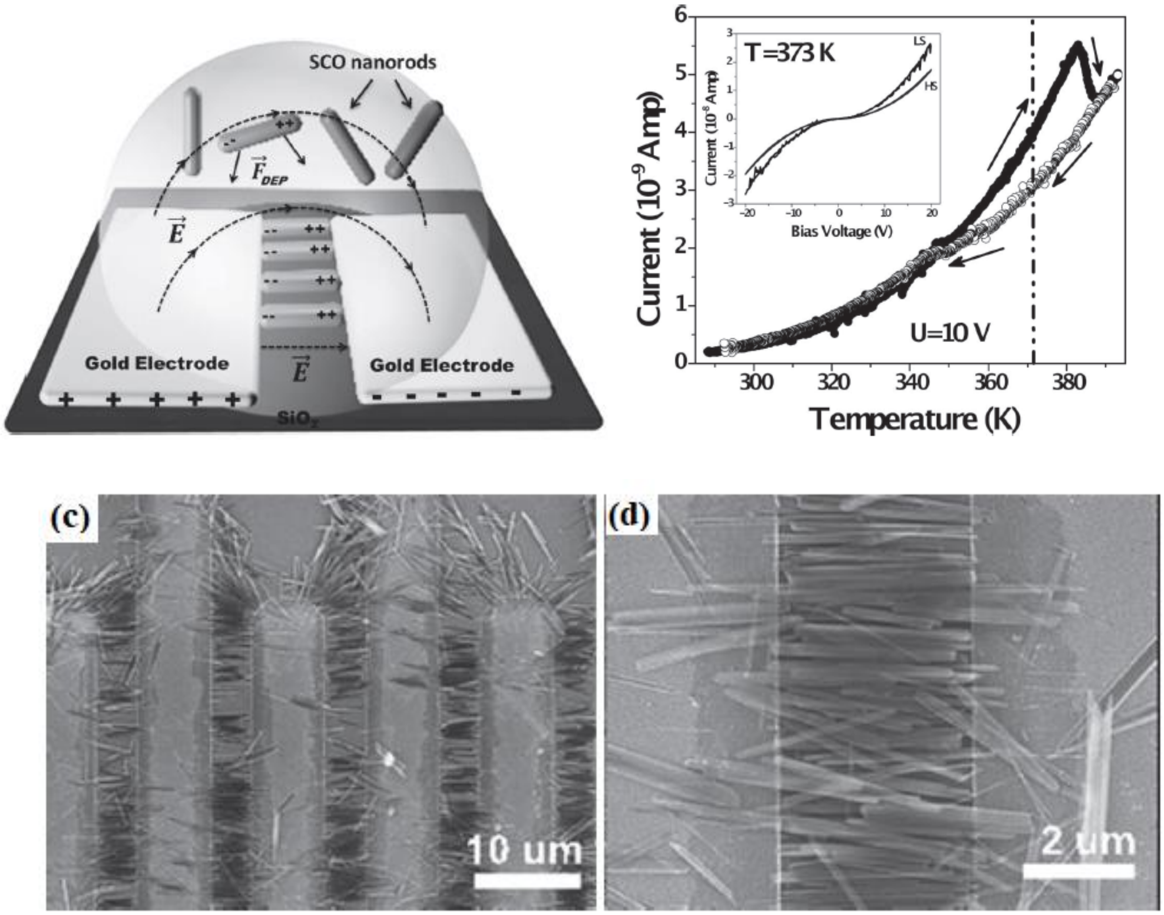

Figure1.3.7 (a) A schematic representation of dielecrophoresis showing the direction of the electric field and force acting on SCO micro-rods (b) Current-temperature curve showing a hysteresis attributed to the HS↔LS switching while the inset shows the *I-V* curves at ~370K during heating (for LS state) and cooling (for HS state). (c) SEM images showing interdigitated electrodes gaps filled with SCO rods (d) zoomed-in SEM imaged showing well aligned SCO rods between the electrodes. [Reference [22].

Another major challenge that is often faced while investigating the charge transport properties in SCO complexes is their high resistivity. Hybrid nanostructures of SCO complexes and metallic nanoparticles have been proposed to overcome such a problem. Hypothetically, such hybrid materials could manifest improved conductivity with a switching behavior related to spin transition. However, whether the spin transition can persist in SCO nanostructures in the vicinity of an external entity needs to be addressed. Devid *et al*. [23] investigated the spin transition in an array of gold nanoparticles over which $[Fe(AcS\text{-}BPP)_2](ClO_4)_2$ –where AcS-BPP denotes (S)-(4-{[2,6-(dipyrazol-1-yl)pyrid-4-yl]ethynyl}phenyl)ethanethioate) – complex molecules were grafted. Grafting of SCO molecules over nanoparticle surfaces was carried out by using a ligand exchange approach which results in a partial grafting of particles surface with SCO molecules and the rest of the surface with an alkyl thiol. Figure 1.3.8 (a) shows the schematic diagram of particles covered with SCO molecules as well as with alkyl thiol molecules.

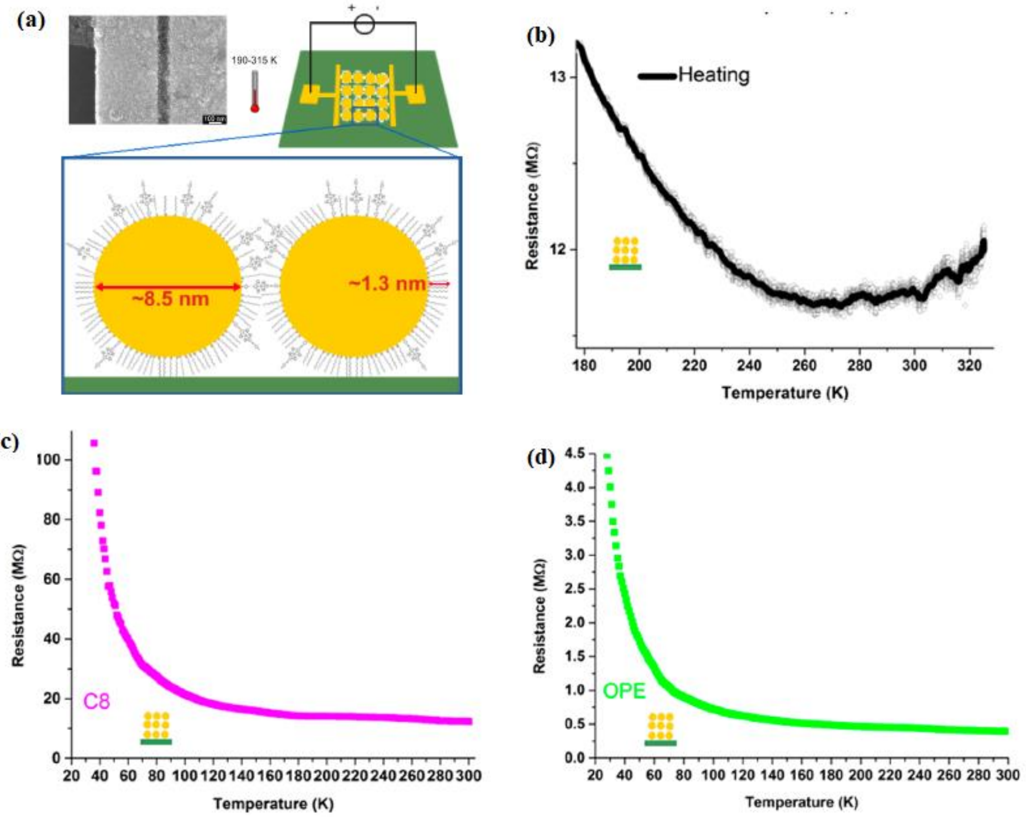

Figure 1.3.8 (a) SEM image of the device showing the SCO coated gold nanoparticle assembly between the electrodes (left) and a schematic diagram of the assembly and the particle surface. (b) Variation of resistance for the same assembly showing an increase in resistance above 280 K (c) Variation in resistance of particles coated with octane thiol and (d) OPE molecules. [Reference [23]]

Charge transport measurements were performed on 2d arrays of gold nanoparticles coated with (a) two passive molecules including OPE (oligo(phenylene)(ethynylene) and octanethiol (C8)) which are not supposed to exhibit spin transition, and (b) SCO molecule mentioned above. The arrays in the former case showed a decrease in resistance with increase in temperature, as shown in figure 1.3.8 (c) and (d), whereas in later case, a minima was observed in the resistance as shown in figure 1.3.8 (b). The increase in resistance above 280 K was attributed to the spin transition. These charge transport results were also supported by DFT calculations for the array of gold particles coated with SCO molecules.

References: Chapter 1.3 Spin cross-over complexes

[1] L. Cambi and L. Szegö, "Über die magnetische Susceptibilität der komplexen Verbindungen," *Berichte der deutschen chemischen Gesellschaft (A and B Series),* vol. 64, no. 10, pp. 2591-2598, 1931.

[2] L. Cambi and L. Szegö, "Über die magnetische Susceptibilität der komplexen Verbindungen (II. Mitteil.)," *Berichte der deutschen chemischen Gesellschaft (A and B Series),* vol. 66, no. 5, pp. 656-661, 1933.

[3] L. Cambi and L. Malatesta, "Magnetismus und Polymorphie innerer Komplexsalze: Eisensalze der Dithiocarbamidsäuren," *Berichte der deutschen chemischen Gesellschaft (A and B Series),* vol. 70, no. 10, pp. 2067-2078, 1937.

[4] C. N. R. Rao, M. M. Seikh, and C. Narayana, "Spin-State Transition in LaCoO3 and Related Materials," in *Spin Crossover in Transition Metal Compounds II*, P. Gütlich and H. A. Goodwin, Eds. Berlin, Heidelberg: Springer Berlin Heidelberg, 2004, pp. 1-21.

[5] H. A. Goodwin, "Spin Crossover in Cobalt(II) Systems," in *Spin Crossover in Transition Metal Compounds II*, P. Gütlich and H. A. Goodwin, Eds. Berlin, Heidelberg: Springer Berlin Heidelberg, 2004, pp. 23-47.

[6] Y. Garcia and P. Gütlich, "Thermal Spin Crossover in Mn(II), Mn(III), Cr(II) and Co(III) Coordination Compounds," in *Spin Crossover in Transition Metal Compounds II*, P. Gütlich and H. A. Goodwin, Eds. Berlin, Heidelberg: Springer Berlin Heidelberg, 2004, pp. 49-62.

[7] S. Thies *et al.*, "Coordination-Induced Spin Crossover (CISCO) through Axial Bonding of Substituted Pyridines to Nickel–Porphyrins: σ-Donor versus π-Acceptor Effects," *Chemistry – A European Journal,* vol. 16, no. 33, pp. 10074-10083, 2010.

[8] E. König, "Structural Changes Accompanying Continuous and Discontinuous Spin-State Transitions," in *Progress in Inorganic Chemistry*: John Wiley & Sons, Inc., 2007, pp. 527-622.

[9] P. Gutlich, Y. Garcia, and H. A. Goodwin, "Spin crossover phenomena in Fe() complexes," *Chemical Society Reviews,* 10.1039/B003504L vol. 29, no. 6, pp. 419-427, 2000.

[10] A. Bousseksou, G. Molnar, P. Demont, and J. Menegotto, "Observation of a thermal hysteresis loop in the dielectric constant of spin crossover complexes: towards molecular memory devices," *Journal of Materials Chemistry,* 10.1039/B306638J vol. 13, no. 9, pp. 2069-2071, 2003.

[11] C. Lefter *et al.*, "Charge Transport and Electrical Properties of Spin Crossover Materials: Towards Nanoelectronic and Spintronic Devices," *Magnetochemistry,* vol. 2, no. 1, p. 18, 2016.

[12] P. Gütlich, A. B. Gaspar, and Y. Garcia, "Spin state switching in iron coordination compounds," (in en), *Beilstein Journal of Organic Chemistry 9:39,* Review vol. 9, 2013/02/15 2013.

[13] O. Kahn and C. J. Martinez, "Spin-Transition Polymers: From Molecular Materials Toward Memory Devices," *Science,* 10.1126/science.279.5347.44 vol. 279, no. 5347, p. 44, 1998.

[14] M. Matsuda, K. Kiyoshima, R. Uchida, N. Kinoshita, and H. Tajima, "Characteristics of organic light-emitting devices consisting of dye-doped spin crossover complex films," *Thin Solid Films,* vol. 531, no. Supplement C, pp. 451-453, 2013/03/15/ 2013.

[15] A. Bousseksou, G. Molnar, L. Salmon, and W. Nicolazzi, "Molecular spin crossover phenomenon: recent achievements and prospects," *Chemical Society Reviews,* 10.1039/C1CS15042A vol. 40, no. 6, pp. 3313-3335, 2011.

[16] P. Gütlich, A. Hauser, and H. Spiering, "Thermal and Optical Switching of Iron(II) Complexes," *Angewandte Chemie International Edition in English,* vol. 33, no. 20, pp. 2024-2054, 1994.

[17] J. Krober, E. Codjovi, O. Kahn, F. Groliere, and C. Jay, "A spin transition system with a thermal hysteresis at room temperature," *Journal of the American Chemical Society,* vol. 115, no. 21, pp. 9810-9811, 1993/10/01 1993.

[18] F. Dassenoy *et al.*, "Platinum nanoparticles stabilized by CO and octanethiol ligands or polymers: FT-IR, NMR, HREM and WAXS studies," *New Journal of Chemistry,* 10.1039/A709245H vol. 22, no. 7, pp. 703-712, 1998.

[19] F. Volatron, L. Catala, E. Rivière, A. Gloter, O. Stéphan, and T. Mallah, "Spin-Crossover Coordination Nanoparticles," *Inorganic Chemistry,* vol. 47, no. 15, pp. 6584-6586, 2008/08/01 2008.

[20] L. Salmon *et al.*, "Re-investigation of the spin crossover phenomenon in the ferrous complex [Fe(HB(pz)3)2]," *New Journal of Chemistry,* 10.1039/B902811K vol. 33, no. 6, pp. 1283-1289, 2009.

[21] A. Rotaru, I. y. A. Gural'skiy, G. Molnar, L. Salmon, P. Demont, and A. Bousseksou, "Spin state dependence of electrical conductivity of spin crossover materials," *Chemical Communications,* 10.1039/C2CC30528C vol. 48, no. 35, pp. 4163-4165, 2012.

[22] A. Rotaru *et al.*, "Nano-electromanipulation of Spin Crossover Nanorods: Towards Switchable Nanoelectronic Devices," *Advanced Materials*, vol. 25, no. 12, pp. 1745-1749, 2013.

[23] E. J. Devid *et al.*, "Spin Transition in Arrays of Gold Nanoparticles and Spin Crossover Molecules," *ACS Nano,* vol. 9, no. 4, pp. 4496-4507, 2015/04/28 2015.

Chapter 2: Tuning Coulomb blockade in assemblies of nanoparticles

2.1 Introduction

In chapter 1.1, we presented a few relevant studies on Coulomb blockade in nano-structures, discussed various parameters that can influence charging energy in arrays of particles, and how they can be advantageous for the tuning of Coulomb blockade. Presence of Coulomb blockade at room-temperature is a desirable feature in assemblies of nanoparticle from their application point of view as well as for the fundamental studies. Although certain assemblies are capable to show room-temperature Coulomb blockade [1, 2], a majority of them requires low-temperature for blockade to occur [3-7]. In this regard, more systems should be prepared that can show Coulomb blockade at room-temperature. At the same time, systems which can offer the possibility of tuning the Coulomb blockade are also important in order to have better control over the phenomenon. Assemblies of chemically prepared core-shell nanoparticles offer not only the possibility to observe Coulomb blockade at room-temperature but also the means of tuning it.

During the course of this thesis, we have studied Coulomb blockade in assemblies of chemically synthesized ultra-fine platinum nanoparticles. These assemblies have interesting features for the study of Coulomb blockade. Being inert in nature, platinum particles are not prone to oxidation and are expected to remain stable in air. At the same time, the size of the synthesized particles can be adjusted in the range of 1.1 – 3 nm which makes them suitable to observe and tune Coulomb blockade at room-temperature. Being synthesized by chemical routes, they also offer the possibility of facile exchange of ligands in the solution. This permits us to coat the particle surface with various ligands including aryl and alkyl chains of amines, thiols, alcohols, and carboxylic acid. Again, this can be used as a tool to tune Coulomb blockade in the assembly of these particles. In this chapter, we shall present charge transport studies performed on the assemblies of the mentioned platinum nanoparticles coated with different ligands. We shall begin by briefly introducing the synthesis of the particles followed by the characterization methods useful for determining the various physical parameters such as inter-particle separation, dielectric constant of ligands, etc. Finally, we shall present the charge transport studies performed at micro and nano-scale assemblies.

The synthesis of the particles was carried out by Dr. Simon Tricard from our laboratory in the group *Nano-structure and organometallic chemistry*. The synthesis procedure consists of two major steps. In the first step, particles are obtained in their “naked” form, where they are not attached to any externally added aryl/alkyl ligands. Instead, they are coated with the tetrahydrofuran (THF) and CO used during the reaction. In the second step, these naked particles are coated with suitable alkyl/aryl groups to obtain their final form. The procedure of the synthesis is briefly described below.

2.2 Synthesis procedure

Synthesis of the particles was carried out in THF inside a Fischer-Porter bottle. In order to avoid any oxide formation during the synthesis, all the steps were performed under argon atmosphere and only deoxygenated THF was used to avoid any traces of oxygen in the reaction mixture. In the first step of the reaction, a 20 mL solution of $Pt_2(dba)_3$ (dba = dibenzylideneacetone) containing 0.165 mmol of Pt was pressurized in a Fisher-Porter under 1 bar CO at room-temperature under vigorous stirring. This procedure was carried out for 30 minutes during which the color of the solution turned brown from violet. The change in color indicates the formation of Pt nanoparticles. The solution was dried and then washed 3 times with pentane in order to remove residuals of $Pt_2(dba)_3$. The resulting colloid was then re-dissolved in 20 mL THF and left for ripening under agitation at room-temperature. This is the crucial step as the size of the particle is determined by the ripening time i.e. the longer the ripening time, the larger the particle size. The particles obtained right after the synthesis were ~1.1 nm in diameter while those left for 15 minutes of ripening were found to be ~1.7 nm in size. Particle size up to 2 nm could be achieved after four days of ripening. We will generally call the particles obtained at the end of this step “naked” particles, as no externally added ligands is coated on the surface. However, as mentioned previously, particles are not completely naked, and the THF and CO used during the reaction are coordinated with the particles. The above reaction can be summarized by the following reaction equation:

$$Pt_2(dba)_3 \xrightarrow{\text{1 bar CO ; THF ; room-temperature}} Pt_x(CO)_y(THF)_z$$

In the second step, various alkyl/aryl ligands possessing different functional entities were added to the different parts of solution. These ligands included 4-aminothiophenol ($HSPhNH_2$), 4-mercaptophenol (HSPhOH), and 4-mercaptobenzoic acid (HSPhCOOH) as shown in Figure 2.1 (a), (b),and (c) respectively. Besides, a series of linear chain alkyl thiols ranging from heptane thiol ($C_7H_{15}SH$) to dodecane thiol ($C_{12}H_{25}SH$) was also used [see Figure 2.1 (d)]. After addition of these ligands, the ripening of the particles is stopped and the particle size remains stable. For all the ligands, a concentration of 0.2 equivalent of platinum was used. This concentration was found to be suitable for optimally covering the particles’ surface without leaving much residue of the ligands in the solution. More details on the synthesis can be found elsewhere [8].

As we shall discuss in the later sections of this chapter, the motive of choosing these ligands is different for alkyl and aryl thiol ligands. The series of alkyl thiol ligands was chosen to study the effect of inter-particle distances on Coulomb blockade in assemblies of fixed particle size. On the other hand, aryl thiols were used to study the effect of different functional groups present at the para position of these ligands. As we shall see later, relative permittivity of the aryl ligands can change significantly when the functional group at the para position is changed which can significantly affect the Coulomb blockade in the assemblies of the particles.

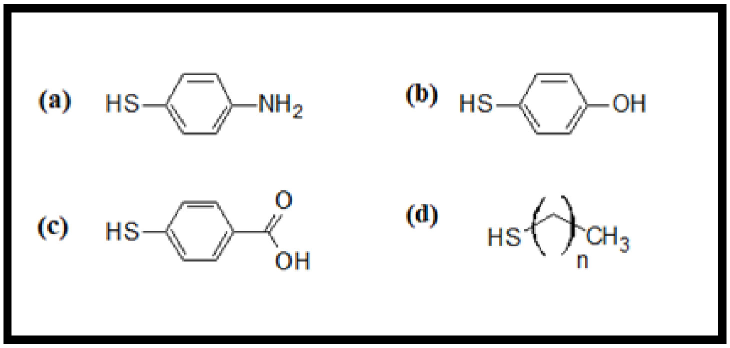

Figure 2.1: Structural formula of different ligands used for coating the surface of platinum nanoparticles. These ligands include (a) 4-aminothiophenol, (b) 4-mercaptophenol, (c) 4-mercaptobenzoic acid, and (d) alkane thiols, where *n* = 6 to 11 in the shown structure.

2.3 Characterization

Particles of different sizes ranging from ~1.1 nm to ~1.7 nm were prepared by using different ripening time. Size of the particles was obtained from TEM images by performing size measurements on ~300 particles. The size dispersion of the particles was found to be ~20% to 30% for all sets of particles. Figure 2.2 (a) and (b) show the TEM images of two sets of particles that were used to study the effect of particle size on Coulomb blockade while Figure 2.2(c) and (d) show their respective size distribution.

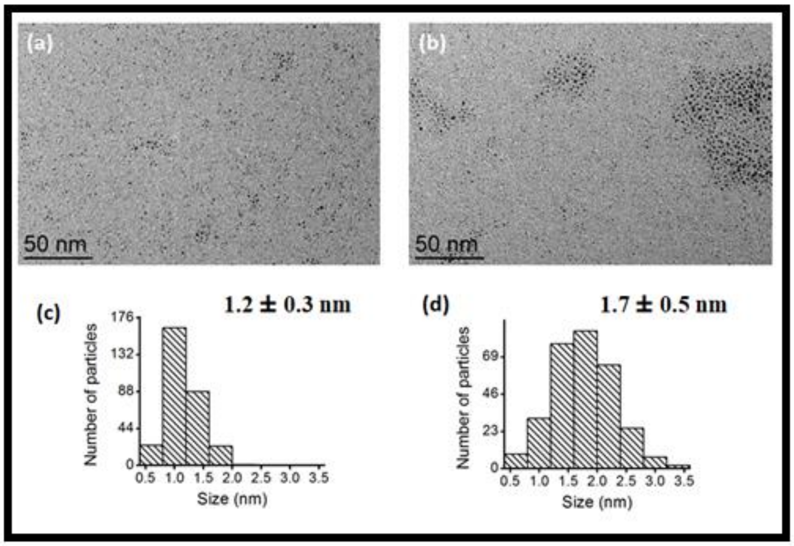

Figure 2.2: TEM images [(a) and (b)] showing well dispersed platinum particles and their respective number size distribution [(c) and (d)].

TEM images were also taken for the assemblies of particles formed after addition of the above mentioned ligands. In case of $HSPhNH_2$ assemblies, platelets were obtained, as shown in Figure 2.3 (a). Small and large rods were obtained in case of HSPhOH and HSPhCOOH respectively as shown in Figure 2.3(b) and (c). Interestingly, larger assemblies formed for the ligand with higher hydrogen bonding strength. The strength of hydrogen bonding follows the following order: amine < hydroxyl< carboxylic acid. Assemblies formed in case of alkyl thiols also showed rod like structure. Figure 2.3 (d) shows the TEM image for the assembly formed with dodecanethiol.

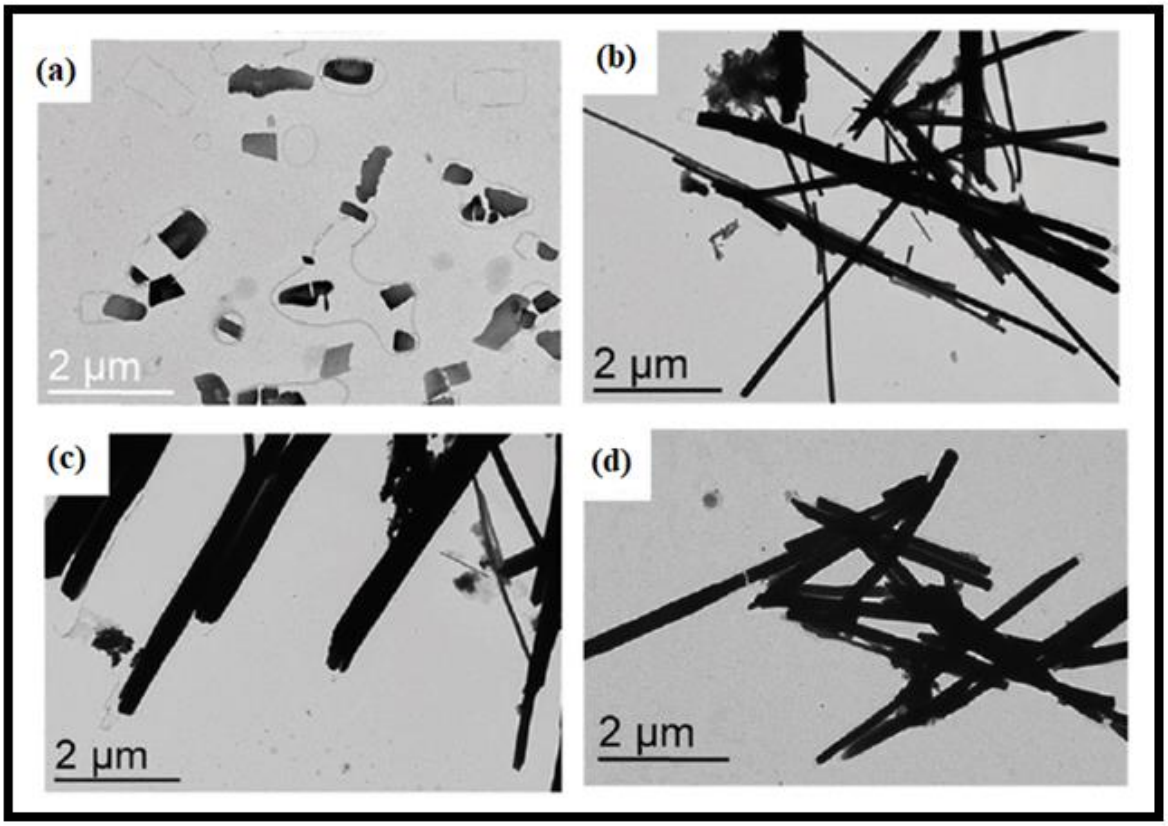

Figure 2.3: TEM images of the assemblies formed by Pt nanoparticles after addition of (a) $HSPhNH_{2,}$ (b) HSPhOH, (c) HSPhCOOH, and (d) alkyl thiol (dodecanethiol).

2.4 Determining of inter-particle separation

(a) For fixed particles size with different alkyl thiols ligands

Varying the length of the ligand molecules can significantly alter the inter-particle separation in an assembly [7, 9]. Generally, in case of linear alkyl chain ligands, increasing the chain length results in increased inter-particle distance. In our case, 6 linear chains of alkyl thiols, ranging from heptanethiol to dodecanethiol, were used to control the separation between the particles of diameter (d) ~1.3 nm. A short-hand notation for the assemblies of these ligands will be used, where they shall be referred as HSCX, where X is the number of carbon in the alkyl chain. For example, HSC7 will correspond to the assembly of particles with heptanethiol.

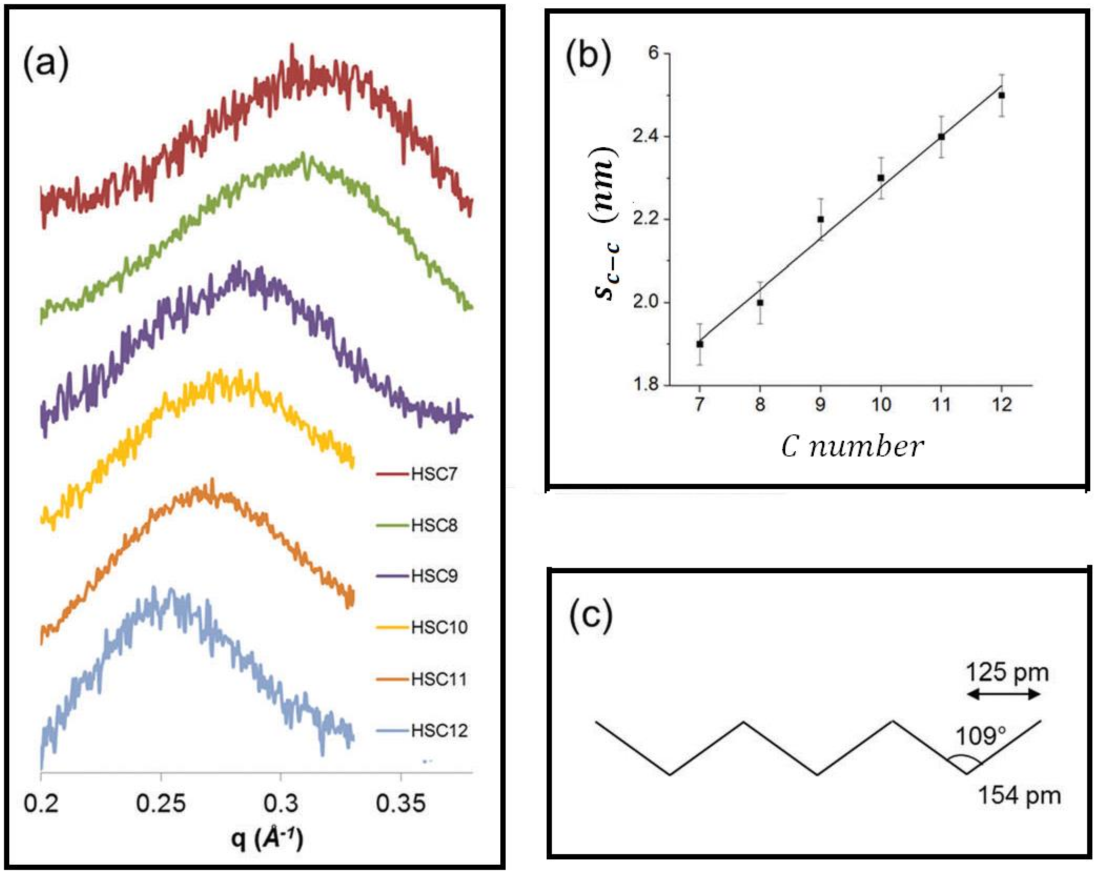

Figure 2.4: (a) SAXs measurements performed over the assemblies of particles of ~1.3 nm size, coated with 6 different alkyl chains ranging from HSC7 to HSC12, (b) variation in centre-to-centre distance (s_{c-c}) as a function of number of carbons in the alkyl chain, and (c) Structural formula of an alkane showing the C - C bond length and its projection over the chain molecule.

Small angle X-ray scattering (SAXs) measurements were performed on assemblies of particles coated with alkyl thiols to obtain the values of inter-particle distance. As evident from Figure 2.4 (a), the position of maximum intensity in the correlation curves shifts towards lower q values with increasing chain length. The centre to centre distance (s_{c-c}) between the particles was estimated by using the formula, $s_{c-c} = 2\pi/q_{max}$. Table A summarizes the values of s_{c-c} obtained in case of different chains of alkyl thiol ligands. These values provide important information regarding the interdigitation of alkyl chains. For example, for the particles coated with HSC7, the value of s_{c-c} is 1.9 nm which indicates an edge to edge separation (s_{e-e}) of 0.6 nm (particle's diameter being 1.3 nm). This value is quite close to the chain length of the 7 carbon alkyl chain which is roughly 0.7 nm [see Figure 2.4(c)]. In case of no interdigitation of ligands, values of s_{e-e} would be approximately two times the length of the ligand. However, lower values are possible due to interdigitation of ligands. In our case, the closely related values of ligand's length and s_{e-e} indicate almost complete interdigitation of the alkyl ligands.

Besides, s_{c-c} increased linearly with increasing carbon number. For each carbon added to the chain, s_{c-c} increased approximately by a length of 123 $\pm$ 8 pm as shown in Figure 2.4 (b). This length corresponds approximately to the projection of C-C bond over the alkyl chain, as shown in Figure 2.4 (c).

Ligands	d ($\pm$ 0.3 nm)	s_{c-c} ($\pm$ 0.05 nm)	s_{e-e} ($\pm$ 0.05 nm)
HSC7	1.3	1.9	0.6
HSC8	1.3	2.0	0.7
HSC9	1.3	2.2	0.9
HSC10	1.3	2.3	1.0
HSC11	1.3	2.4	1.1
HSC12	1.3	2.5	1.2

Table A: Value of center-to-center distance (s_{c-c}) and edge-to-edge distance(s_{e-e}) between the Pt particles (1.3 nm) coated with different chains of alkyl thiol ligands.

(b) For fixed ligands with different particle sizes

Particle size is one of the major factor that determines the extent of Coulomb blockade in an assembly. For a fixed ligand, the charging energy of the particle increases with decrease in its size, and consequently the extent of Coulomb blockade increases. In order to study the size effect, particles of size 1.2 $\pm$ 0.3 nm and 1.7 $\pm$ 0.5 nm were coated with ligands HSPhCOOH, HSPhOH, and $HSPhNH_2$.

SAXs measurements, as shown in Figure 2.5, were performed over the assemblies of these particles in order to obtain the s_{c-c} as described in previous section. For a fixed particle size, the s_{c-c} and s_{e-e} values were found to be higher in case of HSPhCOOH and lower in case of HSPhOH as summarized in Table B. Besides, the observed value of s_{e-e} for a given ligand is found to be slightly higher for smaller particles compared to larger ones.

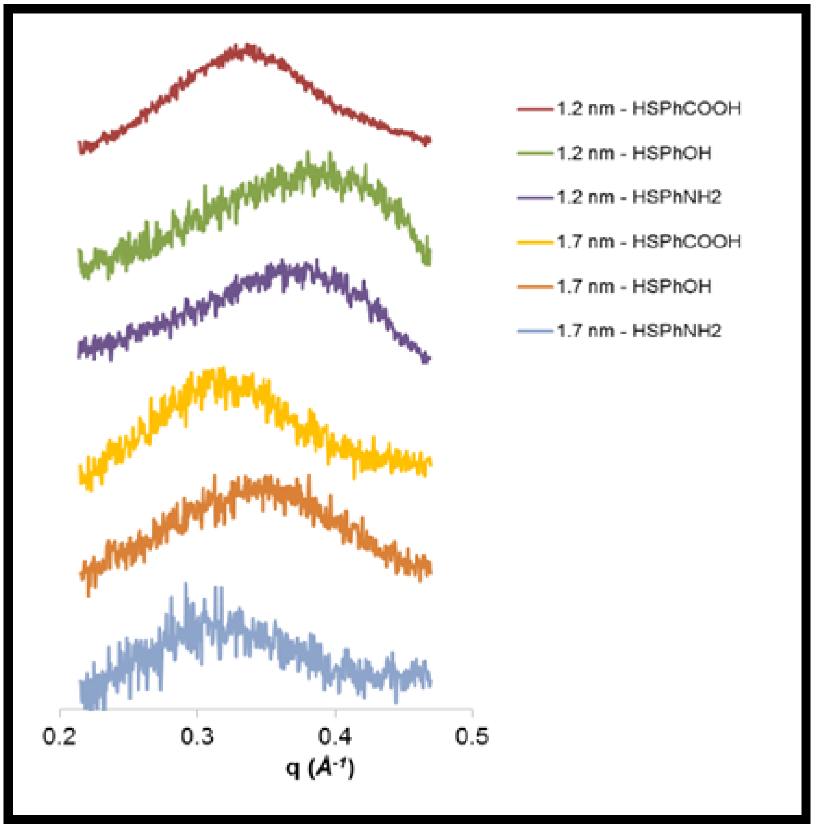

Figure 2.5 : SAXs measurements performed over the assemblies of particles of sizes 1.2 ± 0.3 nm and 1.7 ± 0.5 nm coated with different aryl ligands.

Ligands	d (nm)	s_{c-c} (± 0.05 nm)	s_{e-e} (± 0.05 nm)
HSPhCOOH	1.7 ± 0.5	2.1	0.4
HSPhOH	1.7 ± 0.5	1.9	0.2
$HSPhNH_2$	1.7 ± 0.5	2.1	0.4
HSPhCOOH	1.2 ± 0.3	1.9	0.7
HSPhOH	1.2 ± 0.3	1.6	0.4
$HSPhNH_2$	1.2 ± 0.3	1.7	0.5

Table B: Value of center-to-center distance (s_{c-c}) and edge-to-edge distance (s_{e-e}) between the Pt particles (of sizes 1.2 nm and 1.7 nm) coated with aryl thiol ligands with different functional groups at para position.

2.5 Determining dielectric constant

(a) Aryl ligands

Dielectric constant is relatively less utilized for tuning the Coulomb blockade; however its effect on charging energy cannot be neglected. The values of relative permittivity (ε_r) of different ligands that we used in the experiments were provided by Dr. Phillipe Demont from CIRIMAT, Toulouse by performing dielectric spectroscopy. These values are summarized in Table C. The values of ε_r vary significantly in the case of aryl ligands due to the different functional group present at the para position, and was found to be highest for $HSPhNH_2$ and lowest for HSPhCOOH. High values of ε_r can increase the mutual capacitance between the particles, which may lower the charging energy of a particle in an assembly provided that the other physical parameters such as size, inter-particle distance, etc. remain fixed.

Ligands	ε_r
HSPhCOOH	2.7
HSPhOH	5.2
$HSPhNH_2$	7.1

Table C: Values of relative permittivity obtained by dielectric spectroscopy for different aryl ligands.

(b) Alkyl ligands

In case of alkyl thiols, relative permittivity could not be determined by dielectric spectroscopy due to their liquid state at room-temperature. However, we could estimate it from two other approaches. The first approach included estimation of ε_r from the refractive index of the ligands using the formula $\varepsilon_r = n^2$, where n is the refractive index of the ligand. The values of n (provided by the chemical providers) and calculated ε_r values are summarized in Table D. In the second approach, theoretical values of polarizability(α_{CM}) were used to obtain ε_r values using Clausius-Mossotti relation given below:

$$\alpha_{CM} = \frac{\varepsilon_r - 1}{\varepsilon_r - 2} \frac{3\,M}{4\pi D N_A} \qquad 2(a)$$

where M is the molar mass of the substance, D being the density, and N_A is the Avagadro's number. Theoretical values of polarizability were calculated by Pr. Romuald Poteau of LPCNO using DFT. The advantage of theoretical calculations is the possibility to dissociate the global polarizability (*i.e.* averaged in three dimensions) from the axial polarizability (*i.e.* the component along the axis of the molecules in a *trans* conformation). The axial and the global values of α_{CM} are summarized in Table E. A good agreement was observed between the $\varepsilon_r$values obtained from refractive index and those obtained by putting global polarizability values in Clausius-Mossotti equation. This indicates that the dielectric constant obtained from the refractive index corresponds to the global value of dielectric of the ligand. On the other hand, the dielectric constant obtained by putting axial polarizability in Clausius-Mossotti equation showed higher values than the global dielectric constant. These values of dielectric constant obtained from global and axial polarizability of the ligands are summarized in Table E.

Ligands	*M* (g mol^{-1})	*D* (g cm^{-3})	*n*	ε_r
HSC7	132	0.844	1.451	2.11
HSC8	146	0.843	1.452	2.11
HSC9	160	0.842	1.455	2.12
HSC10	174	0.841	1.458	2.13
HSC11	188	0.841	1.459	2.13
HSC12	202	0.845	1.459	2.13

Table D: Values of molar mass (*M*), density (*D*), and refractive index (*n*) of different alkyl chain ligands provided by the chemical providers. ε_r is calculated using the $\varepsilon_r = n^2$.

Ligands	α_{global} (bohr^3)	α_{axial} (bohr^3)	$\varepsilon_{r-\,global}$	$\varepsilon_{r-\,axial}$
HSC7	113	146	2.10	2.60
HSC8	126	164	2.11	2.63
HSC9	139	182	2.12	2.67
HSC10	152	200	2.13	2.69
HSC11	165	219	2.14	2.72
HSC12	177	237	2.14	2.75

Table E: Values of global and axial polarizability obtained from DFT calculations and corresponding dielectric constant obtained from Clausius-Mossotti equation.

2.5 Theoretical estimation of charging energy

The main ingredients required for the estimation of charging energy are (a) particles size, (b) inter-particle separation, and (c) dielectric constant of the ligands. From the characterization of the assemblies, we have all the ingredients permitting us to perform a theoretical estimation of charging energy using the formula $E_c = e^2/2C_\Sigma$, where C_Σ is the capacitance of a particle surrounded by *N* neighbors and is defined as [10]:

$$C_\Sigma = 2N\pi\varepsilon_o\varepsilon_r r\ln(1 + 2r/s_{e-e}) \qquad 2(b).$$

Considering the assemblies to be 3D with hexagonal arrangement of particles, we take the value of *N* to be 12. With spectroscopically determined values of ε_r, charging energy for assemblies with aryl ligands could be estimated. These values are summarized in Table F.

Ligands	d	E_c estimated (meV)
HSPhCOOH	1.7 ± 0.5	32 ± 3
HSPhCOOH	1.2 + 0.3	74 ± 8
HSPhOH	1.7 ± 0.5	12 ± 0.8
HSPhOH	1.2 ± 0.3	27 ±3
$HSPhNH_2$	1.7 ± 0.5	12 ±0.8
$HSPhNH_2$	1.2 ± 0.3	23 ±3

Table F: Estimated values of charging energy of Pt particles (1.2 nm and 1.7 nm) with different aryl ligands.

As one would expect, for a given ligand, the value of charging energy is higher for smaller particle size. For example, charging energy for the assemblies of Pt-HSPhCOOH (*d*= 1.2 nm) is much higher than that of Pt-HSPhCOOH (*d*= 1.7 nm). On the other hand, for a fixed particle size, the value of charging energy increases as the dielectric constant of the ligand decreases. For example, for particle size 1.2 nm, the value of estimated charging energy is higher with HSPhCOOH (ε_r = 2.7), and the lower for $HSPHNH_2$ (ε_r = 7.1).

Similarly, estimation of charging energy could be made for assemblies of Pt particles (*d* =1.3 nm) with alkyl thiol ligands, and are summarized in Table G. For comparison purposes, we used the dielectric constant obtained from the global polarizability ($\varepsilon_{r-\,global}$) as well as the axial polarizability($\varepsilon_{r-\,global}$). In both the cases, charging energy increases with increase in carbon numbers in the alkyl chain. However, higher values of charging energy are obtained when the dielectric constant corresponding to the global polarizability is used.

	$\varepsilon_{r-\,global}$	$\varepsilon_{r-\,axial}$	$E_{C-\,global}$ (meV)	$E_{c-\,axial}$ (meV)
Pt-HSC7	2.10	2.60	76 ± 8	61 ± 6
Pt-HSC8	2.11	2.63	83 ± 9	67 ± 7
Pt-HSC9	2.12	2.67	97 ± 10	77 ± 7
Pt-HSC10	2.13	2.69	103 ± 12	82 ± 9
Pt-HSC11	2.14	2.72	110 ± 12	87 ± 9
Pt-HSC12	2.14	2.75	117 ± 12	91 ± 9

Table G: Values of global and axial dielectric constant for alkyl thiols and their corresponding charging energies for Pt particles (*d*~1.3 nm).

2.6 Sample elaboration for charge transport measurements

Charge transport measurements were performed on the assemblies of particles at nano and micro scale. For nanoscale assemblies, conductive AFM measurements were performed using a AIST-NT smart SPM-1000 microscope, equipped with a conductive AFM unit. The samples were prepared by depositing a drop of particles' solution on a silicon wafer covered with ~50 nm gold layer and ~5 nm thick anchoring chromium layer. Measurements were performed using conductive Si tips covered with platinum. *I-V* curves were normalized at 2 *V* for aryl series and at 5 *V* for alkyl series. The characteristics were then averaged out on 50 curves. The error bars are shown on the *I-V* curves, and are 95% confidence interval. Figure 2.6(a) shows the schematic diagram of the AFM tip and flow of current in the assembly. Figure 2.6(b) shows image of Pt-HSPhCOOH rods taken from AFM.

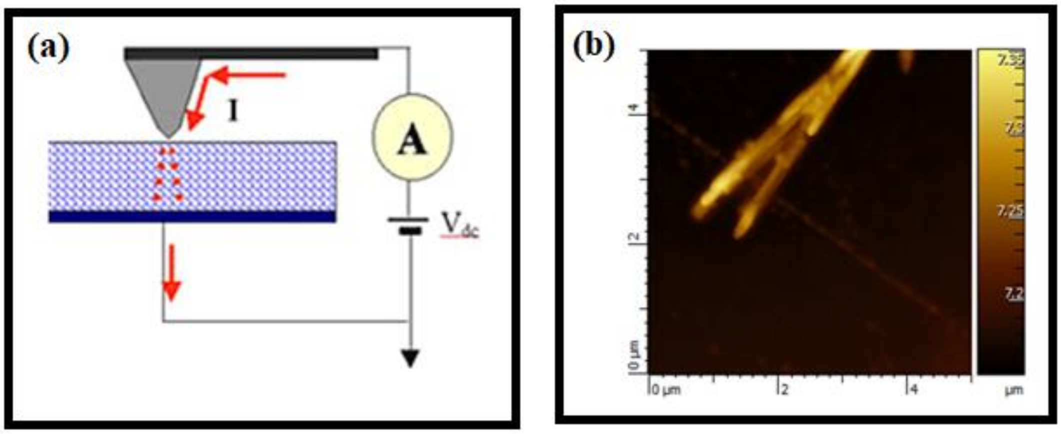

Figure 2.6: (a) Schematic diagram of an AFM tip and assembly showing the flow of current between them and (b) an AFM image of the Pt-HSPhCOOH rods.

For microscale assemblies, interdigitated gold electrodes were used which were designed by photolithography on Si/SiO_2 surface. A single electrode consisted of 20 interdigitated fingers which were 30 nm in height, 200 µm in length, and separated by a 5 µm gap. Figure 2.7 (a) and (b) show the SEM image of an ensemble of 8 interdigitated electrodes, and a zoomed view of a single electrode respectively. To trap the particles between the electrodes, dielectrophoresis was performed at 7.5 V, 10 kHz for 20 seconds. The residual of the drop on the surface was soaked by a filter paper in order to avoid the deposition of the ligands contained in the drop. Images from scanning electron microscope (SEM) shows partially filled gaps, indicating the dielectrophoresis conditions are not fully optimized [see Figure 2.8 (a),(b) and (c)]. Dielectrophoresis performed at 2.5 *V*, 5 *V*, and 10 *V* at frequencies 5 kHz and 10 kHz showed similar partially filled gaps. Further investigation is needed to optimize the dielectrophoresis for these particles. Nevertheless, the fact that a conducting path of nanoparticles was created during the dielectrophoresis process permitted us to perform charge transport measurements on these assemblies.

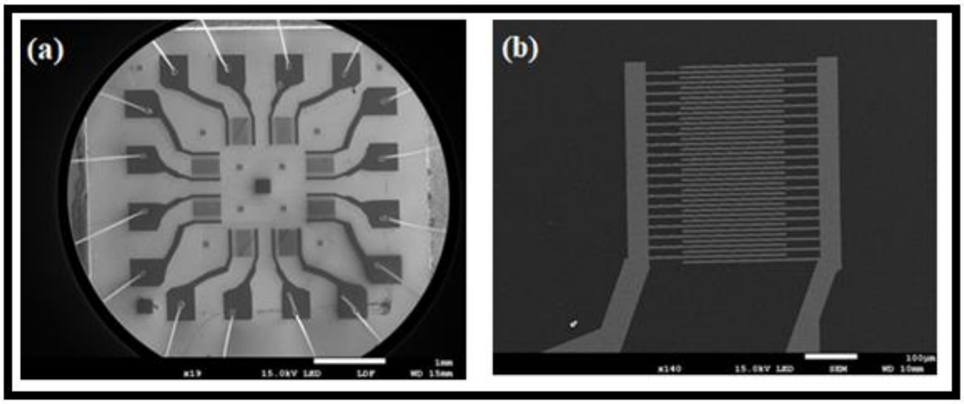

Figure 2.7: SEM images of interdigitated electrodes showing (a) ensemble of 8 electrodes on Si/SO_2 and (b) zoomed view of single electrode.

The resistance of the electrodes measured after performing dielectrophoresis was found to vary from electrode to electrode. Electrodes with more particles deposited between them were found to be more conducting than those with low number of particles, Figure 2.8 (a) shows SEM image of an electrode after dielectrophoresis of particles with HSC7. This electrode had more number of particles compared to the electrodes shown in Figure 2.8 (b) and (c). The room-temperature resistance for these electrodes is shown in Figure 2.8 (d). As evident from the *I*-*V* curves, electrodes with more particles show larger current values.

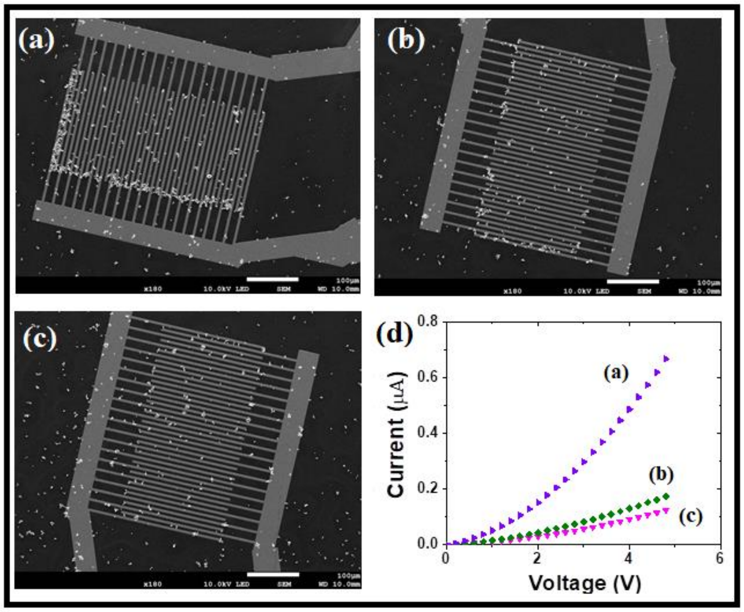

Figure 2.8: SEM images of interdigitated electrodes showing (a) more number of particles, (b) and (c) less number of particles deposited on different electrodes after dielectrophoresis. (c) *I*-*V* curves of the three electrodes showing higher conductance for electrode with large number of particles.

2.7 Charge transport measurments

(a) Effect of inter-particle separation

In order to study the effect of inter-particle separation, we first studied the charge transport in assemblies of Pt particles coated with HSC7 and HSC12 which are the smallest and the longest alkyl chains used in our experiments. This would allow us to observe the both end of spectrum of charging energy in this case i.e. highest and lowest charging energy due to the longest and shortest chain length. Besides, charge transport in assemblies of naked particles was also studied for studying the difference in charging energy of particles before and after adding external ligands i.e. HSC7 and HSC12.

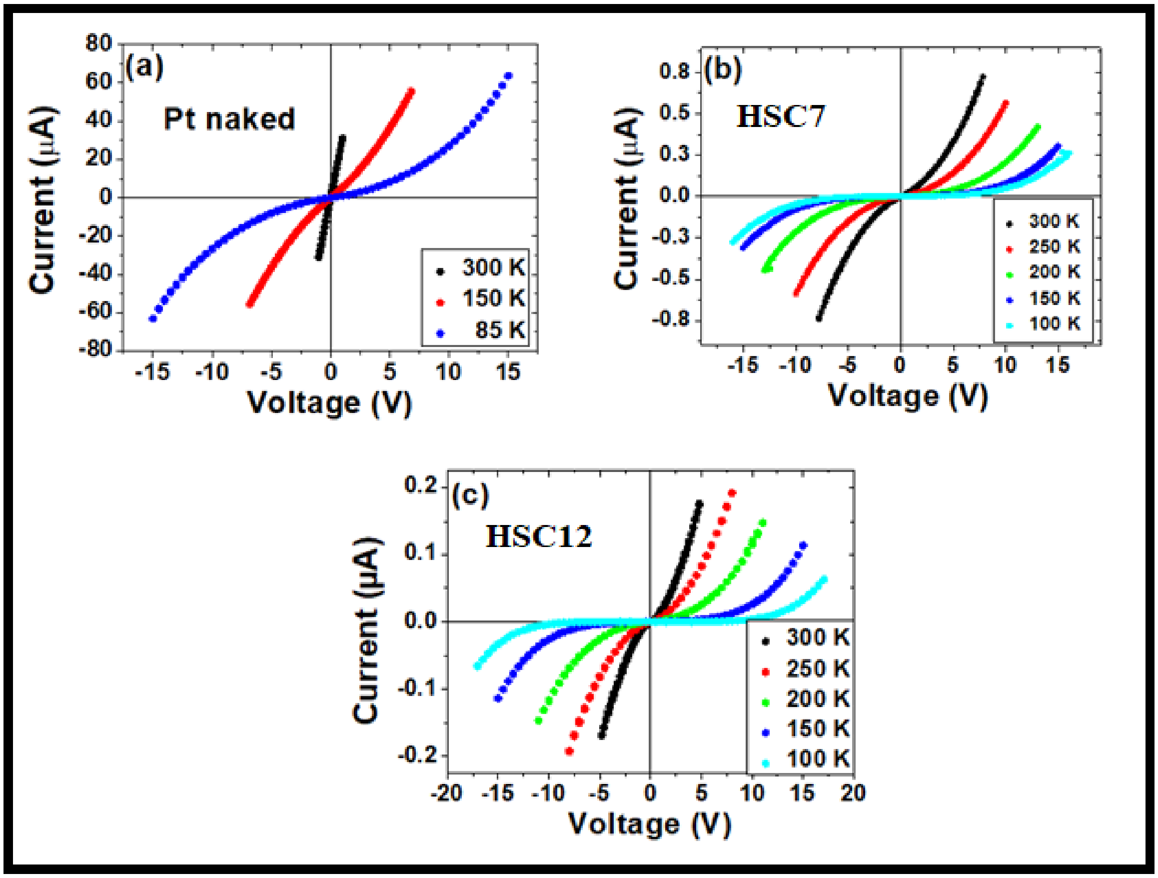

Figure 2.9: *I-V* curves at different temperatures for (a) Pt naked, (b) HSC7, and (c) HSC12 assemblies showing Coulomb blockade behavior.

For assemblies of naked particles, four electrodes studied at room-temperature had a resistance in the range of 2-40 kΩ. Such a variation in the resistance may arise due to the different number of particles deposited between the interdigitated gaps. *I-V* curves measured at room-temperature showed linearity in all cases without any sign of Coulomb blockade. At low temperatures, non-linearity and Coulomb gap was observed in all the four electrodes which confirmed that particles assemblies do not display a fully metallic behavior, despite the low value of the resistance measured at room temperature. Figure 2.9(a) shows the *I-V* curves of a representative assembly of Pt naked particles.

For Pt assemblies coated with HSC7, room-temperature resistance was found to be in the range of 2-15 MΩ for the five measured electrodes which is higher than the resistance of naked particles. Moreover, *I-V* curves were non-linear at room-temperature for all the electrodes. In case of assemblies with HSC12, even higher room-temperature resistance was observed which lied in the range of 35 MΩ-1.7 GΩ for the five measured electrodes. Figure 2.9 (b) and (c) show the *I-V* curves at room-temperature for a representative assembly of HSC7 and HSC12.

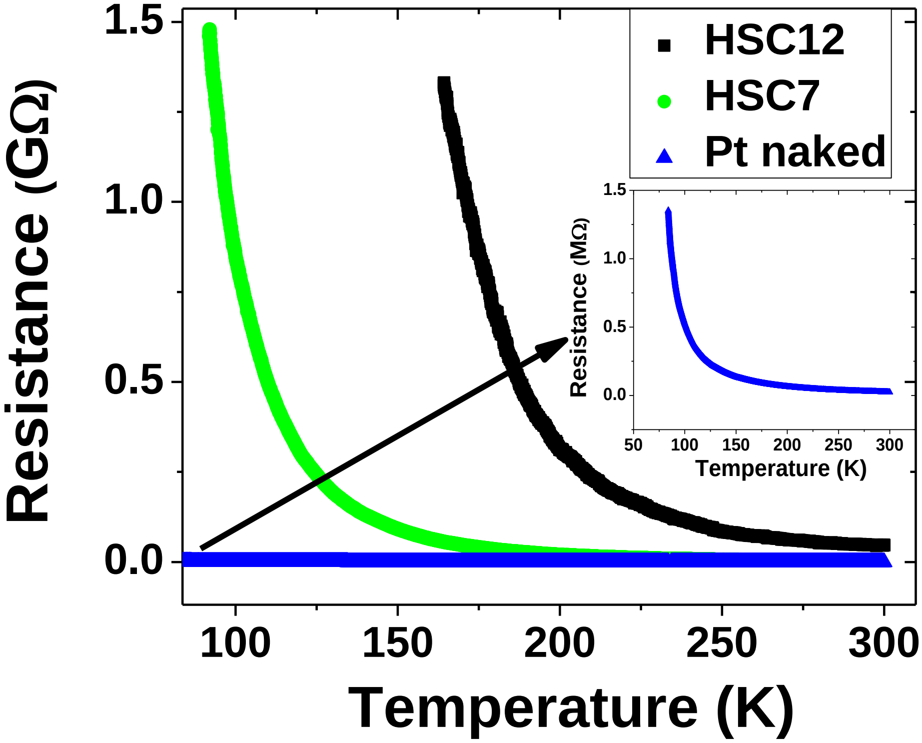

Figure 2.10: Variation of resistance as a function of temperature for assembly of Pt particles coated with HSC12 (at V = 2 V), HSC7 (V = 1V), and naked (V = 1V). Inset shows the enlarged view of resistance temperature curve for assembly of Pt- naked particles.

In order to obtain E_c values, variation in the resistance as a function of temperature was studied for these assemblies. With decrease in temperature, a strong increase in resistance was observed in all cases indicating the presence of Coulomb blockade. Figure 2.10 shows the resistance-temperature curve for the representative assembly from each case. The resistance of assembly with HSC12 increased much more rapidly than the resistance of HSC7 and naked particles' assemblies. This indicates that charging energy starts dominating the thermal energy at much higher temperatures for assemblies of HSC12 compared to HSC7 and Pt naked.

E_c can be extracted from the slope of a lnR versus 1/T as shown for the representative assemblies in Figure 2.11. The values of E_c for these assemblies were found to be 108 meV, 91 meV and 46 meV for the assembly of HSC12, HSC7, and naked particles respectively. However, these values of charging energy in each case varied slightly from electrode to electrode. Figure 2.12 shows the E_c values from all studied electrodes of these assemblies. Despite of the variation in E_c, a general trend can still be observed. The average value of E_c (measured on four or more electrodes) was found to be maximum for assemblies of HSC12 (~ 114 meV) followed by assemblies of HSC7 (~ 87 meV) and then Pt "naked" particles (~ 36 meV). This trend is expected as the longer chain length in case of HSC12 would result in higher inter-particle distance, thus, would have lower value of inter-particle capacitance (as per equation 2(b)) and higher charging energy.

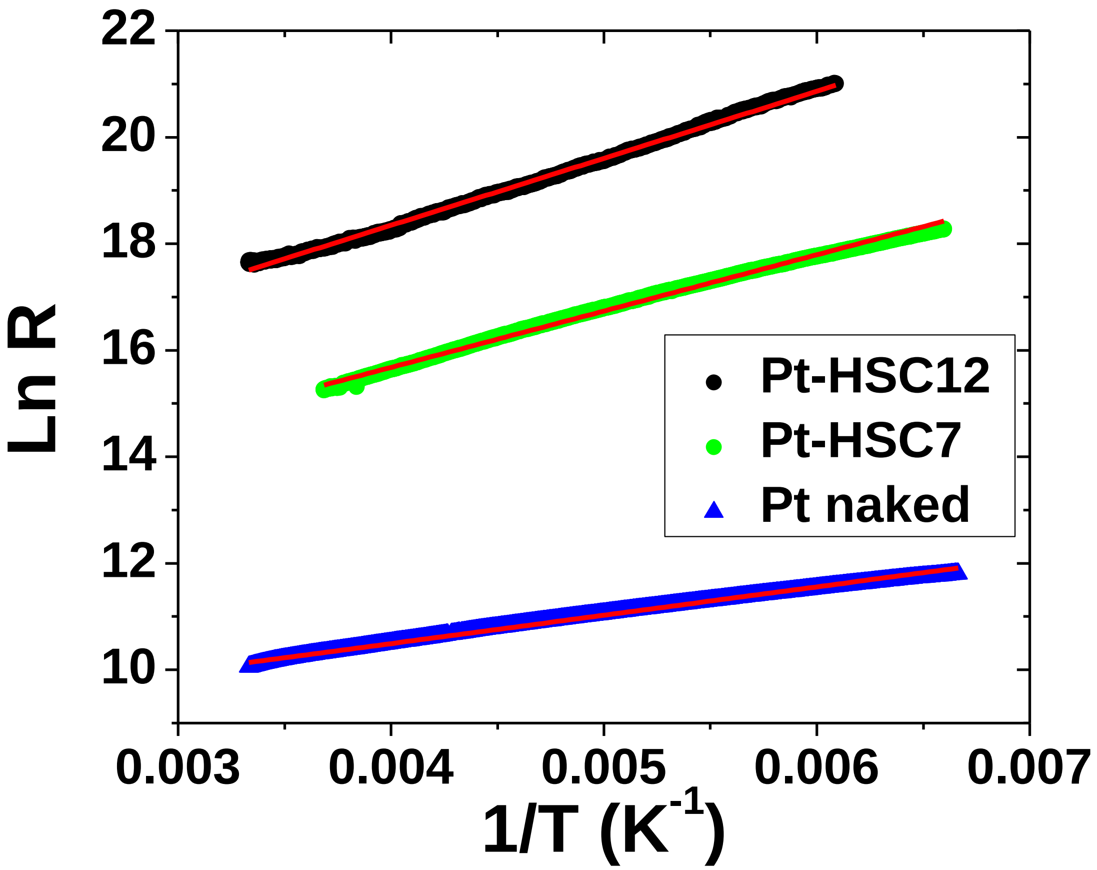

Figure 2.11: A plot of ln R versus 1/T showing linear trend for the assemblies of platinum particles with C12SH, C7SH, and in naked form. The slope of the curve is a measure of charging energy which is highest in case of Pt-C12SH and lowest in case of Pt naked.

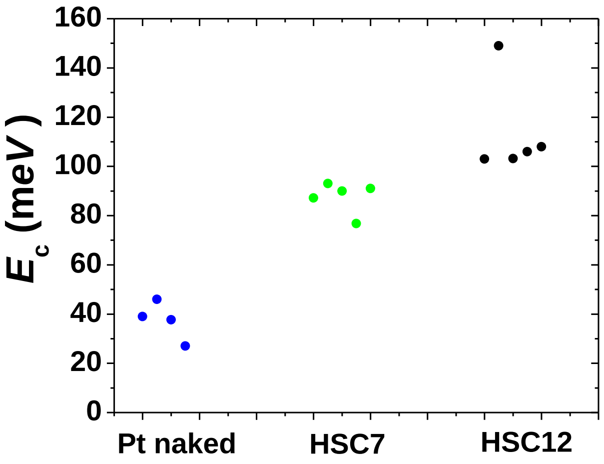

Figure 2.12: Value of charging energy obtained for the HSC12, HSC7, and Pr naked assemblies. For a given type of assembly, charging energy can show small dispersion in value from electrode to electrode.

Besides, the experimental value of charging energy was found close to the theoretical values calculated in section 2.5, using equation 2(b). Table G summarizes the experimental and theoretical values of charging energy obtained from axial and global permittivity. The experimental values were found to be higher than the theoretically estimated values by both approaches i.e. using axial and global permittivity. However, estimated values of charging energy using global dielectric constant were relatively close to the experimental value.

	E_c experimental (m*eV*)	E_c estimated- axial (meV)	E_c estimated- global (meV)
Pt-HSC7	87± 6	61 ± 6	76 ± 8
Pt-HSC12	114±17	91 ± 9	117 ± 12

Table G: Experimental and calculated values of charging energy for assembly of Pt-HSC7 and Pt-HSC12

On the other hand, lowest value of charging energy in case of naked particles can be attributed to two factors. First could be the smaller ligand length. Although the value of inter-particle distance could not be determined for naked particles due to the absence of correlation peak in SAXs measurements, the ligands coated on "naked" particles (CO and THF) are expected to be relatively smaller in size compared to HSC7 or HSC12. It may be the reason of their relatively low charging energy. The second possibility could be the high dielectric constant of the ligands. The low charging energy could also be the combined effect of both the mentioned factors. In any case, the lower charging energy for naked particles compared to HSC7 and HSC12 assemblies indicate the successful functionalization of particle surface by externally added ligands.

The difference between the charging energy of the longest and the shortest alkyl chain assembly was found to be ~27 meV. Thus we expect an average increase of 5 meV per carbon added to the chain. To detect such a small change, a statistics over large number of measurements should be performed. For this, we used conductive AFM which provides the possibility of measuring a large number of I-V curves at room-temperature, and thus to compensate the variability in the transport properties of the assemblies by averaging. Using conductive AFM technique, small nano-scale assemblies could be measured, which lied between the tip of the AFM and the Si surface.

As the conductive AFM used was limited to only room-temperature measurements, we tried to quantify the extent of Coulomb blockade from the I-V curves. Figure 2.13 shows the normalized I-V curve (at $V = 5V$) for the assemblies of alkyl chains. The characteristic curves are statistically averaged over 50 normalized measurements. To quantify the extent of Coulomb blockade, first possibility would be to use the Middleton-Wingreen model (as described in chapter 1.1). I-V curves were fitted using it to obtain the values of the threshold voltage V_t and ξ, and are shown in Table H. There are two reasons for which the Middleton-Wingreen is in fact not suitable for this study. First, negligibally small values of V_t (of the order of 10^{-4} V) were obtained, which restricted us from a reliable comparison of these values to find out the extent of Coulomb blockade. Second, Middleton-Wingreen's model should in principle only be used at low temperature. Therefore, in our system, V_t could not be used as a reliable parameter to relate with Coulomb blocakde.

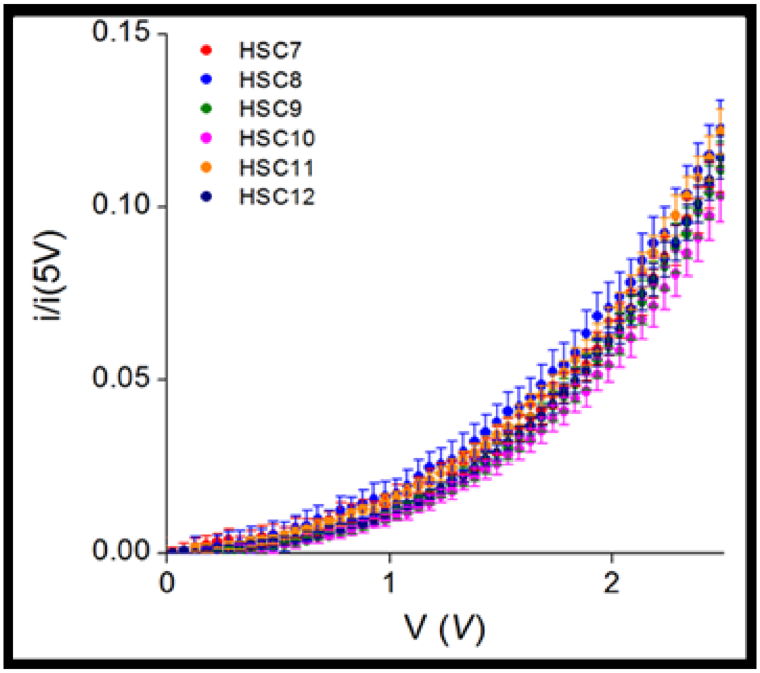

Figure 2.13: Normalized I-V curves measured at room-temperature using AFM for Pt assemblies coated with different alkyl chains.

Ligands	V_t (V) from fit using Middleton-Wingreen equation $\{I \sim (V - V_t)^{\xi}\}$	ξ from fit using Middleton-Wingreen equation $\{I \sim (V - V_t)^{\xi}\}$	ξ from fit using equation $\{I \sim V^{\xi}\}$
HSC7	4.8e-6	3.06 ± 0.1	3.11± 0.07
HSC8	7.1e-4	3.21 ± 0.07	3.29± 0.06
HSC9	1.1e-5	3.23 ± 0.09	3.29± 0.06
HSC10	5.3e-4	3.42 ± 0.06	3.44± 0.06
HSC11	9.3e-4	3.40 ± 0.05	3.40± 0.08
HSC12	8.3 e-4	3.36 ± 0.07	3.43± 0.05

Table H: Values of threshold voltage (V_t) and scaling exponent (ξ) obtained from Middleton-Wingreen fit on the I-V curves measured for Pt assemblies coated with different alkyl thiols. ξ values obtained by fitting $I \sim V^{\xi}$ are also shown.

As a consequence, to compare Coulomb blockade in our assemblies, we chose to rely on a single parameter: the extent of the non-linearity of the curve. The I-V curves were thus fitted by a simple power law: $I \sim V^{\xi}$. These values are summarized in Table H, and do not differ significantly from the values obtained for ξ using the Middleton-Wingreen's equation.

We observed ξ values lying between 3 to 3.5 for all the assemblies. The minimum ξ value was observed for HSC7 and increased for longer chains, so the expected trend is globally respected. However the uncertainty on ξ values is such that, between two consecutive alkyl chains differing by one carbon, the trend is not always respected. We shall discuss relate with these values in later section.

(b) Effect of size and dielectric constant

One effective way of controlling Coulomb blockade is by varying the particle size while keeping fixed the inter-particle distance. In an assembly, the inter-particle distance is mainly governed by the length of the ligands, so keeping the same ligand permit us to fix the inter-particle separation. In order to study the effect of size, we chose particles of sizes 1.2 nm and 1.7 nm, and compared their properties with same ligands. Three ligands were used for each set of particles which included HSPhCOOH, HSPhOH, and $HSPhNH_2$.

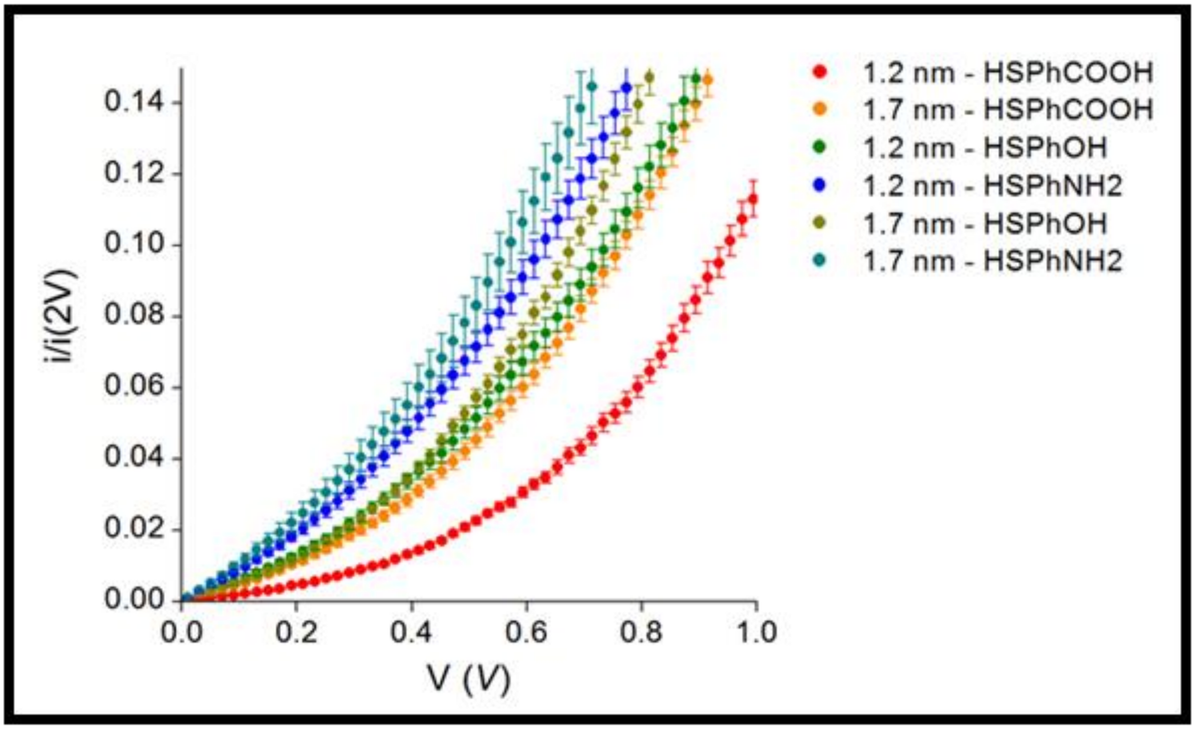

Figure 2.14: *I-V* curves measured for two sets of particle size with different aryl ligands at room-temperature using conductive AFM.

Conductive AFM measurements were performed at room-temperature for the two sets of particles with different ligands. For a given ligand, the extent of Coulomb blockade or non-linearity observed in *I-V* curves varied significantly for the two particles sizes. In case of smaller particles, higher non-linearity was observed. For example, in assemblies of particles with HSPhCOOH, particles of size 1.2 nm showed higher non-linearity compared to the assemblies of HSPhCOOH with particles size 1.7 nm as evident from the *I-V* curves [see Figure 2.14].

Effect of dielectric constant could also be studied from the *I-V* curves shown in Figure 2.14. As the dielectric constant of the material increased, the non-linearity in the *I-V* curve decreased. For example, for 1.7 nm particles, assemblies with $HSPhNH_2$ show lower extent of non-linearity compared to the assemblies with HSPhCOOH. In both the cases, same inter-particle distance was observed (~0.4 nm) using SAXs measurements as summarized in Table B. Since, the particle size is also the same in both cases, the only factor that might have caused this difference is the dielectric constant of the ligands. In case of $HSPhNH_{2,}$ spectroscopically determined dielectric constant was much higher (7.1) than that of HSPhCOOH (2.7). The lower dielectric constant in case of HSPhCOOH explains the higher non-linearity of its assembly as the mutual capacitance between the particles would be lower in this case which should result in higher non-linearity..

We performed the similar analysis of threshold voltage and scaling exponent as in case of alkyl ligands. Again, negligible values of threshold voltages were obtained. Thus, we extracted the values of scaling exponent in these assemblies using a simple power law. ξ values obtained for assemblies with aryl ligands are summarized in Table I.

Ligands	Particle size (nm)	ξ $\underline{+}$ 0.1 from fit using Middleton-Wingreen equation $\{I \sim (V - V_t)^{\xi}\}$	ξ $\underline{+}$ 0.1 from fit using equation $\{I \sim V^{\xi}\}$
HSPhOH	1.7	1.97	2.26
HSPhOH	1.2	2.66	2.66
HSPhCOOH	1.7	2.74	2.74
HSPhCOOH	1.2	3.38	3.40
HSPhNH$_2$	1.7	2.05	2.23
HSPHNH$_2$	1.2	2.39	2.46

Table I: Values of scaling exponent ξ obtained from Middleton-Wingreen'sequation and from a power law for assemblies of two sets of particles with different aryl ligands.

Again, the value of ξ obtained from the two equations did not vary significantly. For all the assemblies with aryl ligands, ξ values lied in the range of 2 to 2.5. Interestingly, we observed a correlation in ξ values with the estimated charging energy of the assemblies which were calculated using equation 2(b). For the assemblies with higher estimated charging energy, a higher ξ value was observed.

We plotted the ξ values as a function of estimated charging energy for both alkyl and aryl ligands. In case of alkyl ligands, charging energy was estimated using global and axial value of dielectric constant. Figure 2.15 (a) shows the trend of ξ with charging energy. In this figure, the charging energy for alkyl thiol assemblies are calculated by using axial values of dielectric constant. Figure 2.15 (b) also shows the trend of ξ with charging energy where the charging energy of alkyl thiol corresponds to their global dielectric constant.

There seems to be some correlation between ξ and charging energy which is observed in both alkyl and aryl assemblies. However, within the alkyl series, some data deviation might be present between two consecutive members. Value of ξ has been shown to depend on the dimensionality of the assemblies [11]. One simulation study has even shown temperature dependency of ξ in 2D dense arrays [12]. However, to our knowledge, no trend has been ever reported between ξ and charging energy. Further experimental studies need to be performed to observe such a trend in other systems. Beside, theoretical investigation would also be needed to find a possible explanation of such a trend.

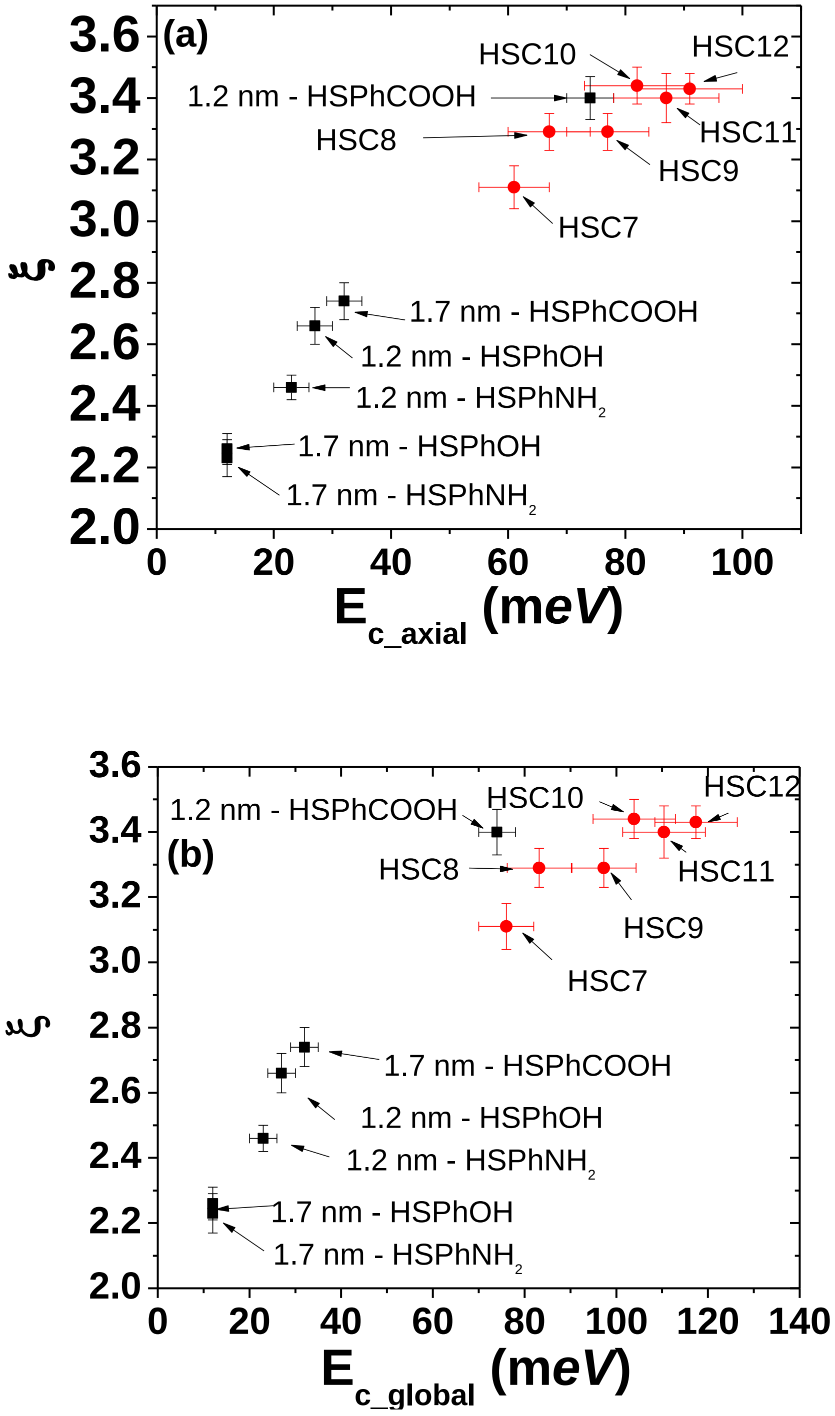

Figure 2.15: Values of ξ for assemblies of particles with different alkyl and aryl ligands showing correlation with charging energy. Values of charging energy are calculated using (a) axial permittivity and (b) global permittivity for alkyl thiols.

2.8 Conclusion

In conclusion, we have measured charge transport in assemblies of Pt particles of sizes in the range of 1.1 nm to 1.7 nm. We could successfully determine the inter-particle separation by using SAXs measurement which showed an increasing distance between the particles with increase in chain length of the alkyl ligands. DFT calculations and spectroscopy shed the light on the dielectric constants of both aryl and alkyl ligands. We could observe the Coulomb blockade at room-temperature due to small size of the particles. Our attempts to tune the charging energy by increasing the ligand's length by one carbon were limited by two factors which are; (a) small difference of charging energy between the two consecutive members of alkyl chain and (b) error in measurements arising due to several factors. Nevertheless, we could successfully determine the charging energy by studying the variation in resistance as a function of temperature in case of the smallest and the largest chain length used in the experiment i.e. HSC7 and HSC12 respectively. Using conductive AFM technique, we could observe the effect of dielectric constant and particle size on non-linearity of *I*-*V* curves. Scaling exponent obtained for different assemblies showed correlation with estimated charging energy. This reflects some effect of charging energy on scaling exponent. However, the reason of such behavior remains unexplained. Theoretical works would be required for establishing the relation between charging energy and scaling exponent. Most studies have quantified Coulomb blockade in terms of charging energy, which often requires low temperature measurements. If a relation between scaling exponent and charging energy is established, it could be used as another tool for quantifying Coulomb blockade at room-temperature.

References: Chapter 2. Tuning of Coulomb blockade in assemblies of nanoparticles

[1] J. Kane, M. Inan, and R. F. Saraf, "Self-Assembled Nanoparticle Necklaces Network Showing Single-Electron Switching at Room Temperature and Biogating Current by Living Microorganisms," *ACS Nano,* vol. 4, no. 1, pp. 317-323, 2010/01/26 2010.

[2] V. Maheshwari, J. Kane, and R. F. Saraf, "Self-Assembly of a Micrometers-Long One-Dimensional Network of Cemented Au Nanoparticles," *Advanced Materials,* vol. 20, no. 2, pp. 284-287, 2008.

[3] A. J. Quinn *et al.*, "Manipulating the Charging Energy of Nanocrystal Arrays," *Small,* vol. 1, no. 6, pp. 613-618, 2005.

[4] J. Dugay *et al.*, "Room-Temperature Tunnel Magnetoresistance in Self-Assembled Chemically Synthesized Metallic Iron Nanoparticles," *Nano Letters,* vol. 11, no. 12, pp. 5128-5134, 2011/12/14 2011.

[5] R. P. Tan *et al.*, "Magnetoresistance and collective Coulomb blockade in superlattices of ferromagnetic CoFe nanoparticles," *Physical Review B,* vol. 79, no. 17, p. 174428, 05/21/ 2009.

[6] A. Zabet-Khosousi and A.-A. Dhirani, "Charge Transport in Nanoparticle Assemblies," *Chemical Reviews,* vol. 108, no. 10, pp. 4072-4124, 2008/10/08 2008.

[7] C. Duan *et al.*, "Controllability of the Coulomb charging energy in close-packed nanoparticle arrays," *Nanoscale,* 10.1039/C3NR02334F vol. 5, no. 21, pp. 10258-10266, 2013.

[8] F. Dassenoy *et al.*, "Platinum nanoparticles stabilized by CO and octanethiol ligands or polymers: FT-IR, NMR, HREM and WAXS studies," *New Journal of Chemistry,* 10.1039/A709245H vol. 22, no. 7, pp. 703-712, 1998.

[9] J. Dugay *et al.*, "Charge transport and interdot coupling tuned by the tunnel barrier length in assemblies of nanoparticles surrounded by organic ligands," *Physical Review B,* vol. 89, no. 4, p. 041406, 01/23/ 2014.

[10] B. Laikhtman and E. L. Wolf, "Tunneling time and effective capacitance for single electron tunneling," *Physics Letters A,* vol. 139, no. 5, pp. 257-260, 1989/08/07/ 1989.

[11] A. A. Middleton and N. S. Wingreen, "Collective transport in arrays of small metallic dots," *Physical Review Letters,* vol. 71, no. 19, pp. 3198-3201, 11/08/ 1993.

[12] R. W. Rendell *et al.*, "Electron transport in nanocluster films with random voids," *IEEE Transactions on Nanotechnology,* vol. 2, no. 2, pp. 75-81, 2003.

Chapter 3: Tunnel magnetoresistance in assemblies of FeCo nanoparticles

3.1 Introduction

Since the downscaling of materials to nanometer scale has come into fashion, magnetic materials have gained tremendous amount of attention [1]. Often termed as nano-magnetic materials, they represent a variety of morphologies such as dots [2], nanowires [3], nanotubes [4], thin films [5] etc. Chemically synthesized magnetic nanoparticles (MNps) in which a metallic core is encapsulated by a layer of organic surfactant, enter this arena with their unique magnetic and magneto-transport properties [6-9]. They show promising features for spintronic devices and already find wide range of applications in magnetic hyperthermia [10, 11], magnetic resonance imaging [12, 13], and sensors [14]. The magnetic nature of these particles is also reflected in their charge transport properties in the form of novel phenomena of tunnel magnetoresistance (TMR). The essence of TMR lies in the spin dependent tunneling (SDT) between two ferro-magnets separated by a tunnel barrier. As we discussed in chapter 1.2, during SDT between two particles, the relative orientations of their magnetic moments govern the tunneling resistance such that a high tunneling resistance is observed when the moments are aligned in an anti-parallel fashion whereas reverse is true for parallel alignment. Since the orientation of the moments changes under the influence of an external magnetic field, so does the resistance of the MNps assemblies. We recall that, in order to quantify the extent of this effect, TMR ratio is usually calculated using following equation:

$$\text{TMR} = \frac{(R_{Max} - R_{Min})}{R_{Min}} \qquad 3(a)$$

where R_{Max} and R_{Min} are the maximum and minimum value of resistance observed while varying the field. In general, R_{Max} occurs when the applied field is close to the coercive field of the assembly while R_{Min} occurs at and beyond saturation field. Black *et al*. first reported a TMR amplitude of 8% at low-temperature in self-assemblies of Co MNps coated with oleic acid [7]. Since then, studies of TMR in assemblies of chemically synthesized particles have gained much attention. Most studies have focused on assemblies of Fe_3O_4 particles due to their relative ease of handling in air. Wang *et al*. have reported a room-temperature TMR of 22% in assemblies of Fe_3O_4 particles coated with polystyrene [15] and 7% for those coated with oleic acid [16]. Arijit *et al*. have reported a TMR of 38% in assemblies of Fe_3O_4 coated with oleylamine [17]. Magnetoresistance in Fe_3O_4 can persist up to high field values due to several possible reasons. It has been suggested that spins at the boundaries of the particles saturate at higher magnetic field compared to the spins at the core of the particles [18] which may give rise to high field magnetoresistance. Beside, in assemblies of non-oxide particles, high field magnetoresistance can arise due to the presence of paramagnetic impurities in the tunnel barrier.

Further enrichment in the transport properties of MNp assemblies comes from Coulomb blockade which prohibits the tunneling between the neighboring particles at low temperature. To counterfeit this effect, higher order tunneling -namely co-tunneling and variable range hopping- come into play [19-22]. Such mechanisms have recently gained much attention as they can significantly enhance the amplitude of low temperature TMR [23, 24].

In the pursuit of better materials with higher TMR amplitude, magnetotransport properties of newly synthesized magnetic materials are frequently reported [8, 25-27]. Bimetallic FeCo MNps are sought to have interesting magnetic properties with tunable magnetization which depends on the composition of the Fe/Co ratio [28, 29]. So far, magnetotransport properties of FeCo have amazed us in various aspects. At LPCNO, previous studies on millimeter long FeCo super-lattices have shown field induced switching and two very different types of magnetoresistance at low field and high field, the later reaching more than 3000% [27]. Besides, when deposited on the substrate, assemblies of FeCo particles coated with oleic acid and hexadecylamine have shown interesting magnetotransport properties with high-field magnetoresistance up to 500% [9]. Theoretical model shedding light on these properties have also been proposed suggesting various possible reasons for such a high field magnetoresistance [43]. However, a clear low-field magnetoresistance in these assemblies could not be observed due to the domination of high-field magnetoresistance. Moreover, the analyses that were performed have shown that these particles were not crystalline FeCo but amorphous, probably due to the presence of carbon originating from the precursors used during the synthesis. This might also be at the origin of the low magnetization measured on these MNPs compared to the bulk [30]. Thus it would be highly desirable to measure the magnetotransport properties of FeCo MNPs with improved structural and magnetic properties.

Recently, FeCo nanoparticles with improved magnetic properties were successfully prepared at the LPCNO by using chemical methods [29]. In this report, we shall present magneto-transport studies performed on the assemblies of these spherical $Fe_{50}Co_{50}$ particles coated with HDA/HCl (Hexadeyl ammonium chloride). We shall first present their synthesis and structural characterization followed by their magnetic properties. We will then present their transport properties in the light of Coulomb blockade, sequential tunneling and co-tunneling phenomenon. Finally, we shall present the TMR studies performed in the temperature range of 1.9 K to 300 K while applying the field in and out of the plane of the assembly.

3.2 Synthesis

Synthesis of spherical $Fe_{50}Co_{50}$ nanoparticles coated with HDA-HCI ligand was carried out by Mathieu Lepesant and Lise-Marie Lacroix ("Nanoparticle and Organometallic Chemistry" group, LPCNO). The synthesis procedure is based on a bottom-up approach whereby the precursors are first thermally decomposed in a solvent under reducing atmosphere to form the short lived atomic species. As the concentration of the atomic species increases in the solution, they start to form nuclei which fuse together and grow over time to form the nanoparticles. Various reaction parameters such as reaction temperature, pressure, relative concentrations of the reagents, reaction time etc. can significantly alter the physical and chemical properties of the resulting nanoparticles and, thus, need to be regulated accordingly to obtain particles of desired shape, size and composition. Below, we present the protocol which is optimized for obtaining $Fe_{50}Co_{50}$ spherical nanoparticles used for our transport studies. Further information on the chemistry and elaborate synthesis procedure can be found in reference [29].

Protocol: In the glove box, 386.3 mg of HDA, 333.5 mg of HDAHCl, 180.7 mg of $[Co(N(Si(CH_3)_3)_2)_2,THF]$ and 150.5 mg of $[Fe(N(Si(CH_3)_3)_2)_2]_2$ were weighed in separate tubes. 5 mL of mesitylene was added to the tube containing HDA, 8 mL to the tube containing HDAHCl and 2.5 mL in each of the tube containing $Co(N(Si(CH_3)_3)_2)_2$ and $[Fe(N(Si(CH_3)_3)_2)_2]_2$ The solution of $Co(N(Si(CH_3)_3)_2)_2$ was then added to the tube containing $[Fe(N(Si(CH_3)_3)_2)_2]_2$ solution followed by the addition of HDAHCl solution while stirring magnetically. Once the solution turned dark blue, HDA solution was added to it and then, the whole solution was transferred to a 180 mL Fischer-Porter priorly washed with a solution of $[Fe(N(Si(CH_3)_3)_2)_2]_2$ in mesitylene.

The Fischer-Porter was then placed in an oil bath maintained at 423 K which results in the evolution of the precursors. One hour later, the Fischer-Porter was placed in cold bath while the color of the solution turned black. The Fischer-Porter was then connected to the hydrogenator whereby the argon atmosphere was replaced by that of hydrogen at 3 bar while continuously stirring the solution magnetically. It was again placed in the oil bath at 423 K for 24 hours. The reaction can be expressed by following reaction equation;

$$[Fe(N(Si(CH_3)_3)_2)_2]_2 + Co(N(Si(CH_3)_3)_2)_2 + 3\ \text{HDAHCl} + 4\ \text{HDA} \xrightarrow[\text{423 K / 1 h / Argon}]{} \xrightarrow[\text{423 K / 24 h / 3 bar } H_2]{}$$

The Fischer-Porter was then transferred back to glovebox and the hydrogen atmosphere was replaced by argon. The particles were precipitated by using a magnet and the supernatant was discarded. The obtained particles were washed 4 times with 10 mL of toluene. Each time the supernatant was discarded while the particles were precipitated using a magnet. After a final washing, nanoparticles were left to dry in the glovebox.

3.3 Characterization

Transmission electron microscopy (TEM**)** images show that particles form assemblies when drop-casted over a TEM grid. As evident from Figure 3.1(a), particles are hexagonally arranged in the assembly with an inter-particle distance of approximately 2 nm. The average size of the particles is found to be 10.3 ± 0.7 nm [Figure 3.1(b)]. The size of the particles can vary slightly from synthesis to synthesis. In two other syntheses carried out in similar manner, the mean particle diameters were found to be 10.2 ± 1.6 nm and 11.5 ± 0.9 nm.

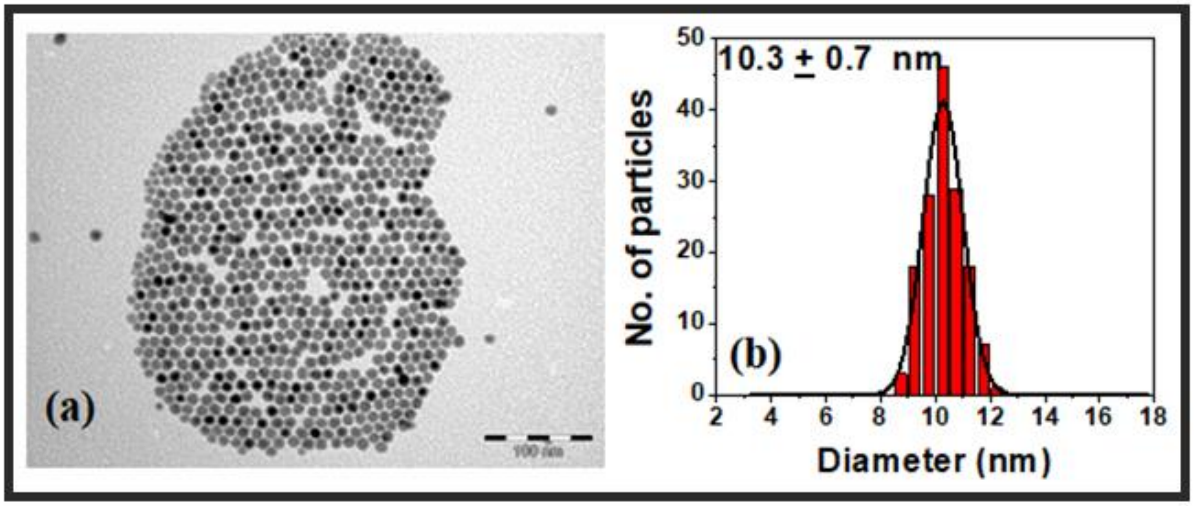

Figure 3.1: (a) TEM image of the particles arranged in a hexagonal fashion in an assembly formed over TEM grid and (b) size distribution of the particles with a mean diameter of 10.3 ± 0.7 nm.

Thermogravimetric analysis revealed that the metallic content of the particles is approximately 85%. Vibrating sample magnetometer (VSM) measurements performed at low temperature (4 K) show a saturation magnetization of 228 Am^2/kg as shown in Figure 3.2 (a). This value is quite close to the expected value of 240 Am^2/kg for $Fe_{50}Co_{50}$. X-ray diffraction (XRD) spectra of particles [Figure 3.2 (b)] show peaks which corresponds to a body centered structure (BCC) of FeCo. Besides, no sign of oxide peaks were observed, indicating that particles were not oxidized during the synthesis.

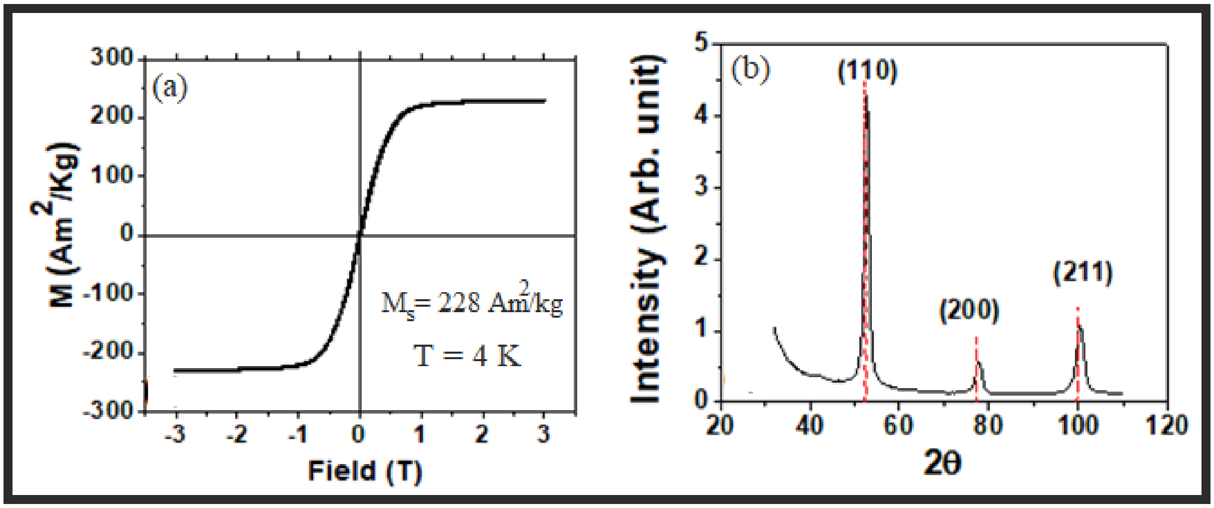

Figure 3.2: (a) Magnetic measurements performed on particles in powder form at low temperature and (b) XRD spectra of the particles showing peaks at different 2θ values. Vertical red lines corresponds to the peaks of BCC structure of FeCo.

3.4 Sample preparation for transport measurements

A 10 mM solution of FeCo particles in THF was sonicated in an air-tight Fischer-Porter for 10 minutes. It was then transferred to the glovebox for deposition over the electrodes. A 10 µl drop of the solution was deposited on a 0.5 cm x 0.5 cm Si/SiO_2 surface carrying lithographically patterned 8 interdigitated electrodes. Each electrode consisted of 20 interdigitated electrodes of width 5 µm, length 80 µm, and height 30 nm. Figure 3.3(a) shows the SEM image of an ensemble of 8 interdigitated electrodes while Figure3.3(b) shows the zoomed view of a single interdigitated electrode.

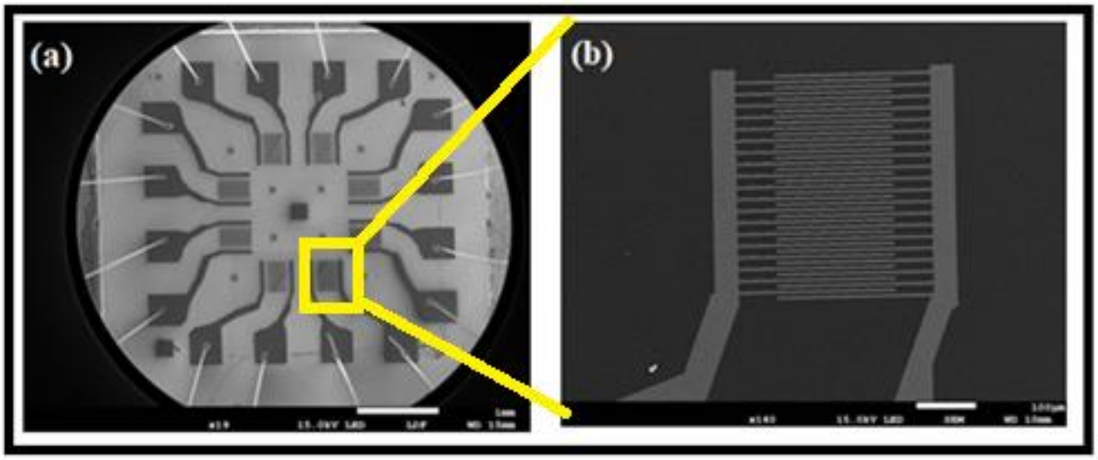

Figure 3.3: SEM image of an interdigitated electrode used for charge transport measurement.

On depositing the drop of solution over interdigitated electrodes, an alternating voltage of 10 V, 10 kHz was applied for approximately 15 seconds (i.e. roughly the time taken by the drop to evaporate). The application of an ac voltage, i.e. dielectrophoresis, is usually employed to effectively fill the gaps between the electrodes, and can be used with various types of nano and micro structures [8, 31-34]. Although dielectrophoresis can be performed by using dc field, ac field is preferred in order to avoid any undesired electrokinetic and electrochemical phenomena. In separate experiments, simple drop cast method was also used to deposit the particles over the electrodes. We shall compare the characteristic of samples prepared by both methods in the later sections. From now onwards, we shall refer the sample prepared by dielectrophoresis as sample A and the sample prepared by dropcasting as sample B.

Whichever method used for deposition, once the particles were deposited, the sample was transferred to a sputtering system for the deposition of a protective alumina layer. The transfer to the sputtering machine takes place via an interconnected chamber between glove-box and sputtering machine where the sample is only exposed to either Ar or remains in vacuum. This allows us to avoid any exposure to oxygen. After deposition of 100 nm thick alumina layer, samples were transferred to a helium cryostat for transport measurements. During this transfer, samples were exposed to air for few 10s of seconds.

Scanning electron microscope (SEM) images were taken from the replica of the samples prepared under similar conditions except that there was no alumina layer deposited over the replicas. This allows us to obtain clear images of the deposited assemblies and avoid any charging effect arising in the SEM due to insulating nature of alumina. The electrode prepared by dielectrophoresis [Figure 3.4 (a)] shows mostly filled interdigitated gaps as expected. Given the height of the electrodes to be 30 nm, completely filled gaps can have up to 3 layers of particles. It has been shown that, in assemblies of particles, charging energy decreases significantly on addition of first few layers of particles [35, 36]. Further addition of layers brings no significant effect on the charging energy. On the other hand, electrodes over which particles were drop casted; contained relatively low number of particles in interdigitated gaps as shown in Figure 3.4(b). Nonetheless, some assemblies spanning the gaps between the electrodes could still be detected, which made them sufficiently conducting for charge transport measurements.

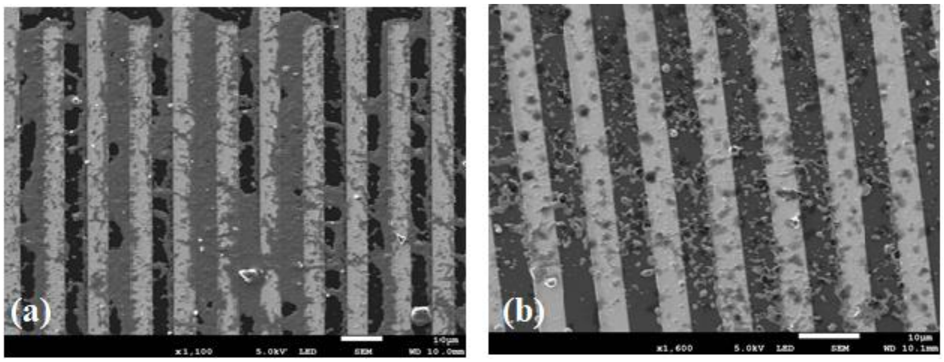

Figure 3.4: SEM images of the replicas of the samples used for charge transport measurements. These samples were prepared by (a) dielectrophoresis at 10 V, 10 kHz and (b) drop casting.

3.5 Current-voltage curves

(a) Room temperature measurements

At room-temperature, *I-V* curves of all measured electrodes showed ohmic behavior irrespective of the method used to prepare them i.e. dielectrophoresis or dropcasting. However, electrodes from sample A (prepared by dielectrophoresis) were found to be highly conducting and showed resistance of the order of few hundred Ohms. On the other hand, electrodes from sample B (prepared by dropcasting) were relatively resistive with dispersed room-temperature resistance in the range of kΩ to MΩ. Figure 3.5 shows the *I-V* curve of a representative assembly from sample A and B. The low resistance value of the electrodes from sample A could have two possible reasons. First and most probable is the large number of particles trapped between the electrodes as evident from the SEM image [Figure 3.4(a)]. Larger number of particles can result in significantly lower value of overall resistance of the assembly. Second possible origin could be application of high voltage during dielectrophoresis. Subjecting the organic ligands to a high voltage could result in the burning of the organic shell. This could reduce inter-particle distance and cause coalescence of the particles in the assembly. Such a phenomenon may result in metallization of the particles, resulting in low resistance of the assembly. We shall shed more light on this aspect by comparing the charging energy in later section.

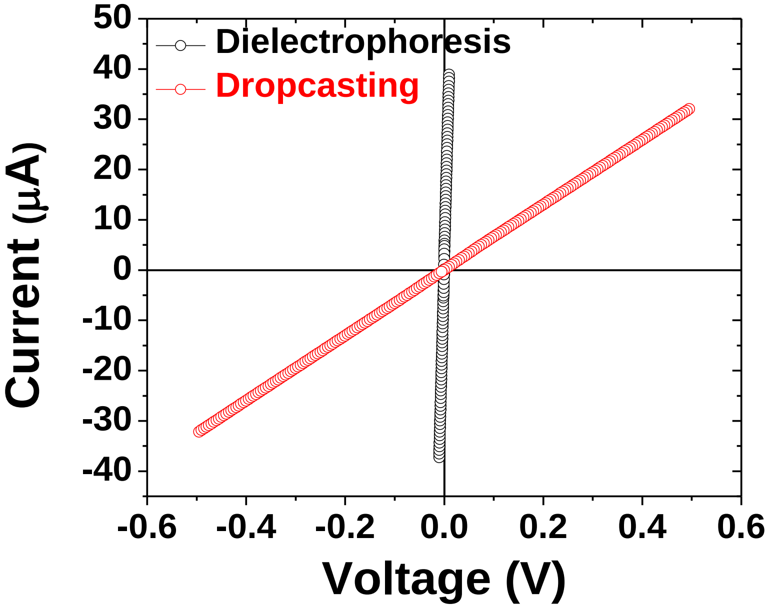

Figure 3.5: Room temperature *I-V* characteristics for electrodes prepared by dielectrophoresis (black) and drop casting (red).

(b) Low temperature measurements

We performed low temperature electrical measurements on several electrodes from sample A and B. On decreasing the temperature, *I-V* curves followed ohmic behavior, and showed no sign of non-linearity in the temperature range of 300 K to 100 K. However, the resistance of the assembly increased with decrease in temperature in all cases. This indicates that the structure of the particles remained preserve and no metal percolation path existed between the electrodes. For the electrodes from sample B, the first sign of non-linearity in the *I-V* curves occured at ~50 K, marking the beginning of Coulomb blockade regime. Further decrease in temperature resulted in an increase in non-linearity, and progressive opening of the Coulomb gap. Figure 3.6 (b) show the *I-V* curves obtained at different temperatures for a representative electrode from sample B. Appearance of Coulomb gap at low temperature is a typical feature of particle's assemblies, and occurs due to the reduced thermal energy available to overcome the charging energy. The presence of a clear Coulomb blockade regime in these assemblies makes them interesting for the magnetotransport studies.

On the other hand, electrodes from sample A showed only slight non-linearity in the *I-V* curves at temperatures below 6 K. No significant Coulomb gap could be observed in the electrode from sample A. Figure 3.6 (a) shows the I-V curves for one representative assembly from sample A.

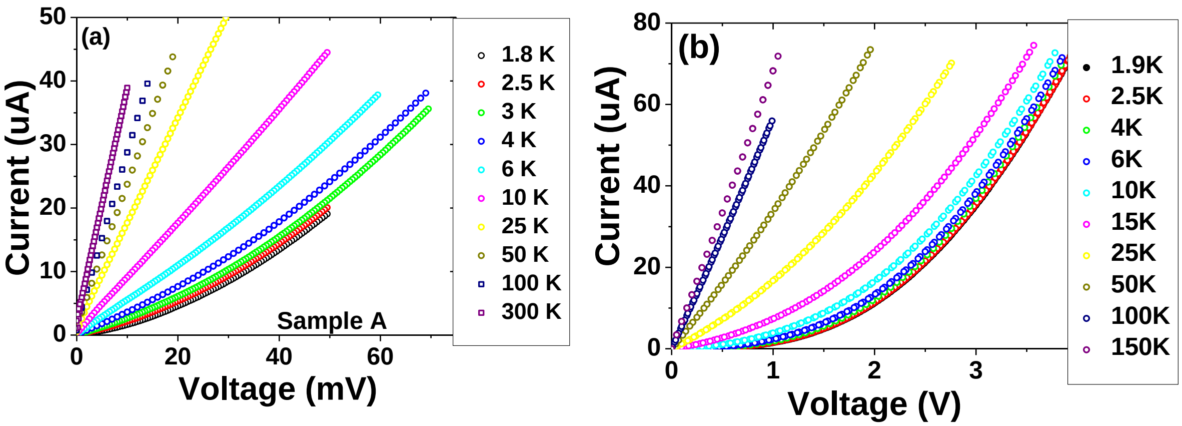

Fig. 3.6: *I-V* curves obtained at different temperatures for assemblies prepared by (a) dielectrophoresis and (b) dropcasting.

3.6 Resistance-temperature curves

Resistance-temperature relationship is often studied to analyze the charge transport mechanism in an assembly. In certain cases, a single charge transport mechanism may prevail at all temperatures [7, 37-39] whereas two or more transport mechanisms dominating in different temperatures regimes have been also reported [20, 40]. Here, we shall present the temperature dependence of resistance in our assemblies in high and low temperature regimes, and analyze the mechanism of charge transport in these temperature regimes. Resistance of the assemblies increased rapidly with decrease in temperature manifesting a typical Coulomb blockade behavior [see Figure 3.7]. At higher temperatures (between 70 K and 200 K), the charge transport mechanism is found to be different than the one observed at low temperatures (below ~40 K). The transition from one mechanism to another takes place gradually in the range of 40 K to 70 K and varies slightly from one electrode to another. In the next section, we shall analyze the mechanism of transport in these temperature regimes.

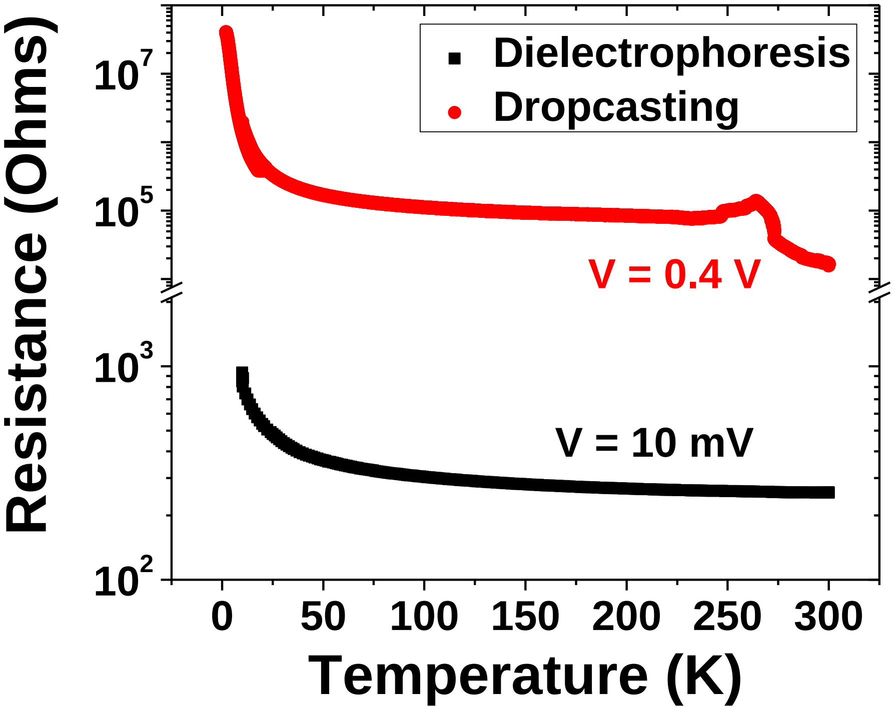

Figure 3.7: Resistance versus temperature curve for the electrodes prepared by dropcasting and dielectrophoresis showing the increase in resistance at low temperature.

(a) High temperature (above ~70K): Sequential tunneling regime

From 70 K to 200 K, resistance of the assemblies could be well described by the Arrhenius equation [eq. 3(b)] which indicates that electron transport between the particles takes place by the mechanism of sequential tunneling. In sequential tunneling, electron tunnels only to the nearest neighbor and follows the relation:

$$R = R_o \, \exp\left(E_c/k_b T\right) \qquad 3(b)$$

where E_c is the charging energy, k_b is the Boltzmann constant and R_o is the intrinsic resistance of the assembly. In order to obtain the charging energy, ln(R) versus 1/T is often plotted as shown in Figure 3.8 (a). Slope obtained from the linear fit of this curve is then used to obtain the value of charging energy. For the assemblies prepared by dropcasting, the obtained value of charging energy is 4.4 me*V*. The theoretical value of charging energy can be obtained from Laikhtman's model which predict the charging energy as

$$E_c = \frac{e^2}{2\, C_\Sigma} \qquad 3(c)$$

where C_Σ is the total capacitance, which includes the self-capacitance of the particle and the capacitance between the particle and its neighbors. It is formulated as

$$C_\Sigma = 2N\pi\varepsilon_o\varepsilon_r r \ln(1 + 2r/s) \qquad 3(d)$$

where N is the number of nearest neighbor, r is the radius of particle, s being the separation between the particles. ε_o and ε_r are the permittivity of the vacuum and relative permittivity of the ligand respectively. Theoretical value of charging energy was calculated by using the values of r (~5.1 nm) and s (~1.9 nm) which were determined from the TEM images. Considering the value of relative permittivity to be 2.7 [41] , we estimated the value of charging energy to be 4.6 me*V*.

Experimental value of charging energy obtained for one representative electrode from sample A was found to be ~2.5 me*V* which is not too far from the value expected theoretically. On the other hand the, charging energy obtained for the electrode from sample B was found to be 4.4 me*V*, which is in excellent agreement with theoretically expected value of 4.6 me*V*. The difference between the charging energies of electrodes from sample A and B cannot be attributed to the difference in size of the particles in both assemblies. This is because the particles size used for the sample B (10.3 ± 0.7) and sample A (10.2 ± 1.6) nm were quite close. A small difference in size should not change the charging energy by a factor of 2. This can be further understood with the help of Figure 3.8 (b), which shows the variation in charging energy as a function of radius of the particle and the experimental values obtained for the two assemblies. In order to have a charging energy of 2.5 me*V* , particle's diameter should be well above 13 nm, which is not the case.

The second possible reason for lower charging energy in case of sample A could be the larger number of particles in the assembly. It can be understood in terms of capacitance of the particles. For example, in a 2D monolayer, the maximum number of nearest neighbor for any particle is 6, which increases up to 9 for a bilayer and 12 for a tri-layer. Increases in number of nearest neighbor can significantly enhance the capacitance between the particles and consequently decreases the charging energy.

Despite of the difference in their charging energy, the mechanism of charge transport in both the assembly remains essentially the same at higher temperatures. Since the assemblies prepared by dielectrophoresis have shown an increase in resistance with decrease in temperature and charging energy similar to that of assembly prepared by dropcasting, it suggests that the dielectrophoresis did not burn the ligands so as to create metallic paths inside the assembly.

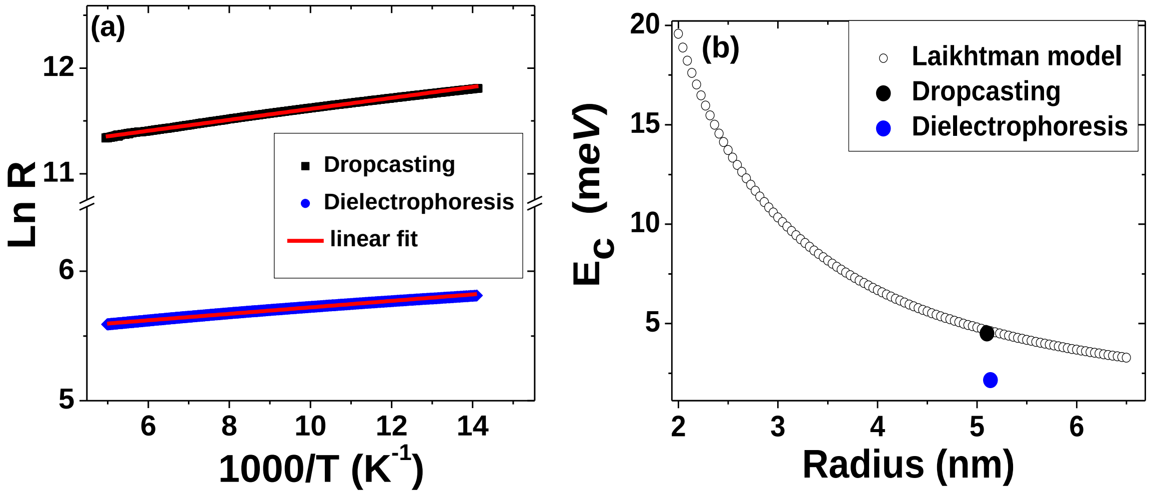

Figure 3.8: (a) ln(R) plotted against inverse of temperature showing a linear trend which indicates that the charge transport takes place through sequential tunneling at high temperature and (b) Charging energy as a function of radius as predicted by Laikhtman's model (hollow circles) and the experimentally obtained charging energy for assembly prepared by dropcasting (black solid circle) and dielectrophoresis (blue solid circle).

(b) Low temperature (below ~40 K) : Co-tunneling regime

For electrode from sample B, resistance starts to deviates from T^{-1} dependence and no longer follow sequential tunneling regime below 70 K. Instead, a $T^{-1/2}$ dependency progressively emerges which dominates completely below 40 K. The cross-over from T^{-1} to $T^{-1/2}$ is gradual and varies from assembly to assembly in the range of 40 K to 70 K. In order to understand such a behavior, one needs to consider that the charging energy of this electrode is observed to be ~55 K (4.4 meV). Therefore, Coulomb blockade is expected to dominate around this temperature and the current in the device should be blocked at low voltages. Nevertheless, a small leakage current can still flow via the mechanism of correlated tunneling (co-tunneling) whereby electrons can tunnel through the particles via the virtual intermediate states.

Similar $T^{-1/2}$ behavior was observed for the electrode from sample A. However, $T^{-1/2}$ dependency in this electrode occurred at much lower temperature compared to the electrode from sample B. In co-tunneling regime, the resistance in an assembly varies as given by,

$$R = R_o \left[\exp \left(T_o/T\right)^{1/2} \right] \qquad 3(e)$$

where T_o is the activation temperature. For precise measurement of resistance at low-temperatures, near zero-bias resistance was obtained from the *I-V* curves measured at different temperatures. Figure 3.9(a) shows the variation of ln R with $T^{-1/2}$. A linear trend could be observed for the electrode from sample A (dielectrophoresis) and sample B (dropcasting) as evident from the mentioned figure. The values of T_o obtained from the linear fit was found to be 414 K and 25 K for the electrodes from sample B and A respectively. An important relation between T_o and the localization length (ξ) of the electron is given by equation $3(f)$. For weakly coupled particles, the ξ value should be less than $2r$ (r being the radius of the particle).

$$T_0 = \frac{2.8\, E_c\, r}{k_b \xi} \qquad 3(f)$$

Using equation $3(f)$, the ξ values for electrode from sample B was found to be 1.8 nm ($0.35r$) whereas the same in case of sample A was 14.5 nm ($2.8r$). This shed light on the inter-particle coupling in two assemblies. Smaller ξ values of $0.35r$ in case of sample A suggests a weak inter-particle coupling, and that the electron remain well localized within the particle. Higher ξ value in assembly prepared by dielectrophoresis indicates relatively higher coupling between the particles exists in this case. Such a difference in inter-particle coupling is unexpected as the same ligand is used in both the cases which should provide similar inter-particle distance and permittivity. However, we hypothesize that in case of sample A, interdigitation of the ligand could have occurred due to the dielectric force during the sample preparation. This may result in smaller inter-particle distance and consequently higher inter-particle coupling. This can also justify the higher conductivity and lower charging energy observed in this case.

On the other hand, *I-V* curves in the co-tunneling regimes cannot be described by Middleton-Wingreen equation. Tran *et al.* have provided an expression of current in the co-tunneling regime [19, 20] which is :

$$I \sim I_o V_{jun}\, g^j \{ \left[(eV_{jun})^2 + (k_b T)^2 / E_C^2 \right] \}^{j-1} \qquad 3(g)$$

where g is the normalized conductivity per tunnel junction, E_c is the charging energy, and j is the number of tunnel junctions involved in the co-tunneling event. In order to calculate the normalized conductivity per tunnel-junction, we assumed the gaps between the electrodes to be completely filled with particles. Using equation 3(g), *I-V* curves at different temperatures could be fitted to obtain the values of *j*. For both type of samples, value of *j* remained very close to 1 at temperatures above ~50 K. This indicates that sequential tunneling takes place above 50 K. Below this temperature, values of *j* evolved continuously and reached a maximum of 2.2 at temperature 2.5 K sample B. This indicates that the effect of co-tunneling becomes stronger as the temperature is lowered down. It also signifies that the low energy sites in the assembly are becoming far and far with decrease in temperature. This is the direct consequence of size dispersion of particles present in the assembly, where the bigger particles (which act as low energy site) are separated far from each other due to their low number density.[21]

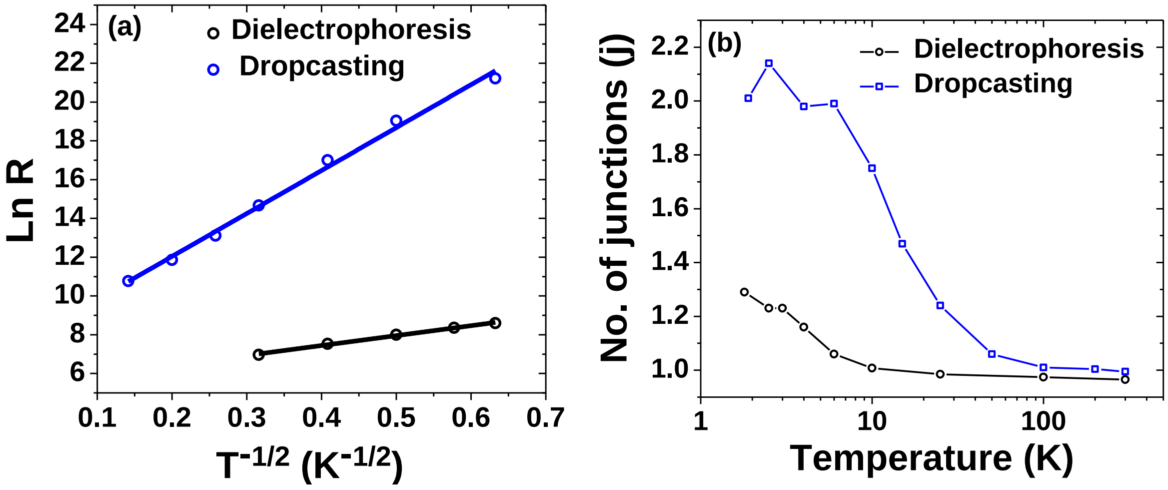

Figure 3.9: (a) A plot of lnR versus $T^{-1/2}$ for the electrode from sample A (dielectrophoresis) and B (dropcasting) .(b) Evolution of number of junctions involved in the co-tunneling with temperature. At high temperature, number of junctions approaches to 1 which indicates that charge transport occurs by sequential tunneling. At low temperatures, value of *j* increases indicating the presence of co-tunneling mechanism.

Electrode from sample A also showed increase in value of *j* at low temperatures. In this case, the maximum value of *j* observed at 2.5 K was close to 1.3 as shown in Figure 3.9 (b). The comparison of *j* values in both type of assemblies suggest that the co-tunneling is more present in the case of assemblies prepared by drop casting methods. This can be explained on the basis of more conduction paths available in the assemblies of higher dimension. For example, in case of a 1D assembly, current would essentially flow through one path. In such a case, the chances of co-tunneling event at low temperature would be enhanced when the particles are of different sizes. As for the assemblies of higher dimension, several current paths would exist. Some of these current paths may offer lower resistance, and current would preferentially flow through them instead of co-tunneling.

Apart from the temperature, co-tunneling phenomenon is also affected by the applied voltage at the junction of the particle. Recently, it has been shown that there may be three co-tunneling regimes in which current may vary differently with applied voltage [42]. These co-tunneling regimes and their prevailing conditions are given below:

Regime 1: $I \propto V,$ when $eV_{jun} \ll k_bT$ $\quad 3(h)$

Regime 2: $I \propto V^{\alpha}$ where $\alpha = 2j - 1$, when $k_bT < eV_{jun} \ll k_bT \ln\left(\frac{e^2}{h}R_T\right)$ $\quad 3(i)$

Regime 3: $I \propto \exp\left[-\sqrt{\frac{V^*}{V}}\right]$ when $k_bT\ \ln\left(\frac{e^2}{h}R_T\right) < eV_{jun} \ll k_bT$ $\quad 3(j)$

In case of dropcasted assembly, we further investigated how the number of junctions (*j*) involved n the co-tunneling varies as a function of applied voltage.

At low temperatures, equation $3(h)$ was valid only at very low voltage. For example, at 2.5 K, condition for equation $3(h)$ will previal only below 0.8 me*V*, which is significantly lower than the applied voltage in our case. However, we found that the condition of regime 2 was satisfied in case of assembly prepared by dropcasting (sample B). To find the value of α from equation $3(i)$, derivative of ln*I*/ln*V* was plotted from which the α values were extracted as a function of voltage. From the voltage dependent α values, we could extract the voltage dependent *j* values. Figure 3.10 shows the variation of *j* as a function of voltage at different temperatures ranging from 2.5 K to 50 K. At low temperatures, the value of *j* first increases slightly from 2 (at 4 *V*) to 2.8 (at ~1*V*). On further decreasing the voltage, a decrease in the values of *j* is observed. In general, extent of co-tunneling is expected to increase at lower voltage; however the reduced value of *j* suggests a decrease in co-tunneling below certain voltage. As the temperature is increased, the value of *j* increases and becomes less and less sensitive to voltage.

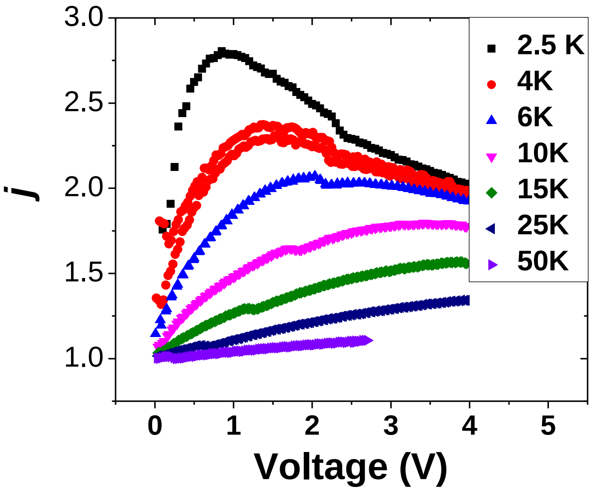

Figure 3.10: Variation in number of junctions (*j*) as a function of applied voltage at different temperatures.

3.7 Tunnel magnetoresistance

(a) Sample A: prepared by dielectrophoresis

We have performed TMR measurements in FeCo assemblies in the temperature range of 1.8 K to 300 K. At room temperature, TMR amplitude varied slightly from assembly to assembly and lied close to 0.5%. For the assemblies prepared by dielectrophoresis, despite of their low resistance, a clear room-temperature TMR could be observed as shown in Figure 3.11(a). Decrease in temperature caused an increase in TMR amplitude. At low temperature, the TMR amplitude was close to 2.8% as shown in Figure 3.11 (b).

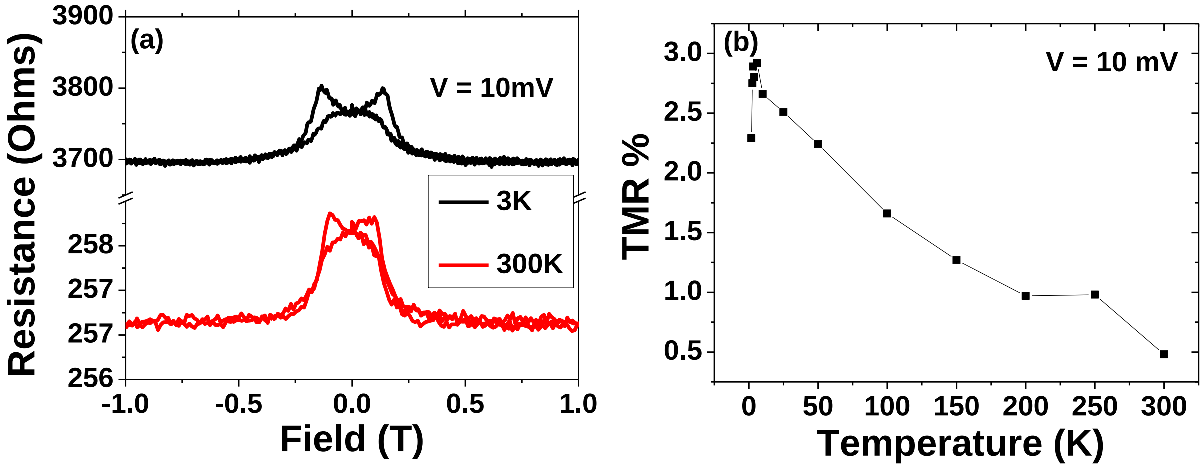

Figure 3.11: (a) TMR curves at 300 K and 3 K for the assembly prepared by dielectrophoresis. (b) Variation in TMR amplitude with respect to temperature in the same assembly.

(b) Sample B: prepared by drop casting

Assemblies prepared by drop casting also showed an increase in TMR amplitude on decreasing the temperature. For sample B, we could study the TMR while applying the field parallel (in plane) and perpendicular to the plane (out of plane) of the film. The curves measured in the case of an in-plane field are shown in Figure 3.12(a). To measure these curves, an applied voltage of 2.5V was used below 50 K, whereas a voltage of 0.75 was used above 50 K. The higher voltage values were used at low temperature in order to measure sufficient current in the assembly. However, as the current increased at high temperature, the value of applied voltage was reduced in order to avoid any damage to the assembly. At low temperature, a TMR amplitude close to 3.8% could be observed, which changed with the voltage at low temperature as we shall discuss later.

Similarly, TMR curves for the field direction perpendicular to the film are shown in Figure 3.12 (b). Here also, different voltages were used at low and high temperature. Below 50 K, an applied voltage of 3 V was used which was decreased to 0.75 V above 50 K. However, as we shall discuss later, TMR amplitude remain almost voltage independent above 50 K whereas it starts to become more and more sensitive to the applied voltage as the temperature goes below 50 K.

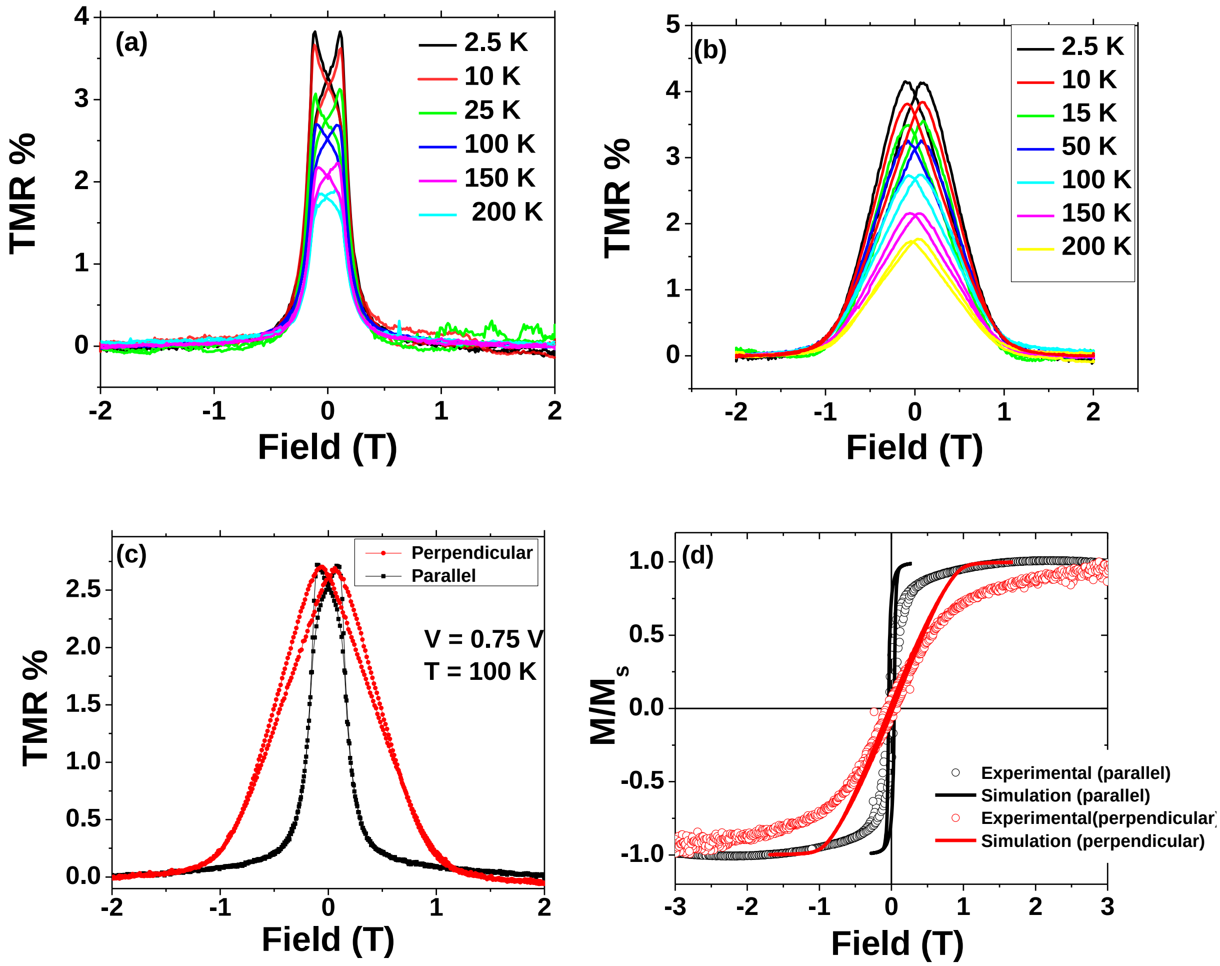

Figure 3.12: (a) TMR curves obtained at different temperatures (measured at 2.5 V for T <50 K, and at 0.75 V for T > 50 K) with external magnetic field parallel to the plane of the assembly, (b) TMR curves at different temperatures for applied field perpendicular to the plane (measured at 3 V for T< 50 K and 0.75 V for T > 50 K), (c) TMR curves at 100 K (0.75 V) for both field configurations and (d) Normalized *M-H* curve obtained at 4 K for an assembly deposited over Si/SiO$_2$ showing higher saturation field when applied field is perpendicular to the plane of assembly (red circles) and low saturation field for applied field parallel to the plane of the assembly (black circles). Monte-Carlo simulations (solid line) support the experimental data showing the similar behavior in both field configurations.

The fact that TMR is governed by the magnetization reversal in the assembly is supported by the different shapes of TMR curves obtained while applying the magnetic field parallel and perpendicular to the sample plane. Figure 3.12(c) shows the TMR curves obtained in the two field directions at 100 K for an applied voltage 0.75 V. As evident from the figure, when the external field is parallel to the sample plane, a sharp peak is observed near the coercive field of the assembly. Further increasing the field causes a sharp decrease in resistance. This indicates that the particles are saturated using moderate fields. On the other hand, when the field is perpendicular to the plane of the assembly, the resistance saturates at much larger field. From these observations, it can be concluded that the easy axis of the assembly lies in the plane of the assembly suggesting that the assembly remains essentially two dimensional as expected.

Magnetic measurements performed on the assemblies of particles show similar behavior where the magnetic moment saturates at much higher field in case of field direction perpendicular to the plane; whereas saturation occurs at lower field values in case of field parallel to the plane of the assembly. Experimental *M-H* curves are shown by circles in Figure 3.12 (d) for both field directions.

Our collaboration with the group of Dr. Varhsa Banerjee (Department of physics, Indian Institute of Technology, Delhi) permitted us to support these results using simulations. Monte Carlo simulations were performed by Arun Kumar Bupathy for 2D assemblies of magnetic particles with triangular lattice. The simulated *M-H* curves are shown by solid lines in Figure 3.11(d). As evident from the figure, simulated curves also support the higher saturation field in case of its direction perpendicular to the plane of assembly. Although the simulated and experimental curve do not superimpose perfectly, they follow the same trend. The difference between the simulated and the experimental curves could arise due to the fact that perfect 2D assemblies are not used for experimental studies and (b) presence of defects in the assemblies which may also affect the saturation field of the assembly.

3.8 Temperature dependence of TMR

As mentioned previously, the TMR amplitude in both sample A and B showed a temperature dependency where TMR amplitude increased significantly at low temperatures. For sample A, TMR amplitude close to 3% could be observed whereas the same for sample B was close to 4%.

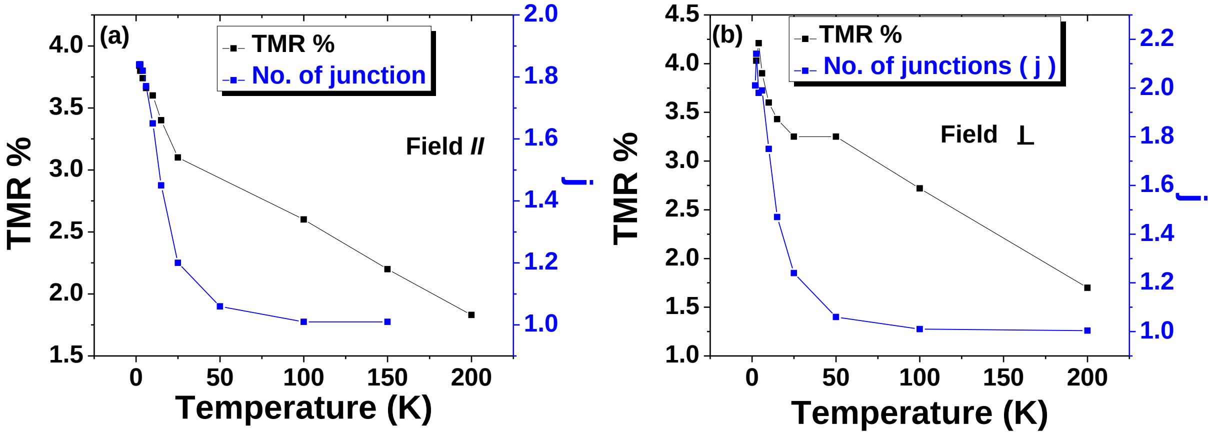

Figure 3.13: Evolution if TMR amplitude and j as a function of temperatures when the applied field is (a) in plane, and (b) out of plane of the assembly.

The variation in TMR amplitude for sample B is shown in Figure 3.13(a) for field parallel to the plane and in Figure 3.13(b) for field applied out of plane. In the high temperature regime, TMR amplitude increased from ~1.75% to 3.2% while decreasing the temperature from 200 K to 50 K (corresponding to an increase of 0.01% /K, if linear trend is assumed). Below this temperature, the amplitude of TMR increased rather sharply and increased from 3.2% to 3.8% from 25 K to 2.5 K (corresponding to an increase of 0.02%/K, if linear increase in assumed). For one of the measured electrode, TMR% could increase upto 12% at low temperature (not shown here). The temperature dependence in assemblies of particles is often attributed to the spin-flipping inside the tunnel barrier. As the temperature decreases, the spin-flipping process reduces which results in increase in TMR amplitude.

In our case, the variation of TMR amplitude at high temperature regime could be attributed to the spin flipping. However, the steep increase in TMR at low-temperature is unlikely to be explained on the basis of spin-flipping alone. It has been shown that, at low temperature, higher order tunneling can significantly enhance TMR amplitude. In studied samples, it has been observed that co-tunneling progressively dominates at temperatures below ~50 K, which could contribute to steep increase in TMR at low temperature. For the applied field in the plane of assembly, Figure 3.13 (a) shows the evolution of TMR% and number of junctions (*j*) involved in the co-tunneling process as a function of temperature. The value of *j* increases above 1 at low temperature. In the similar temperature regime, value of TMR amplitude also increases steeply. This suggests that the sharp increase in TMR amplitude could be related to the co-tunneling. Similar behavior was observed for the applied field perpendicular to the plane of the assembly as shown in Figure 3.13(b).

Thus, the overall temperature dependence of LF-TMR in our assemblies can be attributed to the combined effect of spin-flipping and co-tunneling processes, where the former might be dominating at higher temperatures regimes and later in low temperature regime. Similar temperature dependence has been observed by Wang *et al*. [43] and others [24] in assemblies of particles.

3.9 Voltage dependence of magnetoresistance

At temperatures above 50 K, TMR amplitude showed no voltage dependence in any of the studied assembly in the voltage range of 0.25 V to 1.5 V. However, below 50 K, TMR amplitude becomes sensitive to the applied voltage. In contrast to previous reports on nanoparticle assemblies, we have observed an increase in TMR amplitude at higher voltage. Figure 3.14 (a) and (b) show the TMR curves obtained at different voltages at 6 K for field parallel and perpendicular to the plane of the assembly respectively. The voltage dependency progressively disappears at higher temperature where the amplitude of the TMR remains almost unchanged.

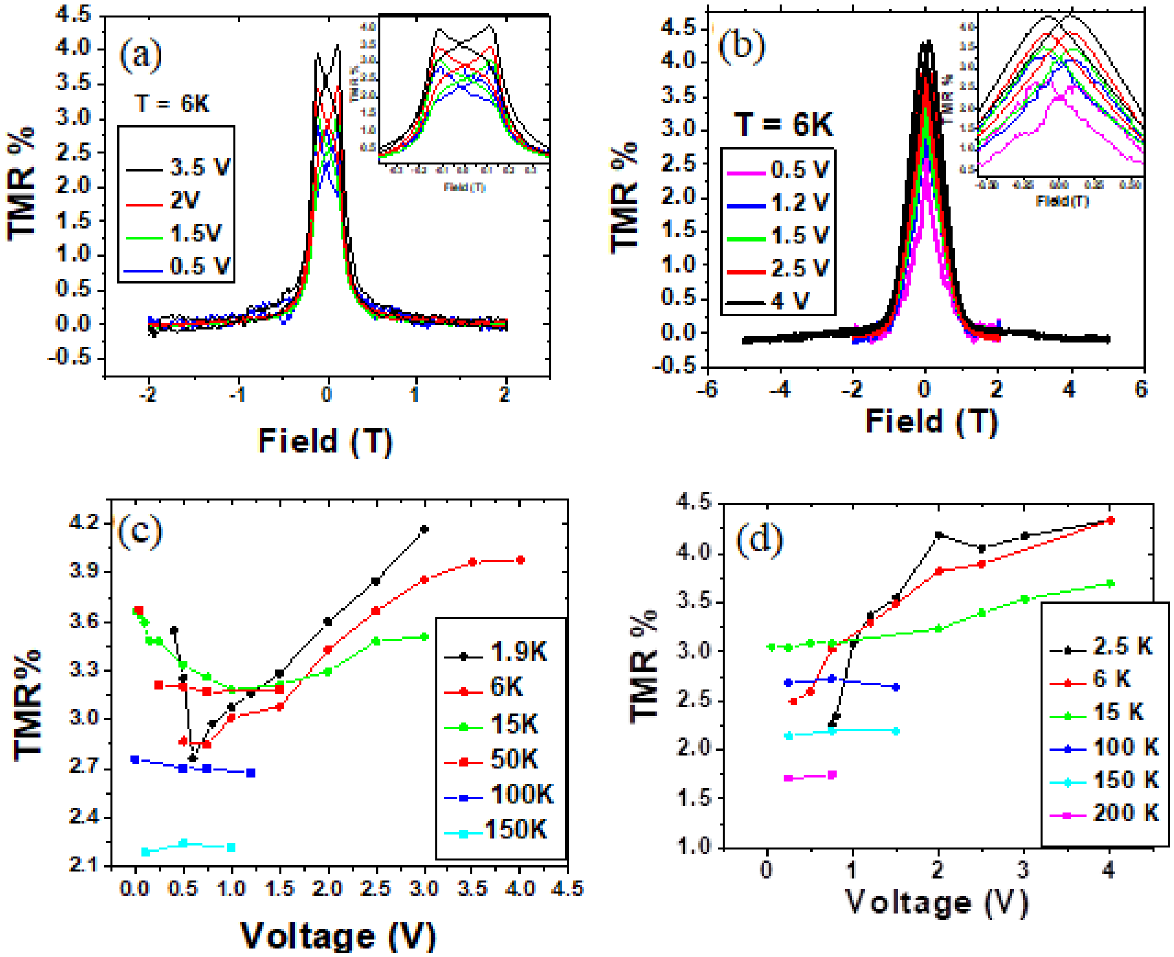

Figure 3.14: Low-temperature TMR curves at different voltages for applied field (a) in-plane and (b) out of plane of the assembly. Voltage dependency of TMR amplitude at different temperatures for field direction (c) in plane and (d) out of plane.

Generally, in magnetic tunnel junction, the TMR decreases with increase in voltage which is explained by the fact that, at high voltages, electrons with an energy higher than the Fermi level release magnons after crossing the barrier. This release of magnons causes a decrease in TMR amplitude by promoting spin-flipping process [44]. In our assemblies, the trend is opposite. An explanation for this unexpected behavior could come from the co-tunneling process. If the value of *j* depends on the applied voltage, and if *j* increases with voltage, this might induce a rise in the TMR amplitude. To try to test this hypothesis, we plot the variation in *j* and TMR amplitude as a function of voltage. We could observe somewhat similar tendency for both j and the TMR amplitude as a function of voltage as shown in Figure 3.15. As evident from figure, the *j* values remain close to 2 at higher voltages and show no significant changes. On decreasing the voltage, value of *j* starts to decrease and tends towards 1.

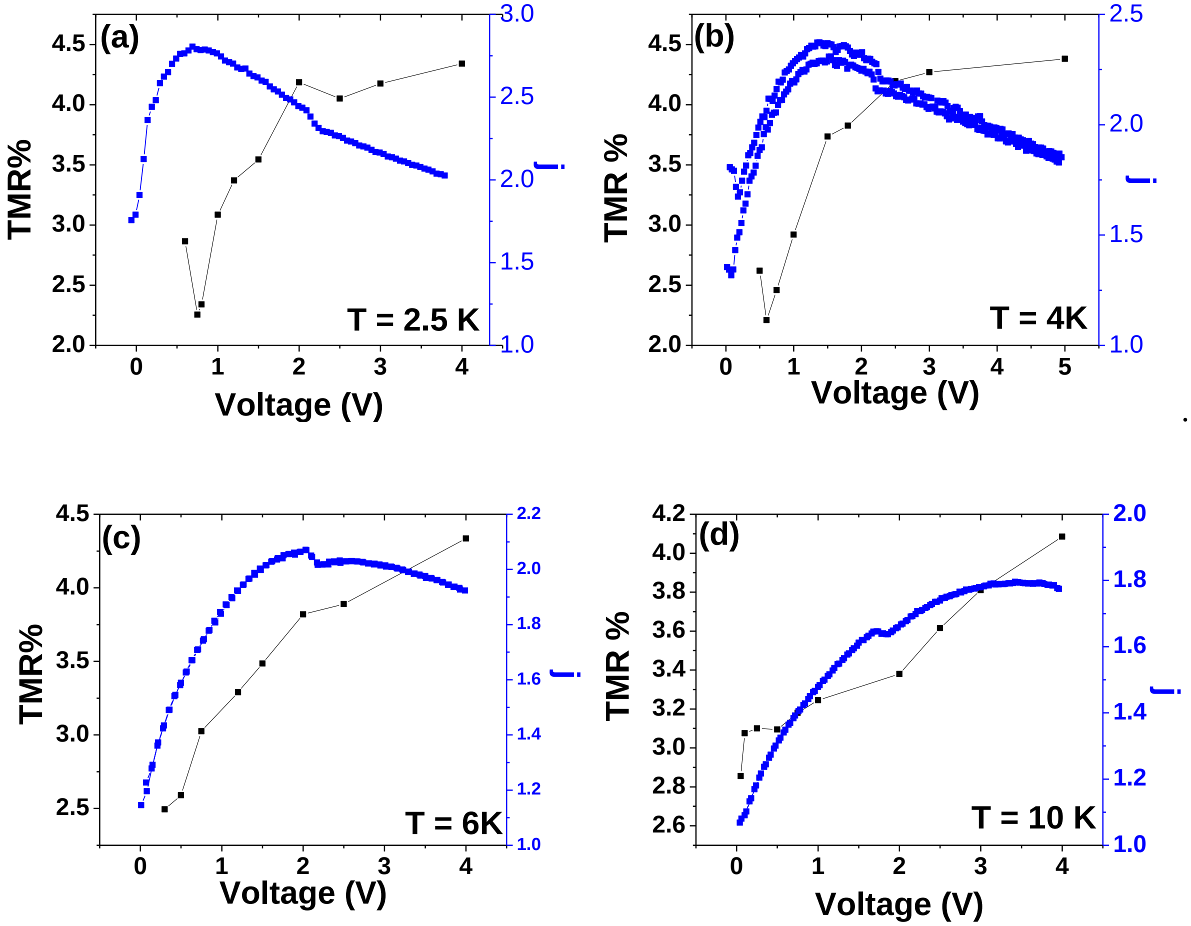

Figure 3.15: Variation in the TMR amplitude and *j* values as a function of voltage at different temperatures in low temperature regime for perpendicular field configuration. A similar trend can be observed in both the quantities.

3.10 Highest observed TMR amplitude

Among the drop-casted assemblies, TMR amplitude at low temperature varied between ~3 to ~11% from assembly to assembly. Here, we present the case study of the sample with highest observed TMR amplitude. This sample was prepared by drop casting (11.5 ± 0.9 nm) and showed a room-temperature resistance of ~ 4 MΩ which is much higher than the two electrodes discussed in previous sections which had 300 Ω [sample A: dielectrophoresis] and 16 kΩ [sample B: drop casting]. A clear Coulomb blockade behavior could be observed at low temperature as shown in Figure 3.16(a). Analysis of resistance-temperature plot at higher temperature shows that charging energy for this electrode was 6.1 meV [see Figure 3.16(b)], which is again higher than previous two electrodes discussed i.e. sample A [2.5 meV] and B [4.4 meV].

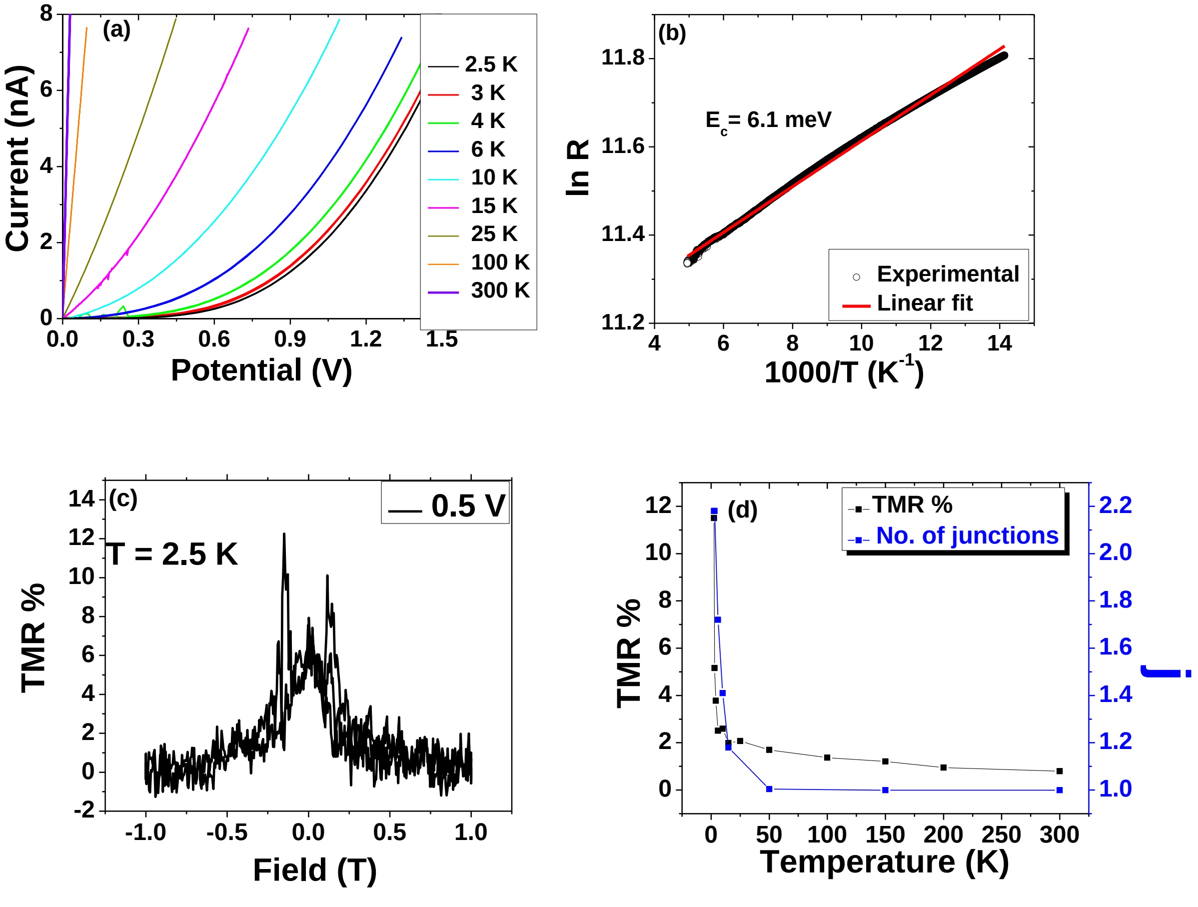

Figure 3.16: (a) *I-V* curves of a drop casted electrode which was found to be most resistive, (b) ln(*R*) versus 1/*T* plot for the same electrode showing a linear trend at higher temperature. The charging energy corresponds to 6.1 meV, (c) TMR curve of the assembly at 0.5 V and 2.5 K, and (d) variation in number of junctions involved in the co-tunneling and TMR amplitude as a function of temperature for the same assembly.

At 2.5 K, TMR could be observed on this electrode and showed maximum amplitude of ~11% as shown in Figure 3.16(c). This amplitude is the highest observed among all the electrodes we studied. Figure 3.18 (d) show the variation in TMR and number of juntions (*j*) involved in co-tunneling as a function of temperature for this electrode. The TMR amplitude decreases rapidly to 2.2 % as the temperature is increased to 10 K. Similar trend is followed by *j*.

3.11 High Field MR (HF-MR)

Under the conditions of low voltage and low temperature, certain magneto-resistive effects could be observed in the assemblies at higher magnetic field values. These high field magnetoresistances (HF-MR) could not be related with the magnetization reversal in the assemblies, and are attributed to several other phenomena as we shall discuss in subsequent section. We shall first discuss the form of the resistance- field curve in the presence of these HF-MR and then present their tendencies with respect to temperature and voltage. We shall take the example of some of the electrodes which were prepared by dielectrophoresis as well as drop casting.

(a) Shape of the MR curve

Figure 3.17 shows a MR curve obtained at 2.5 K, 10 mV from a representative electrode of sample A [prepared by dielectrophoresis]. In the MR curve, three field regimes can be seen where the MR behaves differently. Just above the zero field, the conventional **TMR** is observed, which is explained by magnetization reversal in the assembly. The essence of this TMR lies in the spin dependent tunneling and magnetization reversal in the assembly as we have seen previously. It is indicated by green arrows in Figure 3.17. When the field is increased above the saturation field, the resistance of the assembly starts to increase as shown by red arrows. We refer this magnetoresistance as $\mathbf{MR_1}$. It increases with the field up to a certain field values above which the resistance of the assembly starts to decrease again due to another type of magnetoresistance which persists at higher field values. We refer this magnetoresistance as $\mathbf{MR_2}$. It is indicated by blue arrows.

Although the explanation for TMR is known, the reason of MR_1 and MR_2 are not very clear. However, this is not the first time that such high-field magnetoresistance have been observed. Previously at LPCNO, similar behavior has been reported in FeCo assemblies and superlattices. The HF-MR resembling to MR_2 could reach up to 3000% in that case, however a clear TMR was not observed due to the domination of MR_2. Besides, similar behavior could be observed in the assemblies of Fe nanoparticles at low temperature. In the present case, the maximum amplitude observed for MR_2 does not exceed more than few %, however, a clear TMR has been observed.

It has been proposed that MR_2 could be the manifestation of paramagnetic impurities that might be present in the barrier or at the surface of the particles. Model and theory conforming to this hypothesis has been also proposed at LPCNO [45].

Both MR_1 and MR_2 prevails only under certain condition of temperature and voltage in our assembly. Under a given condition, one of them is dominant over other or completely disappears. We shall present them by taking relevant examples.

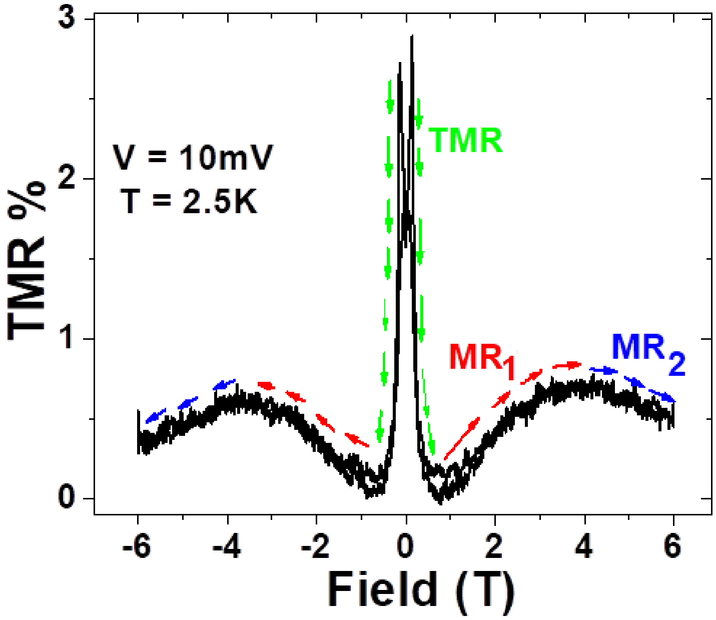

Figure 3.17: A low-temperature MR curve showing the conventional TMR (green arrow) and the high-field MRs. i.e. MR_1 (red arrows) and MR_2(blue arrows).

(b) Tendencies of HF-MR

We first take the example of sample A [dielectrophhoresis] to show the tendencies of HF-MR. **At T = 1.8 K,** MR_1 becomes significantly dominant in this assembly as shown in Figure 3.18(a). At higher fields, resistance stays saturated and MR_2 remains absent. When a significantly low voltage is applied, the shape of the curve appears similar to that of an inverse MR as evident from the MR curve at 1 m*V* in Figure 3.18(a). Amplitude of MR_1 is voltage dependant and vanishes progressively as the voltage is increased from 1 mV to 50 mV (see Figure 3.18a).

The disappearance of MR_2 has been previously observed in the FeCo assemblies where HF-MR similar to MR_2 disappear abruptly below 1.8 K. Such a disappearance of MR_2 at low temperatures has been attributed to paramagnetic-ferromagnetic or paramagnetic-glass transition of the localized magnetic moments.

For **T = 2.5 K,** MR$_2$ appears at higher field which can be seen in the form of decrease in resistance beyond 4 T. While MR$_2$ starts to appear at 2.5 K, the amplitude of MR$_1$ decreases from ~3% to ~0.8% (at V = 5 mV) on increasing the temperature from 1.8 K to 2.5 K. Figure 3.18(b) shows the MR curves as a function of voltage. As the voltage increases, amplitude of MR$_1$ decreases. Figure 3.17(c) shows the variation in amplitude of MR$_1$ as a function of voltage at 1.8 K and 2.5 K. The abrupt increase in MR$_1$ at low temperature can be seen in Figure 3.18(d) showing temperature variation of MR$_1$. These observations suggests that the preferable conditions for HF-MR are low voltage and low temperature.

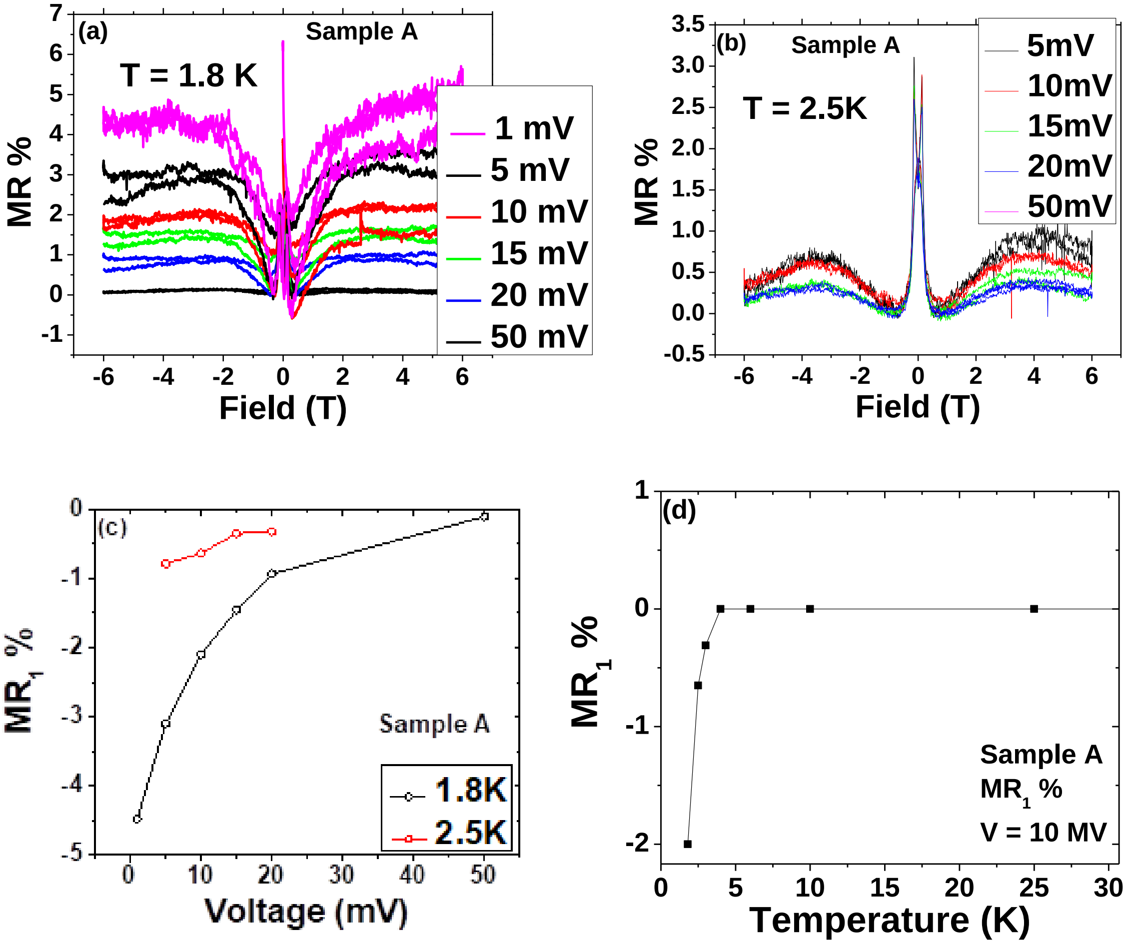

Figure 3.18: (a) MR curves for the assembly prepared by dielectrophoresis showing HF-MR at different voltages at (a) 1.8 K and (b) 2.5 K. (c) Voltage dependence of HF-MR (MR$_1$) at 1.8 K and 2.5 K, and (d) amplitude of MR$_1$ as a function of temperature..

Similar behavior could be observed in other electrodes prepared by dielectrophoresis where the MR$_2$ disappeared at 1.8 K and significantly large MR$_1$ emerged. The highest MR$_1$ observed at

1.8 K corresponds to one of the electrodes prepared by dielectrophresis where an amplitude of roughly 16% could be achieved at 1.8 K and 1 mV, as shown in Figure 3.19(a). Here also, the amplitude of MR1 disappears gradually with increase in applied voltage as shown in Figure 3.19(b).

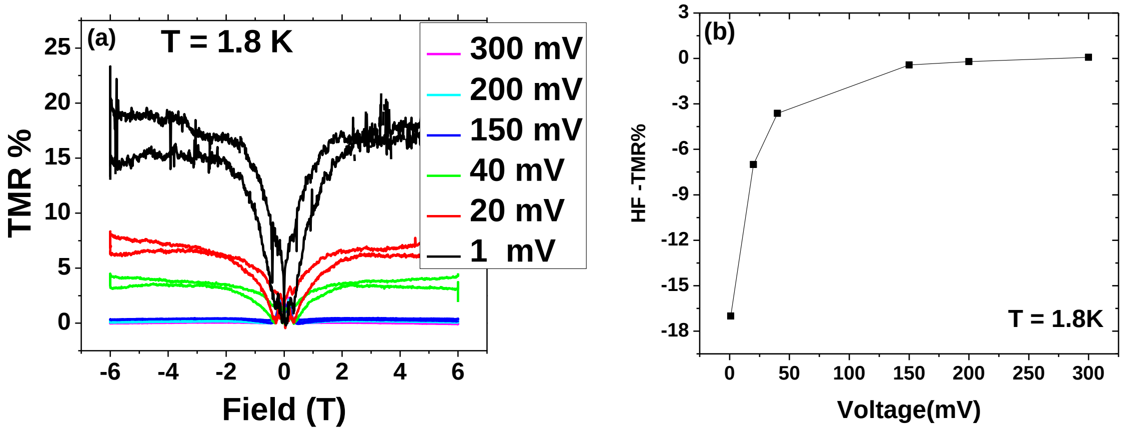

Figure 3.19 (a) MR curves at 1.8 K for an electrode prepared by dielectrophoresis. The MR_1 amplitude was found to be maximum in this electrode and (b) Variation in HF-MR as a function of voltage at 1.8 K.

Similar behavior could be observed in the assemblies prepared by drop casting. Figure 3.20 (a) shows the HF-MR measured at low temperature for one of the electrodes prepared by dropcasting. Here too, the MR_1 vanishes rapidly at higher temperature. Surprisingly, in some cases, we have observed that MR_1 reappears at 15 K. The reason of such reappearance at 15 K is not known.

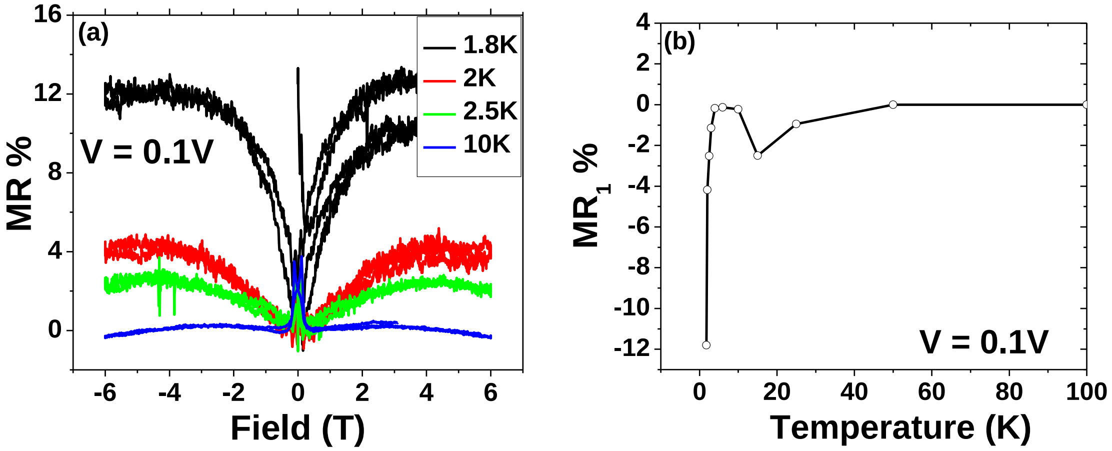

Figure 3.20: (a) MR curves at different temperatures for an electrode prepared by drop casting and (b) variation in amplitude of MR_1 as a function of temperature showing a sudden increase at low temperatures. Beside a reappearance of MR_1 can be seen at 15 K.

3.12 Conclusion

In conclusion, we have studied the magneto-transport behavior of chemically prepared FeCo assemblies. The assemblies of particles could be formed in micrometer sized gaps between the electrodes either by dielectrophoresis or by drop casting. While the advantage of the former technique is the higher conductivity of the prepared electrodes due to efficient filling of gaps, the advantage of the later is the strong influence of Coulomb blockade on transport properties, which permits to study the interaction between the higher-order tunneling process and TMR phenomenon. Analysis of charge transport shows that sequential tunneling takes place at higher temperature regime whereas co-tunneling starts to dominate below ~ 50 K.

Magneto-transport measurements showed a TMR amplitude close 0.5% at room-temperature. At low temperatures, TMR amplitude between 3 to 11% could be observed. The temperature dependency of TMR is attributed to the spin-flipping process at high temperature regime; whereas at low temperatures, it is attributed to the co-tunneling. Besides, a voltage dependency of TMR amplitude also arises in low temperatures regime where an increase in voltage increases the TMR amplitude. Co-tunneling analysis showed that value of j also follows similar trends. We attribute the voltage dependency of TMR amplitude to the changes in j as a function of voltage. Thus, higher values of TMR at high voltages could be related to the co-tunneling phenomenon.

Apart from the conventional TMR, we have observed a high-field magnetoresistance under the conditions of low-temperature and low-voltage. The amplitude of the HF-MR could increase up to 16% at 1.8 K. In most assemblies, HF-MR disappears rapidly around 10 K.

References: Chapter 3-Tunnel magnetoresistance in assemblies of FeCo nanoparticles

[1] S. Bedanta, A. Barman, W. Kleemann, O. Petracic, and T. Seki, "Magnetic Nanoparticles: A Subject for Both Fundamental Research and Applications," *Journal of Nanomaterials,* vol. 2013, p. 22, 2013, Art. no. 952540.

[2] R. P. Cowburn, "Magnetic nanodots for device applications," *Journal of Magnetism and Magnetic Materials,* vol. 242-245, pp. 505-511, 2002/04/01/ 2002.

[3] A. Fert and L. Piraux, "Magnetic nanowires," *Journal of Magnetism and Magnetic Materials,* vol. 200, no. 1, pp. 338-358, 1999/10/01/ 1999.

[4] Y. Ye and B. Geng, "Magnetic Nanotubes: Synthesis, Properties, and Applications," *Critical Reviews in Solid State and Materials Sciences,* vol. 37, no. 2, pp. 75-93, 2012/04/01 2012.

[5] G. Scheunert, O. Heinonen, R. Hardeman, A. Lapicki, M. Gubbins, and R. M. Bowman, "A review of high magnetic moment thin films for microscale and nanotechnology applications," *Applied Physics Reviews,* vol. 3, no. 1, p. 011301, 2016/03/01 2016.

[6] W. Liu, W. Zhong, and Y. W. Du, "Magnetic nanoparticles with core/shell structures," (in eng), *J Nanosci Nanotechnol,* vol. 8, no. 6, pp. 2781-92, Jun 2008.

[7] C. T. Black, C. B. Murray, R. L. Sandstrom, and S. Sun, "Spin-dependent tunneling in self-assembled cobalt-nanocrystal superlattices," (in eng), *Science,* vol. 290, no. 5494, pp. 1131-4, Nov 10 2000.

[8] J. Dugay *et al.*, "Room-Temperature Tunnel Magnetoresistance in Self-Assembled Chemically Synthesized Metallic Iron Nanoparticles," *Nano Letters,* vol. 11, no. 12, pp. 5128-5134, 2011/12/14 2011.

[9] R. P. Tan, J. Carrey, M. Respaud, C. Desvaux, P. Renaud, and B. Chaudret, "High-field and low-field magnetoresistances of CoFe nanoparticles elaborated by organometallic chemistry," *Journal of Applied Physics,* vol. 103, no. 7, p. 07F317, 2008/04/01 2008.

[10] A. J. Giustini, A. A. Petryk, S. M. Cassim, J. A. Tate, I. Baker, and P. J. Hoopes, "MAGNETIC NANOPARTICLE HYPERTHERMIA IN CANCER TREATMENT," *Nano LIFE,* vol. 1, no. 01n02, p. 10.1142/S1793984410000067, March-June 2010.

[11] M. Bañobre-López, A. Teijeiro, and J. Rivas, "Magnetic nanoparticle-based hyperthermia for cancer treatment," *Reports of Practical Oncology & Radiotherapy,* vol. 18, no. 6, pp. 397-400, 2013/11/01/ 2013.

[12] J. Estelrich, M. J. Sánchez-Martín, and M. A. Busquets, "Nanoparticles in magnetic resonance imaging: from simple to dual contrast agents," *International Journal of Nanomedicine,* vol. 10, pp. 1727-1741, 03/06 2015.

[13] C. Huang, K. G. Neoh, L. Wang, E.-T. Kang, and B. Shuter, "Magnetic nanoparticles for magnetic resonance imaging: modulation of macrophage uptake by controlled PEGylation of the surface coating," *Journal of Materials Chemistry,* 10.1039/C0JM01526A vol. 20, no. 39, pp. 8512-8520, 2010.

[14] T. A. P. Rocha-Santos, "Sensors and biosensors based on magnetic nanoparticles," *TrAC Trends in Analytical Chemistry,* vol. 62, pp. 28-36, 2014/11/01/ 2014.

[15] W. Wang, M. Yu, M. Batzill, J. He, U. Diebold, and J. Tang, "Enhanced tunneling magnetoresistance and high-spin polarization at room temperature in a polystyrene-coated ${\mathrm{Fe}}_{3}{\mathrm{O}}_{4}$ granular system," *Physical Review B,* vol. 73, no. 13, p. 134412, 04/11/ 2006.

[16] S. Wang, F. J. Yue, D. Wu, F. M. Zhang, W. Zhong, and Y. W. Du, "Enhanced magnetoresistance in self-assembled monolayer of oleic acid molecules on Fe3O4 nanoparticles," *Applied Physics Letters,* vol. 94, no. 1, p. 012507, 2009/01/05 2009.

[17] A. Mitra, B. Barick, J. Mohapatra, H. Sharma, S. S. Meena, and M. Aslam, "Large tunneling magnetoresistance in octahedral Fe3O4 nanoparticles," *AIP Advances,* vol. 6, no. 5, p. 055007, 2016/05/01 2016.

[18] C. Park, Y. Peng, J.-G. Zhu, D. E. Laughlin, and R. M. White, "Magnetoresistance of polycrystalline Fe3O4 films prepared by reactive sputtering at room temperature," *Journal of Applied Physics,* vol. 97, no. 10, p. 10C303, 2005/05/15 2005.

[19] T. B. Tran, I. S. Beloborodov, X. M. Lin, T. P. Bigioni, V. M. Vinokur, and H. M. Jaeger, "Multiple Cotunneling in Large Quantum Dot Arrays," *Physical Review Letters,* vol. 95, no. 7, p. 076806, 08/12/ 2005.

[20] T. B. Tran, I. S. Beloborodov, J. Hu, X. M. Lin, T. F. Rosenbaum, and H. M. Jaeger, "Sequential tunneling and inelastic cotunneling in nanoparticle arrays," *Physical Review B,* vol. 78, no. 7, p. 075437, 08/26/ 2008.

[21] S. Mitani, S. Takahashi, K. Takanashi, K. Yakushiji, S. Maekawa, and H. Fujimori, "Enhanced Magnetoresistance in Insulating Granular Systems: Evidence for Higher-Order Tunneling," *Physical Review Letters,* vol. 81, no. 13, pp. 2799-2802, 09/28/ 1998.

[22] A. L. E. a. B. I. Shklovskii, "Coulomb gap and low temperature conductivity of disordered systems," *Journal of Physics C: Solid State Physics,* vol. 8, no. 4, p. L49, 1975.

[23] M. Pauly *et al.*, "Co-tunneling enhancement of the electrical response of nanoparticle networks," (in eng), *Small,* vol. 8, no. 1, pp. 108-15, Jan 9 2012.

[24] H. Kumar *et al.*, "Role of Coulomb blockade and spin-flip scattering in tunneling magnetoresistance of FeCo-Si-O nanogranular films," *Journal of Applied Physics,* vol. 109, no. 7, p. 073914, 2011/04/01 2011.

[25] S. Shinji Miwa and Masashi Shiraishi and Masaki Mizuguchi and Teruya Shinjo and Yoshishige, "Spin-Dependent Transport in C 60 –Co Nano-Composites," *Japanese Journal of Applied Physics,* vol. 45, no. 7L, p. L717, 2006.

[26] H. Kusai, S. Miwa, M. Mizuguchi, T. Shinjo, Y. Suzuki, and M. Shiraishi, "Large magnetoresistance in rubrene-Co nano-composites," *Chemical Physics Letters,* vol. 448, no. 1, pp. 106-110, 2007/11/05/ 2007.

[27] R. P. Tan, J. Carrey, M. Respaud, C. Desvaux, P. Renaud, and B. Chaudret, "3000% high-field magnetoresistance in super-lattices of CoFe nanoparticles," *Journal of Magnetism and Magnetic Materials,* vol. 320, no. 6, pp. L55-L59, 2008/03/01/ 2008.

[28] J. Yuan, C.-F. Li, Z.-Q. Liu, D. Wu, and L. Cao, "Synthesis of variously shaped magnetic FeCo nanoparticles and the growth mechanism of FeCo nanocubes," *CrystEngComm,* 10.1039/C7CE01353A vol. 19, no. 43, pp. 6506-6515, 2017.

[29] C. Garnero, "Synthèse organométallique de nanoparticules de FeCo pour l'intégration sur inductance," 2016.

[30] R. P. Tan *et al.*, "Magnetoresistance and collective Coulomb blockade in superlattices of ferromagnetic CoFe nanoparticles," *Physical Review B,* vol. 79, no. 17, p. 174428, 05/21/ 2009.

[31] A. Rotaru *et al.*, "Nano-electromanipulation of Spin Crossover Nanorods: Towards Switchable Nanoelectronic Devices," *Advanced Materials,* vol. 25, no. 12, pp. 1745-1749, 2013.

[32] A. Vijayaraghavan *et al.*, "Ultra-Large-Scale Directed Assembly of Single-Walled Carbon Nanotube Devices," *Nano Letters,* vol. 7, no. 6, pp. 1556-1560, 2007/06/01 2007.

[33] R. Krupke, F. Hennrich, H. B. Weber, M. M. Kappes, and H. v. Löhneysen, "Simultaneous Deposition of Metallic Bundles of Single-walled Carbon Nanotubes Using Ac-dielectrophoresis," *Nano Letters,* vol. 3, no. 8, pp. 1019-1023, 2003/08/01 2003.

[34] S. B. Asokan, L. Jawerth, R. L. Carroll, R. E. Cheney, S. Washburn, and R. Superfine, "Two-Dimensional Manipulation and Orientation of Actin−Myosin Systems with Dielectrophoresis," *Nano Letters,* vol. 3, no. 4, pp. 431-437, 2003/04/01 2003.

[35] C. Duan *et al.*, "Controllability of the Coulomb charging energy in close-packed nanoparticle arrays," *Nanoscale,* 10.1039/C3NR02334F vol. 5, no. 21, pp. 10258-10266, 2013.

[36] Y. Wang, C. Duan, L. Peng, and J. Liao, "Dimensionality-dependent charge transport in close-packed nanoparticle arrays: from 2D to 3D," *Scientific Reports,* Article vol. 4, p. 7565, 12/19/online 2014.

[37] A. Zabet-Khosousi, Y. Suganuma, K. Lopata, P.-E. Trudeau, A.-A. Dhirani, and B. Statt, "Influence of Linker Molecules on Charge Transport through Self-Assembled Single-Nanoparticle Devices," *Physical Review Letters,* vol. 94, no. 9, p. 096801, 03/09/ 2005.

[38] A. J. Quinn *et al.*, "Manipulating the Charging Energy of Nanocrystal Arrays," *Small,* vol. 1, no. 6, pp. 613-618, 2005.

[39] J. Dugay *et al.*, "Charge transport and interdot coupling tuned by the tunnel barrier length in assemblies of nanoparticles surrounded by organic ligands," *Physical Review B,* vol. 89, no. 4, p. 041406, 01/23/ 2014.

[40] M. Manheller, S. Karthäuser, R. Waser, K. Blech, and U. Simon, "Electrical Transport through Single Nanoparticles and Nanoparticle Arrays," *The Journal of Physical Chemistry C,* vol. 116, no. 39, pp. 20657-20665, 2012/10/04 2012.

[41] M. A. Osborne and A. A. E. Fisher, "Charge-tunnelling and self-trapping: common origins for blinking, grey-state emission and photoluminescence enhancement in semiconductor quantum dots," *Nanoscale,* 10.1039/C6NR00529B vol. 8, no. 17, pp. 9272-9283, 2016.

[42] J.-F. Dayen *et al.*, "Enhancing the Molecular Signature in Molecule-Nanoparticle Networks Via Inelastic Cotunneling," *Advanced Materials,* vol. 25, no. 3, pp. 400-404, 2013.

[43] T. Zhu and Y. J. Wang, "Enhanced tunneling magnetoresistance of ${\mathrm{F}\mathrm{e}\ensuremath{-}\mathrm{A}\mathrm{l}}_{2}{\mathrm{O}}_{3}$ granular films in the Coulomb blockade regime," *Physical Review B,* vol. 60, no. 17, pp. 11918-11921, 11/01/ 1999.

[44] J. S. Moodera, J. Nowak, and R. J. M. van de Veerdonk, "Interface Magnetism and Spin Wave Scattering in Ferromagnet-Insulator-Ferromagnet Tunnel Junctions," *Physical Review Letters,* vol. 80, no. 13, pp. 2941-2944, 03/30/ 1998.

[45] R. P. Tan, J. Carrey, and M. Respaud, "Voltage and temperature dependence of high-field magnetoresistance in arrays of magnetic nanoparticles," *Journal of Applied Physics,* vol. 104, no. 2, p. 023908, 2008/07/15 2008.

Chapter 4: Spin-transition in Fe (II) complex and in Pt nanoparticle – Fe(II) complex hybrid nanostructures

4.1 Introduction

In chapter 1.3, we discussed the phenomenon of spin-transition in Fe (II) complexes, and its influence on charge transport properties. The high spin ↔ low spin transition in these complexes can impart a switching behavior to the conductivity of their assemblies [1, 2]. Such a behavior can be exploited for their applications in wide range of devices [3, 4]. However, despite this advantageous quality, there exists a room for improvement in certain physical properties of these complexes. For example, spin cross-over (SCO) complexes display very low conductivity, which make their integration in useful devices difficult. One possible way to improve their conductivity could be the elaboration of hybrid structures containing both metal nanoparticles and SCO complex. Hypothetically, the conductivity of such hybrid structure could have: (a) higher values due to the presence of metallic nanoparticles, and (b) switching behavior related to the SCO complex. Moreover, it could be possible that the presence of Coulomb blockade in the assembly could enhance the difference of conductivity between the high- and the low-spin state, similar to what is observed for the TMR amplitude in assemblies of magnetic nanoparticles.

Experimental studies on the mentioned hybrid structures are lacking and several important questions need to be addressed before approving such a hypothesis. The first and foremost question that needs to be asked is “Could the spin transition in SCO complexes be preserved in the presence of nanoparticles?” Presence of an external entity can change the electric environment of the complex in addition to the cooperativity, which in turn can affect the process of spin transition. Thus, the spin transition in the hybrid nanostructures cannot be taken for granted, unless verified experimentally. If the spin transition in such hybrid structures persists, then the second relevant question to ask would be “Is it possible to observe spin-transition’s signature in charge transport properties?” It is true that in assemblies of some SCO complexes spin transition could manifest itself in the form of conductivity switching, however, in such cases current flows essentially through the SCO complex. Thus, any physical change, such as change in the size of the molecule, which may occur during the transition, would directly influence the charge transport properties. In case of hybrid structures, presence of metal nanoparticles may offer a low resistive path due to which current may not flow through the SCO complex. Consequently, there is a possibility that spin transition may not manifest itself in the form of conductivity switching. In order to answer these questions, experimental studies are necessary to perform. So far, to our knowledge, only one study has been realized in assemblies of nanostructure SCO complex and metal nanoparticles hybrid structure, where the spin transition effect has been observed in charge transport properties in the form of a shallow minimum in resistance as a function of temperature [5]. Further studies need to be performed in similar systems with different metal nanoparticles and SCO complexes to look for abrupt switching or hysteresis in the conductivity as a function of temperature,

During the course of this thesis, we have studied spin-transition in: (a) [Fe(oTs)$_2$.6 H$_2$0]Y (where oTs = paratoluene sulfonate, and Y = (1E)-1-(thiophen-3-yl)-N-(4H-1,2,4-triazol-4-yl)ethan-1-imine) complex, and (b) hybrid structure of the mentioned complex and platinum nanoparticles. From now onwards, the mentioned Fe (II) complex without Pt particles shall be referred as “coordination network” and in the presence of Pt particles as “hybrid network”. We have performed charge transport in assemblies of both types of networks. Any changes occurring in charge transport properties alone cannot be attributed to spin transition, and thus needs to be supported by other studies. Therefore, we have performed magnetic measurements in both types of networks to support charge transport measurements. In this chapter, we shall present these studies. We shall begin by briefly summarizing the synthesis of these networks followed by their characterization. Then, we shall present the magnetic measurements and charge transport studies before finally concluding on our results.

The synthesis of the coordination and hybrid network could be developed due to the collaborative efforts of two chemistry teams at the LPCNO and LCC. The chemical preparation of these structures was carried out at LPCNO by Dr. Simon Tricard, Angélique Gillet and Mathilde Rigoulet of “Nanostructures and organometallic chemistry” group and by Dr. Lionel Salmon of LCC from the “Equipe P”. A typical synthesis procedure includes the synthesis of Pt particles, the synthesis of coordination network, and the mixing of two solutions to obtain a hybrid network. A brief summary of the synthesis procedure is presented in the next section.

4.2 Synthesis procedure

Synthesis of Pt particles: For the synthesis of Pt nanoparticles, a procedure similar to the one described in chapter 2 was used. Briefly, a solution of Pt$_2$(dba)$_3$ (90 mg; 0.165 mmol of Pt) in 20 mL of freshly distilled and deoxygenated THF was pressurized in a Fischer-Porter bottle with 1 bar of CO during 30 minutes at room temperature under vigorous stirring. During this time, the solution color changed from violet to brown (attesting the formation of the nanoparticles). The mixture was evaporated and washed with pentane to eliminate the dba (3 x 20 mL), and to obtain native nanoparticles. The colloid was then re-dissolved in 20 mL of THF.

Synthesis of coordination network: All solutions were prepared in THF. 2 mL of a solution of Fe(oTs)$_2$.6 H$_2$0 (oTs = paratoluene sulfonate) was added in 2 mL of a solution of the ligand Y (Y = (1E)-1-(thiophen-3-yl)-N-(4H-1,2,4-triazol-4-yl)ethan-1-imine). The precursor’s concentrations were adapted to obtain 3 eq. of the Y ligand per Fe. The solution was agitated for 2 hours. Then, the solution was either evaporated to dryness and isolated as pale white powder

(powder form) or partly evaporated to a light yellow-gel (gel form). Figure 4.1 (a) and (b) shows the structural formula of precursors whereas 4.1(c) shows the structure of the coordination network.

Synthesis of the hybrid network: All solutions were prepared in THF. 2 mL of a solution of $Fe(oTs)_2.6\ H_20$ (oTs = paratoluene sulfonate) and 2 mL of a solution of the Y ligand were simultaneously added to 4 mL of the platinum nanoparticle mixture. The precursor's concentrations were adapted to obtain 0.2 eq. of ligand and 0.06 eq. of Fe per introduced Pt. The brown solution was agitated for 2 hours. Drops of the crude solution were deposited on specific substrates for characterization (drop-cast state). The solution was either evaporated to dryness and isolated as dark-brown powder (powder form) or partly evaporated (gel form).

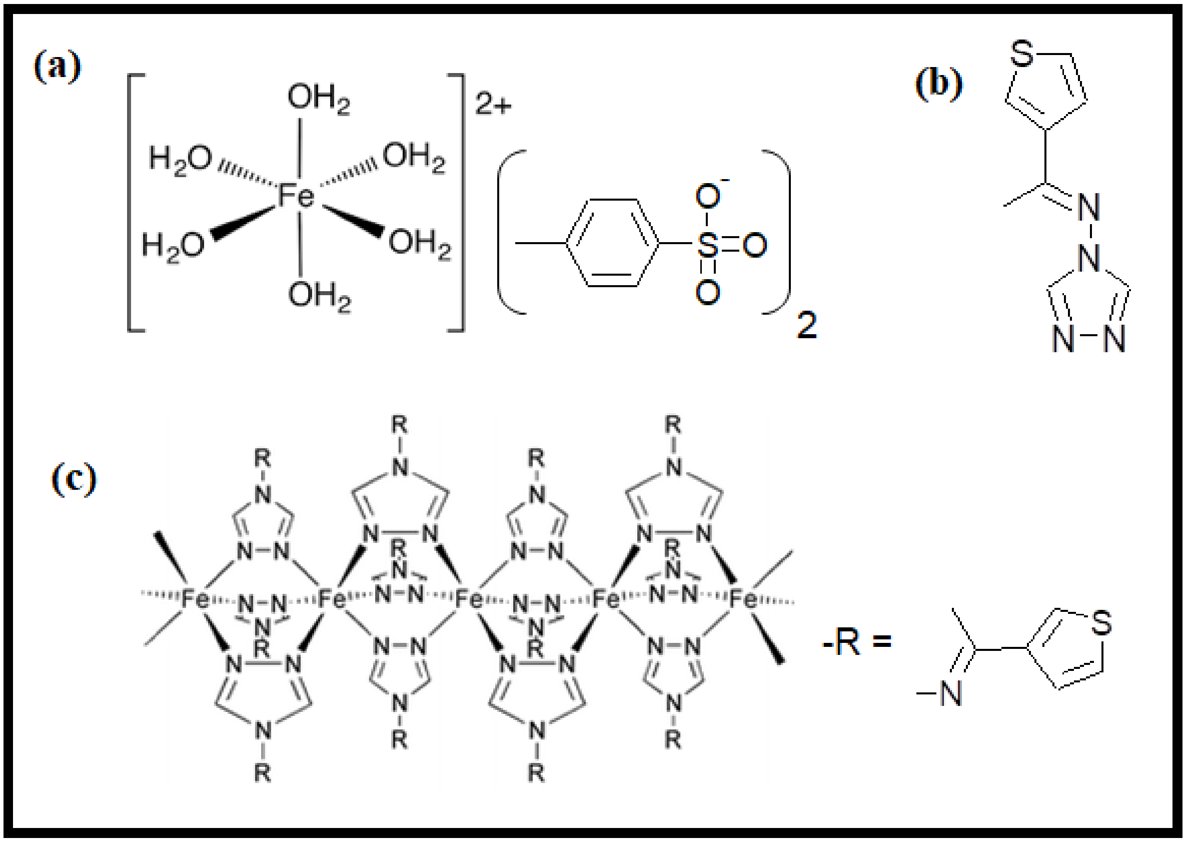

Figure 4.1: Structural formula of (a) Fe (II) precursor, (b) ligand Y and (c) coordination network.

4.3 Characterization

TEM images of the Pt particles and of the hybrid networks were taken after depositing a drop of their solutions on TEM grids. Well dispersed platinum particles showed a mean diameter of 1.1 nm ± 0.3 nm. In accordance with our previous studies, we did not observe any kind of auto-organization formed by platinum particles as evident from the TEM image shown in Figure 4.2 (a). For hybrid network, in certain regions, an auto-organization of the particles in the form of parallel chain like structures could be observed. However, certain regions without any organization of the particles could also be found. In Figure 4.2 (b) the light grey areas marked by yellow arrows show some of the regions where the particles are found to be auto-organized. Figure 4.2 (c) shows the zoomed view of one such area. On further zooming, particles arranged in the chain like structures can be seen [Figure 4.2 (d)]. We hypothesize that such an organization of the particles could be due to their interaction with the coordination network. However, such organization was only observed for the prepared samples where the 0.2 eq, of Y and 0.06 eq. of Fe were added per Pt. For the samples, where the higher concentration of the Fe and Y were used (0.4 eq. of X and 0.12 eq. of Fe (II)), no or little organization was observed.

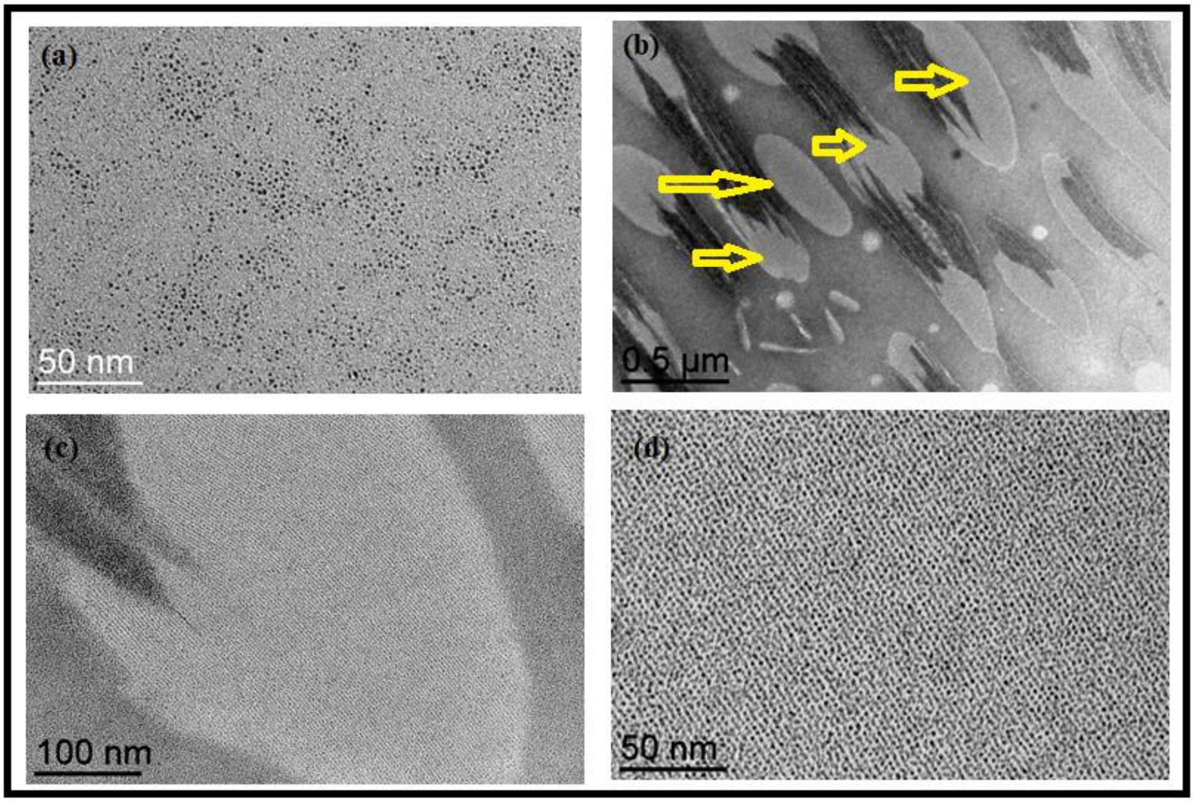

Figure 4.2: TEM images showing of (a) well dispersed platinum nanoparticles, and (b) hybrid network showing the regions where the organization of particles take place. (c) and (d) show the zoomed view of the assembly showing the particles arranged in chain like structures.

4.4 Thermal induced transition in coordination network

(a) Change in color

In most Fe (II) complexes, spin transition can be induced thermally. This holds true for the coordination network used in our study as well. The preliminary detection of thermal induced transition in coordination network could be performed by observing the thermochromism (i.e. change in color with temperature). Thermochromism is a typical feature of SCO complexes and can be observed in nearly all Fe (II) complexes. We observed that the coordination network used in our study shows a pale white color at room temperature but becomes violet at low temperature. Figure 4.3 shows the coordination network in vibrating sample magnetometer (VSM) capsules kept at room-temperature (pale white color) and cooled with liquid nitrogen (violet color). As the low spin state is expected at low temperature, we attribute the violet color to the low spin state, and the pale white color to the high spin state.

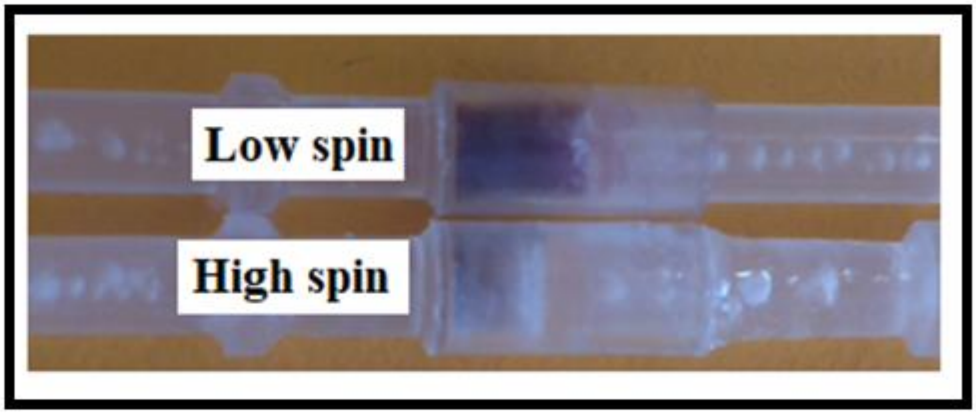

Figure 4.3: Gel form of the coordination networks in VSM capsules showing the pale white color for the capsule kept at room-temperature (high spin state), and violet color for the capsule cooled with liquid nitrogen (low spin state).

Although the presence of thermochromism indicates that the spin transition may exhibit in the coordination network, it does not provide any quantitative information about the profile of transition such as transition temperature, presence or absence of a hysteresis, extent of transition (i.e. complete or partial) etc. In order to obtain further information on these aspects, we chose to study the magnetic behavior of the complex as a function of temperature. Magnetic studies are presented in the subsequent section.

(b) Magnetic detection of spin-transition

We used vibrating sample magnetometer to study the variation in magnetic moment of the complex as a function of temperature at a constant magnetic field. During a transition from high spin to low spin state, Fe (II) in the SCO complexes changes from a paramagnetic state (with four unpaired electron) to a diamagnetic state (with zero unpaired electron). Such a change directly affects the magnetic moment of the SCO complexes. Thus, magnetic measurements can act as a direct evidence of spin-transition in a complex (if any), and can be used to support its manifestation in charge transport studies.

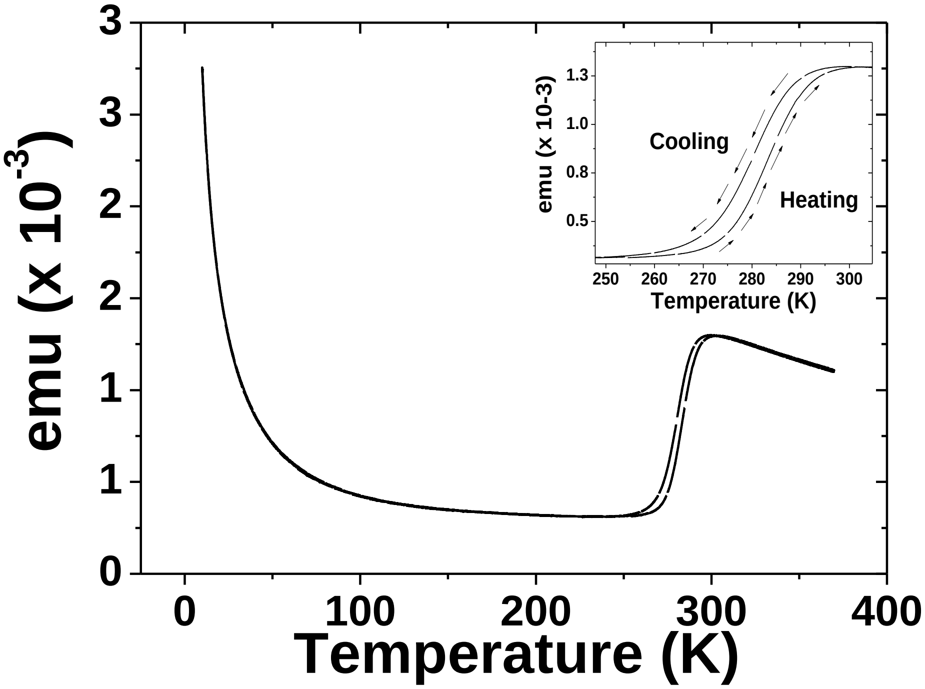

Figure 4.4: Magnetic moment of the coordination network in the gel form showing a decrease in magnetic moment in the temperature range of 300 K to 280 K. Inset shows the hysteresis observed during the thermal cycle.

Magnetic measurements were performed at 1.5 T while sweeping the temperature cycles from 370 K →10 K → 370 K at the rate of 1 K per minute. The sweeping rate of temperature and the field values would remain the same for future magnetic measurements as well. For the complex in gel form, a decrease in magnetic moment was observed while decreasing the temperature from 300 K to 280 K, as shown in Figure 4.4. During the heating cycles, magnetic moment increased in the mentioned range of temperature with a small hysteresis of ~ 4 K, as shown in the inset of Figure 4.4. These observations confirmed the presence of spin-transition in the coordination network.

Although the decrease in magnetic moment indicates the presence of spin-transition, it does not provide any information on its extent. A more informative and customary way of analyzing the spin transition is to plot the product of molar susceptibility (χ_m) and temperature against temperature. When a magnetic moment has a purely paramagnetic behavior and follows a Curie-law, this product is a constant. In Fe (II) complexes, as the number of unpaired electrons change from 4 to 0 during a high-spin to low-spin transition, the value of $\chi_m T$ drops down. It decreases from 3 to zero if the whole population of Fe (II) undergo transition from high spin to low spin state. This can provide information regarding the extent of transition. Thus, from here onwards, we shall present our magnetic measurements in the form of $\chi_m T$ plots except for the magnetic measurements performed on the drop casted assemblies on Si/SiO_2 surface, where the strong diamagnetic signal from the substrate could not be subtracted from the data.

After observing the spin-transition the first time the sample was measured, we performed several thermal cycles on the same coordination network sample to verify the reproducibility of the spin-transition. Three consecutive thermal cycles performed on the coordination network in gel form are shown in Figure 4.5. During the first cycle, the $\chi_m T$ value decreased from ~ 3 cm^3 K mol^{-1} (at 300 K) to ~ 0.5 cm^3 K mol^{-1} (at 260 K) indicating a nearly complete spin transition in this regime. Only a small decrease was observed in $\chi_m T$ values from 260 K to 10 K. Surprisingly, during the second cycle, the $\chi_m T$ value decreased from ~3 to ~1.7 cm^3 K mol^{-1} between 300 K and 260 K. On further decreasing the temperature, the $\chi_m T$ value decreased gradually and reached close to 0.5 cm^3 K mol^{-1} at 10 K as shown in Figure 4.5. This indicates that the spin-transition during second cycle was partially rapid (from 300 K to 260 K) and partially gradual (below 260 K). Similar behavior was observed during the third cycle.

Although unexpected, such evolution of spin transition required investigation to find its cause. Two observations helped us to find the source of such evolutionary behavior of spin transition. First, the physical state of the sample changed after the measurement. Initially prepared sample showed a sticky gel like structure. However, after performing the magnetic measurements, the form of the sample was similar to that of a powder which was not sticky in nature. Second, the mass of the sample decreased roughly by 8% after the measurements. We interpret these observations in terms of quantity of solvent present in the sample. The initial sticky nature of the complex could be due to the presence of THF in the sample, which was used as a solvent during the reaction. During the magnetic measurements, THF might have escaped out slowly from the sample and from the capsule, leaving behind the coordination network in powder form. Later, it was indeed verified that the VSM capsule in which samples are enclosed for magnetic measurements permit the slow escaping of solvent or vapors, confirming this hypothesis.

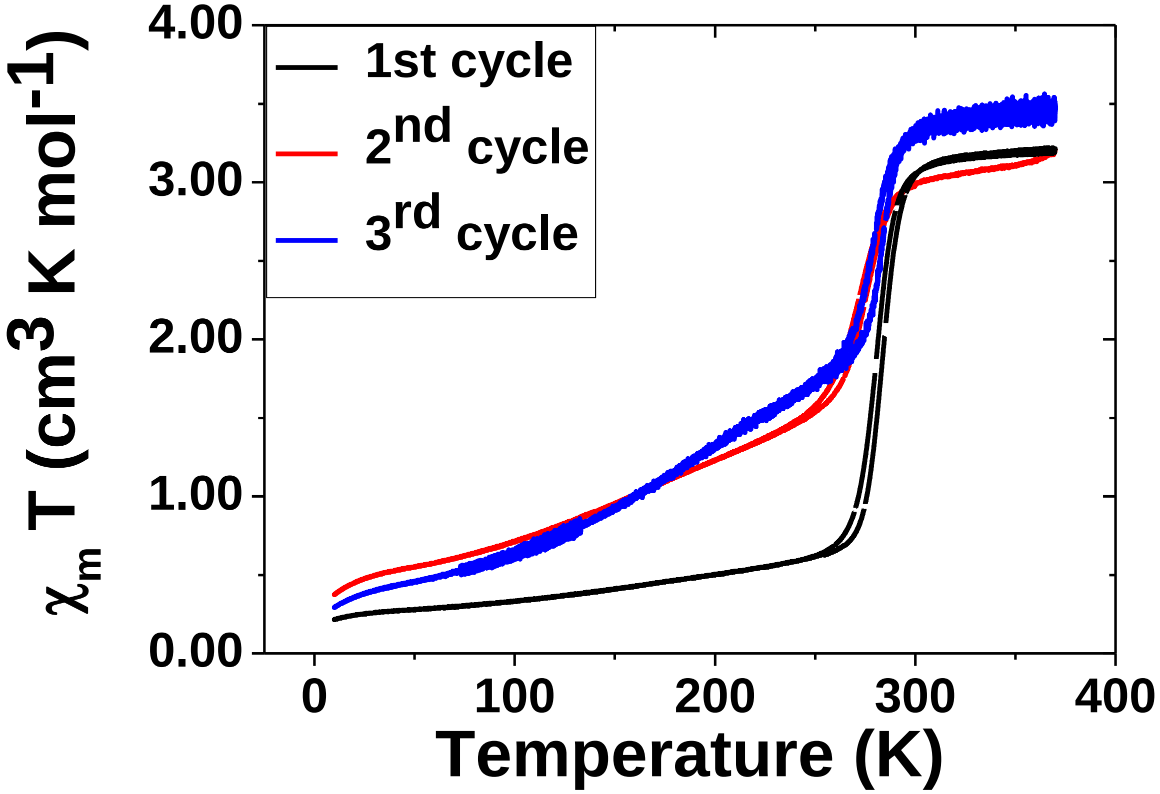

Figure 4.5: Three consecutive thermal cycles showing the evolution of spin transition in the coordination network in gel form. The first cycle show relatively rapid transition whereas the subsequent cycles show partially rapid and partially gradual transition.

(c) Role of solvent

To further confirm that the evolution in spin transition raised due to the escape of solvent during the measurement, we performed further magnetic measurements on the coordination network. This time, we chose to prepare the sample in two states. In the first state, sufficient amount of solvent was left in the sample so that it remained in the form of gel for longer period of time. This would permit us to perform successive thermal cycles while evaporating the solvent at certain intervals. In the second state, the coordination network was left to dry for longer period of time until its sticky nature disappeared completely and the sample appeared to be in powder form.

For the sample in the gel form, several thermal cycles were performed. First two cycles were performed consecutively to observe the effect of slowly escaping solvent from the samples. For some of the subsequent cycles, for a faster evaporation of solvent, sample was taken out of VSM and left opened in air before starting the next cycle. We shall mention before each cycle, if the sample was taken out for drying. The followed procedure and the observations made during these magnetic measurements are summarized below; thermal cycles are shown in Figure 4.6.

Cycle 1: In the gel form, coordination network was subjected to first thermal cycle during which a decrease in $\chi_m T$ from 2.2 to 0.7 cm^3 K mol^{-1} was observed while decreasing the temperature from 300 K to 200 K. At lower temperatures, $\chi_m T$ value remained constant.

Cycle 2: During the successively performed second thermal cycle, the value of $\chi_m T$ decreased from 2.2 to 0.5 cm^3 K mol^{-1} from 300 K to 200 K, indicating a slight increase in rapidity and extent of transition.

Before performing the third thermal cycle, the VSM capsule was taken out and left open in air for the solvent to evaporate. After 15 minutes, roughly 18% of the initial mass of the sample was lost due to the evaporation of solvent. The sample was then subjected to magnetic measurements once again for the third thermal cycle.

Cycle 3: This time, a much rapid transition was observed with a larger fraction of spin population transiting to low spin state compared to cycle 1 and 2. This was indicated by the decrease in $\chi_m T$ values from 2.2 to close to zero while decreasing the temperature from 300 K to 250 K.

Cycle 4: Fourth cycle performed right after the third (without extracting the sample) showed a behavior similar to cycle 3.

Before 5th cycle, sample was taken out again and left open to dry. The rate of evaporation of solvent became slower as the quantity of the solvent decreased in the sample. This was indicated by slow decrease in mass of the sample. To increase the evaporation rate, the sample was kept at 330 K for 30 minutes until the mass of the sample was reduced by 30% compared to the initial mass (at the beginning of the first cycle).

Cycle 5: Surprisingly, at the beginning of the fifth cycle at 300 K, we observed that $\chi_m T$ value was 0.7 cm^3 K mol^{-1} which was much lower compared to the $\chi_m T$ value observed in previous cycles at 300 K. One possible explanation of such low $\chi_m T$ value could be that most population of Fe (II) in the complex was somehow present in low-spin state at 300 K. In order to verify this, the temperature was increased to 330 K before performing the fifth thermal cycle. As the temperature increased, $\chi_m T$ value increased as well, and attained a value of 2.5 at 330 K. On performing the fifth cycle, the $\chi_m T$ value decreased quite gradually from 2.5 (at 330 K) to 0.5 (at 150 K).

Cycle 6: During the sixth cycle, the observed transition was similar to the one observed in cycle 5, although maybe more gradual.

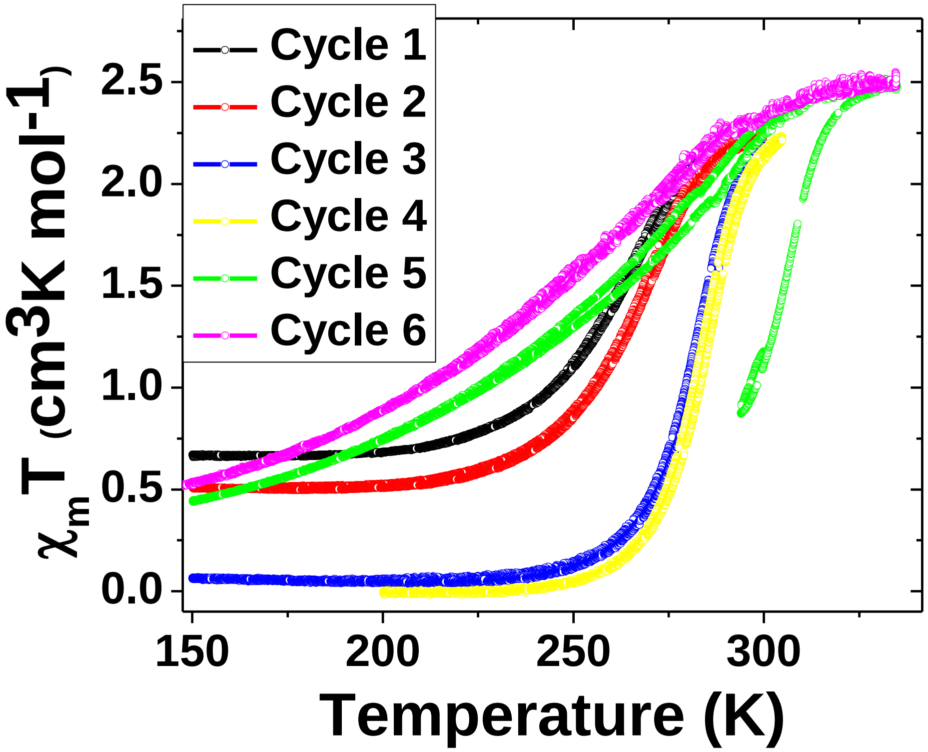

Figure 4.6: Thermal cycles showing the evolution in spin transition as the quantity of the solvent in the sample evolved.

Before drawing any conclusion from these thermal cycles, we would first like to comment on the value of $\chi_m T$ observed in the experiments. The value of $\chi_m T$ observed in the thermal cycles was observed in the range of 2.3 to 2.6 which is slightly lower than the expected value of 3. The lower value of $\chi_m T$ could arise due to two reasons. First reason could be an error in the estimation of Fe (II) quantity present in the sample. Numbers of moles of Fe (II) present in the complex were estimated by using the envisaged molecular formula of the complex and mass of the sample after letting it dry for 4-5 days. Traces of solvent trapped in the sample may cause an error in the estimation of number of moles of Fe (II) in the complex. However, such an error would result in an underestimation of Fe (II) moles, and so an overestimation of the $\chi_m T$ value. Second possible reason could be the partial fraction of the Fe (II) population present in the low-spin state. The observed $\chi_m T$ value could be lower than 3 in cases where certain fraction of population is present in the low spin state as well. This could be possible scenario observed in our case.

Thermal cycles shown in the Figure 4.6 provide information on the influence of solvent on spin transition. In the presence of high quantity of solvent, a gradual and incomplete transition occurs as observed in cycle 1. As the solvent slowly evaporates (during the measurement), the transition becomes slightly more rapid with more fraction of population transiting to low spin state as observed in cycle 2. As significant amount of solvent is evaporated (roughly 18% by opening the VSM capsule), transition becomes significantly faster and reached almost towards completion as observed in cycle 3. Successively performed fourth cycle showed yet again slightly faster transition which again could have come from small quantity of solvent evaporating during the measurement. Till this point, reduction in solvent quantity caused the transition to become more rapid and complete. However, further drying resulted back in gradual and incomplete transition as observed in fifth and subsequent cycle.

Finally, magnetic measurements were performed on the second sample which was left to dry until it appeared to be in powder form. As shown in Figure 4.7, $\chi_m T$ value for this sample did not show any significant changes in the temperature regime where transition was expected. Absence of transition in this sample further confirmed that solvent played an important role in determining the transition behavior of the complex.

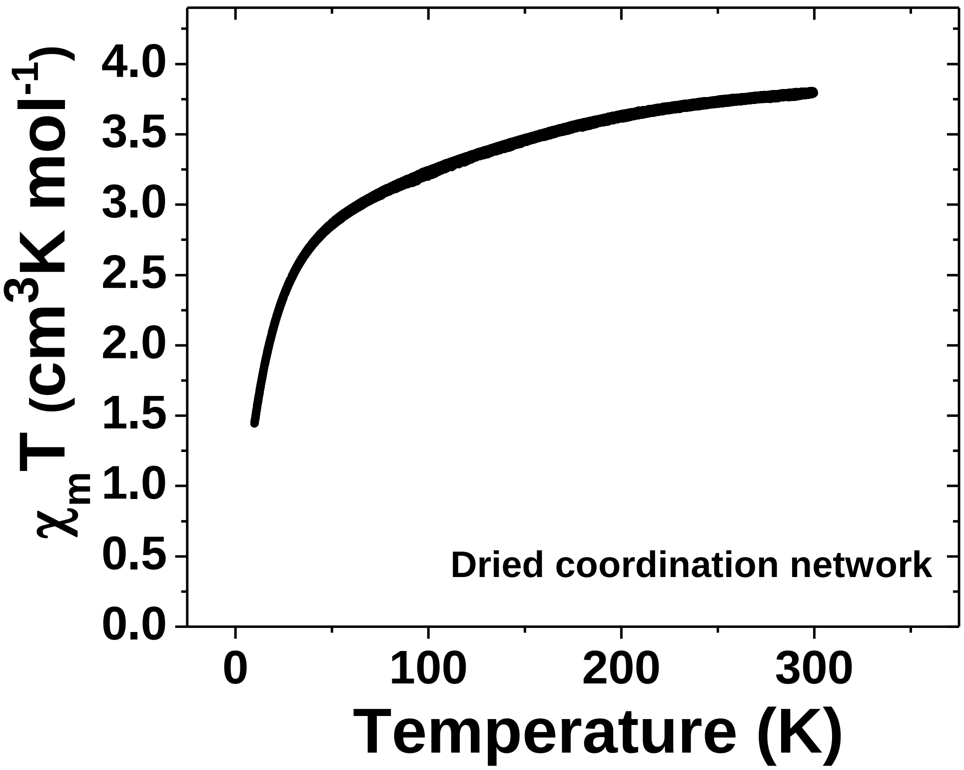

Figure 4.7: Magnetic measurements on a dried coordination network showing the absence of spin transition.

These observations indicate that an optimum quantity of solvent should be present in the sample in order to observe a rapid and complete spin transition. Higher quantity of solvent results in gradual and incomplete transition while absence of solvent would cause a complete disappearance of spin transition. In the studied sample, the rapid transition observed in cycle 3 was observed when the mass of the solvent present in the sample was roughly 12% of the whole sample mass. This value, however, cannot be generalized as the initial amount of solvent present would vary from sample to sample.

4.5 Spin transition in hybrid networks

Thermal induced spin transition was also studied in hybrid networks. The presence of platinum nanoparticle in hybrid network make them appear black-brown in color, which restricted us from verifying the thermochromism. However, magnetic measurements could still be performed. In order to verify if similar solvent dependency exhibits in hybrid networks, we prepared the sample in gel and dried form. Figure 4.8 shows the magnetic measurement performed on dried hybrid networks. As expected, no sign of spin transition was observed in the dried form as indicated by the constant value of $\chi_m T$ over a wide range of temperature.

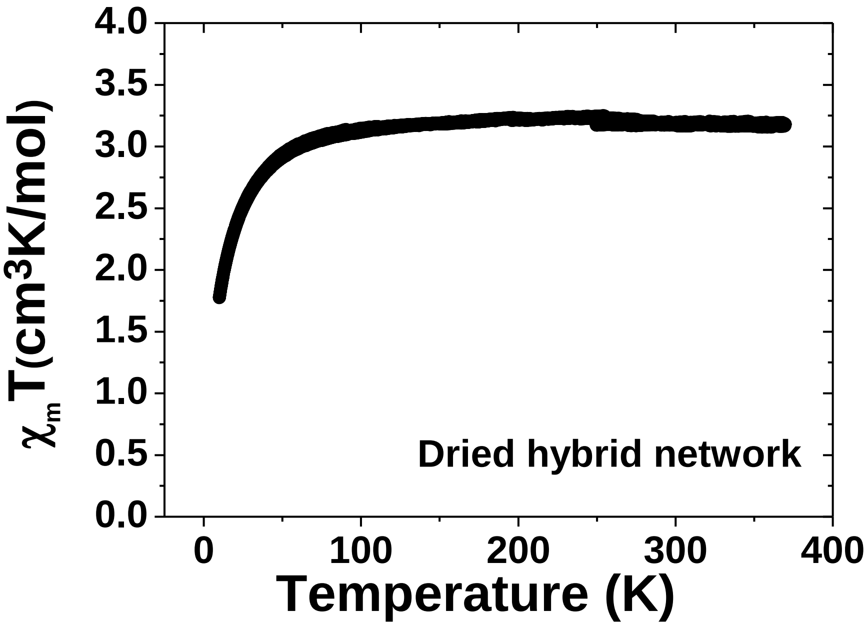

Figure 4.8: Magnetic measurement performed on the dried hybrid network showing a constant $\chi_m T$ value in the range of temperature (300 K to 100 K), which indicates the absence of spin-transition in this temperature regime.

In the gel form of hybrid network, magnetic measurements were performed on several samples. Similarly to coordination networks, several thermal cycles were performed successively, as shown in Figure 4.9. During the first cycle, $\chi_m T$ value decreased from 2.5 (at 300 K) to 2.2 (at 150 K), which was also observed during the second cycle. This suggests that only a small fraction, if any, of the spin population undergo a transition, while a large fraction remained blocked in high spin state. Such an incomplete and gradual transition could arise from two possible sources. First possible reason could be the presence of platinum nanoparticles, which might have blocked the spin-transition. Second reason could be the quantity of solvent which might be not present in optimum quantity. As observed in case of coordination network, extra amount of solvent could result in partial and gradual transition. To verify if this could be the case in the gel form of hybrid network, we increased the sample temperature up to 370 K during which the value of $\chi_m T$ increased up to 2.7 cm^3 K mol^{-1}. This indicates that some of the population was already present in low spin state which transit to high spin state on heating. The next two thermal cycles (fourth and fifth) showed a gradual decrease in $\chi_m T$ value from 2.7 cm^3 K mol^{-1} at 300 K to 0.6 cm^3 K mol^{-1}at 50 K, which indicates a nearly complete but gradual transition. To verify if the quantity of the solvent could be further optimized, the VSM capsule was opened and heated for 10 minutes at 370 K before performing the fifth thermal cycle. The $\chi_m T$ value observed in fifth cycle remained close to 3 and did not show any significant variation with temperature indicating the absence of transition. These measurements suggest that the solvent dependency of transition existed in the gel form of hybrid networks as well. Heating of the sample after the 2nd cycle might have optimized the quantity of solvent present in the sample so the transition could be observed. However, further heating performed before fifth cycle might have caused reduction in the solvent quantity below the optimum required for spin transition.

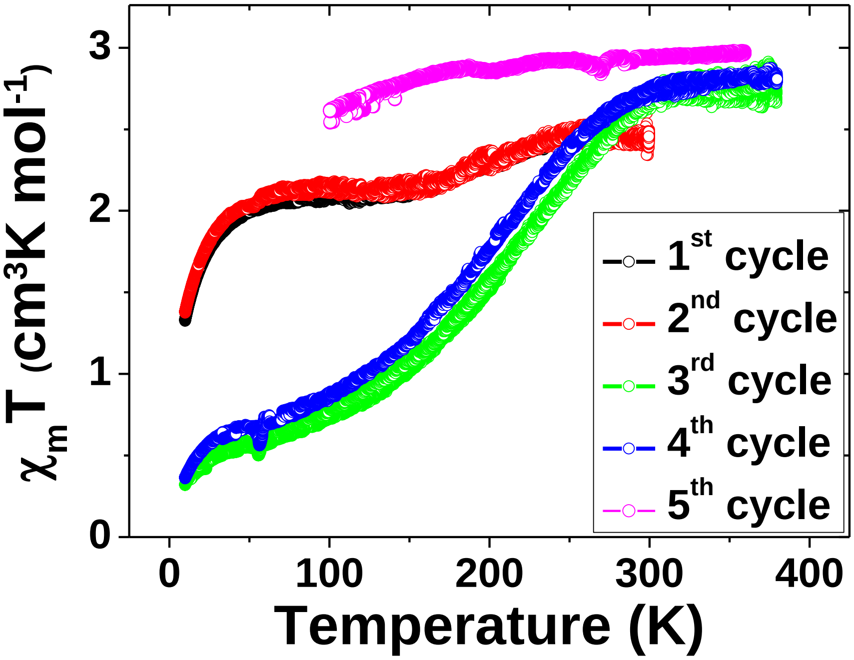

Figure 4.9: Magnetic measurements performed on the hybrid network in the form of gel showing the evolution of spin transition for different cycles.

Controlling the quantity of solvent in the sample remained a delicate task as high quantities of solvent resulted in partial and gradual transition whereas low quantity of solvent resulted in its disappearance. The fact that we could not observe in this sample an abrupt and hysteretic transition as the one observed in coordination networks can be attributed to either the presence of particles or due to the non-optimal quantity of the solvent in the sample.

Although a complete, abrupt and hysteretic transition was not observed in any of the studied sample, we could still observe an *incomplete*, abrupt and hysteretic transition in one of the sample, as shown in Figure 4.10. In this sample, $\chi_m T$ value decreased from 3 to 1.6 while decreasing the temperature from 300 K to 250 K. Further decreasing the temperature had no significant effect on $\chi_m T$ value. However, after heating the sample up to 370 K, the transition disappeared in the second thermal cycle, probably due to the evaporation of solvent. Besides, fluctuations in the magnetic moment could also be observed, the reason of which is not known.

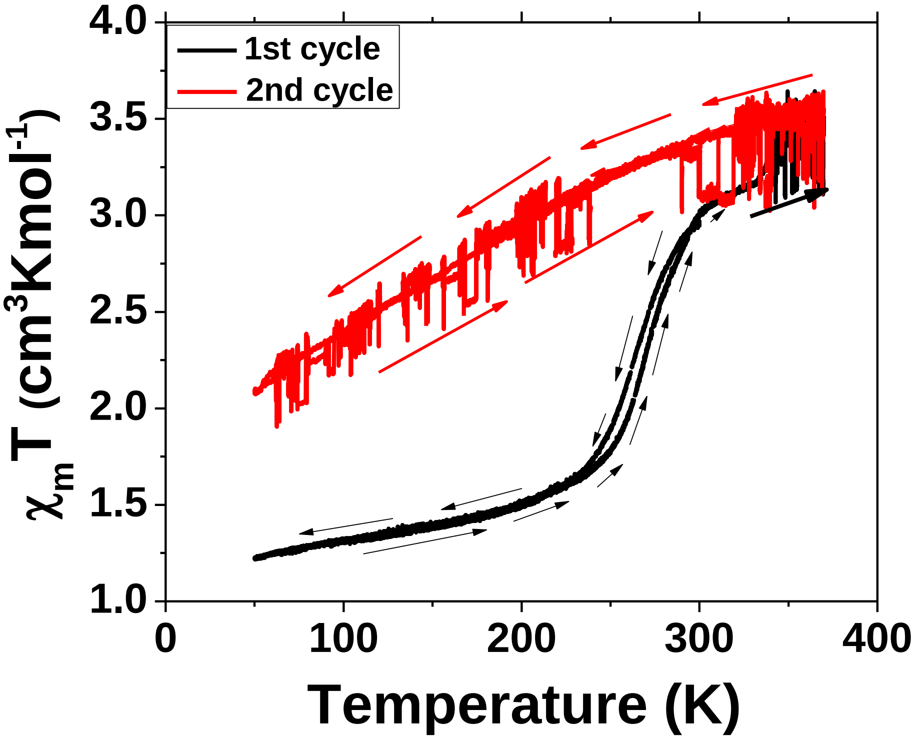

Figure 4.10: Magnetic measurement performed on an hybrid network sample in the gel form showing a partial and rapid transition during first cycle, which disappeared in the second cycle performed, after heating the sampled to 370 K.

4.6 Magnetic measurements on assemblies deposited on substrates

Magnetic measurements presented until now were performed either on dried powder form or gel form of the sample. Similar measurements were also performed on drop casted assemblies of coordination and hybrid networks deposited on a Si/SiO$_2$ surface. Such measurements were required in order to verify that the transition is not blocked by any kind of interaction with the surface. Since charge transport measurement, as we shall see in later sections, are performed on assemblies deposited on substrates, this is necessary to make sure that the transition persists in such samples. For this, few tens of drops (20 to 40) of hybrid and coordination network's solution were deposited on Si/SiO$_2$ substrates in order to have detectable amplitude of magnetic moment. In this case, the estimation of Fe (II) present on the surface could not be performed, thus, magnetic measurement non-normalized by the sample weight will be presented. Results are shown Figure 4.11.

In the case of coordination networks, a decrease in magnetic moment was observed in the range of 300 K to 250 K while decreasing the temperature during the first thermal cycle. On increasing the temperature, magnetic moment increased with a hysteresis of 30 K [see figure 4.11(a)]. The negative value of magnetic moment is due to the diamagnetic signal coming from the substrate; however, it did not restrict us from observing the quantity of interest, i.e. the transition in the assembly of coordination networks. During the second cycle, the hysteresis disappeared while the magnetic moment showed a maxima around 300 K. The disappearance of the transition could be due to solvent effects. However, in the case of assemblies deposited on substrates, the presence of solvent cannot be observed with naked eye. However, certain amount of solvent may remain trapped between the particles. This is often observed in the form of an increase in the pressure inside the VSM chamber when the assemblies are heated slightly above room-temperature. Besides, it takes relatively longer time for vacuum to establish when the assemblies are put in the vacuum chambers of different instruments such as SEM or sputtering, compared to a naked substrate without assemblies.

To measure assemblies of hybrid networks, the diamagnetic signal of the substrate was clearly an issue since the deposited drops contained a very small amount of Fe(II). To obtain an improved signal, we drop casted assemblies of hybrid networks inside VSM capsules whose diamagnetic signal has been previously measured. Figure 4.11(b) shows the magnetic moment of the hybrid assembly deposited inside the VSM capsule after removing the signal coming from the capsule. Even if the signal is noisy, it seems that a hysteresis in the magnetic moment could be observed in the range between 300 K and 250 K. The fact that the hysteresis does not close completely even at higher temperature might be due to noise or, if real, is not understood.

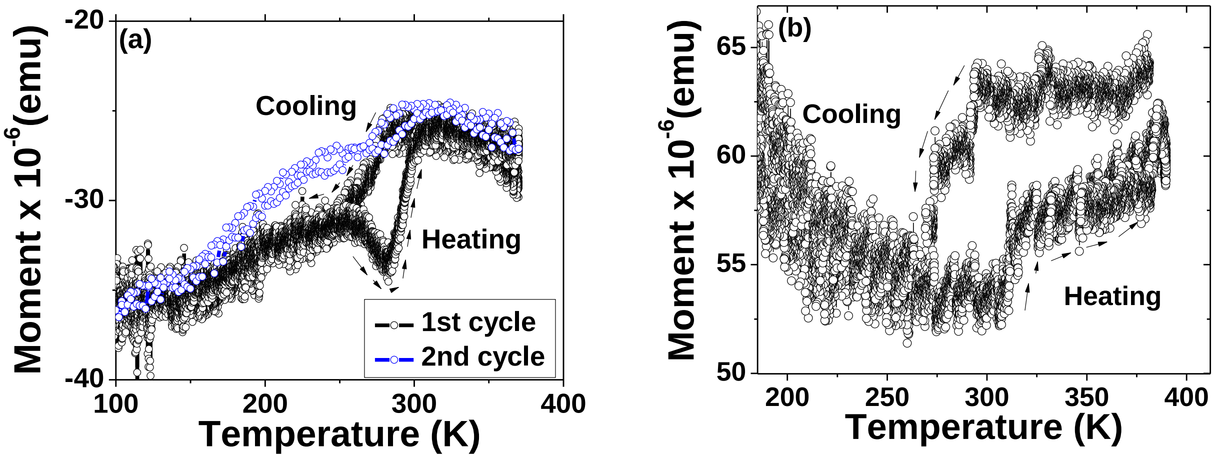

Figure 4.11: (a) Magnetic moment of coordination network's assembly deposited on Si/SiO$_2$ showing the presence of a hysteresis during first thermal cycle which disappeared in the second cycle. (b) Magnetic moment (after diamagnetic correction) of the hybrid network's assembly deposited in the VSM capsule.

4.7 Transport measurements

Transport measurements were performed on the assemblies of coordination and hybrid network deposited on the interdigitated electrodes. Deposition was carried out only by dielectrophoresis in case of coordination networks, while both dielectrophoresis (10 V, 10 kHz) and drop casting were used in case of hybrid assemblies. Asssemblies of coordination network showed resistance in range of 10^9 $^-10^{10}$ Ω at room-temperature. On the other hand, resistance of the hybrid assemblies varied in the range of $10^{5-}10^{10}$ Ω. The conventional way of observing the spin transition in charge transport measurements is to study the variation in current (or resistance) as a function of temperature. As the two states are sought to have different physical properties, a change in conductivity is expected around the transition temperatures. In general, an abrupt or rapid transition can be detected much more easily compared to a gradual transition.

Already, with the magnetic measurements, we realized that the transition in our system could be gradual or rapid depending on the quantity of the solvent present in the sample. However, controlling the solvent during transport measurements could not be performed. Thus, after deposition, assemblies were placed in the cryostat for measuring current-temperature cycles. The temperature regime over which these cycles were performed varied from electrode to electrode. We shall first present these studies in assemblies of coordination networks and then move to the assemblies of hybrid network.

(a) Coordination networks

As mentioned previously, assemblies of coordination networks were found to be highly resistive at room-temperature (of the order of ~10^{10} Ω), and needed a typical voltage around 10 V in order to obtain a measureable current and an acceptable noise to signal ratio. Results are shown in Figure 4.12. Thermal hysteresis was observed in the current in temperature range of 300 K to 260 K with some particular characteristics observed during heating and cooling cycles. For example, on cooling, the current in the assemblies decreased between 300 K and 260 K, with a small upward kink, as shown in Figure 4.12 (a). It is worth noting that for highly resistive electrode 3, current did not show any significant decrease during cooling curve, however, the kink could be observed. During heating, the current in the assemblies increased by more than three order of magnitude around 260 K followed by a same order of decrease around 300 K [see Figure 4.12(b)]. This resulted in a hysteresis in the thermal cycles of current in the temperature regime between 300 K and 260 K, as shown in Figure 4.12(c).

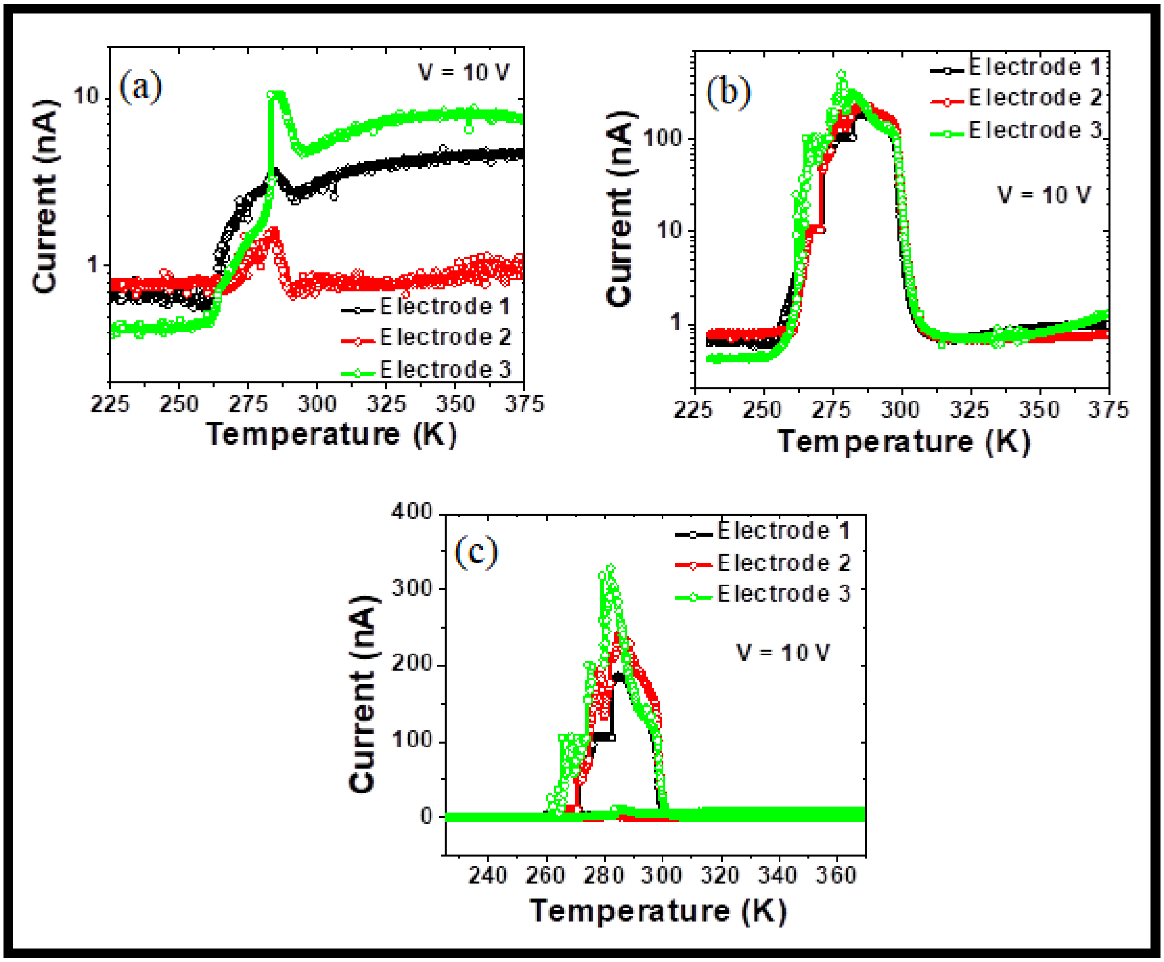

Figure 4.12: (a) Cooling cycle showing a small kink, (b) heating cycle showing a large kink and (c) complete thermal cycle showing the occurrence of hysteresis in the temperature regime where the transition is expected in the coordination network.

Hysteresis in thermal cycles of current has been reported previously where the low-spin state of the SCO complex was found to be more conducting [1]. However, in our case what we observe is more an *increase of current during the transition* rather than a large difference of current between the high-spin and the low-spin state. This increase is huge in the low-spin to high-spin transition and moderate in the opposite direction. We shall discuss more about these results in the later section.

(b) Hybrid network

Transport measurements were performed also on several assemblies of hybrid networks. In these assemblies, room-temperature resistance varied in the range of 10^5 to 10^{10} Ω for different assemblies, and a voltage ranging between few tenths of a volt up to 2 V was applied to observe the current in the range of few nA to few hundred nA.

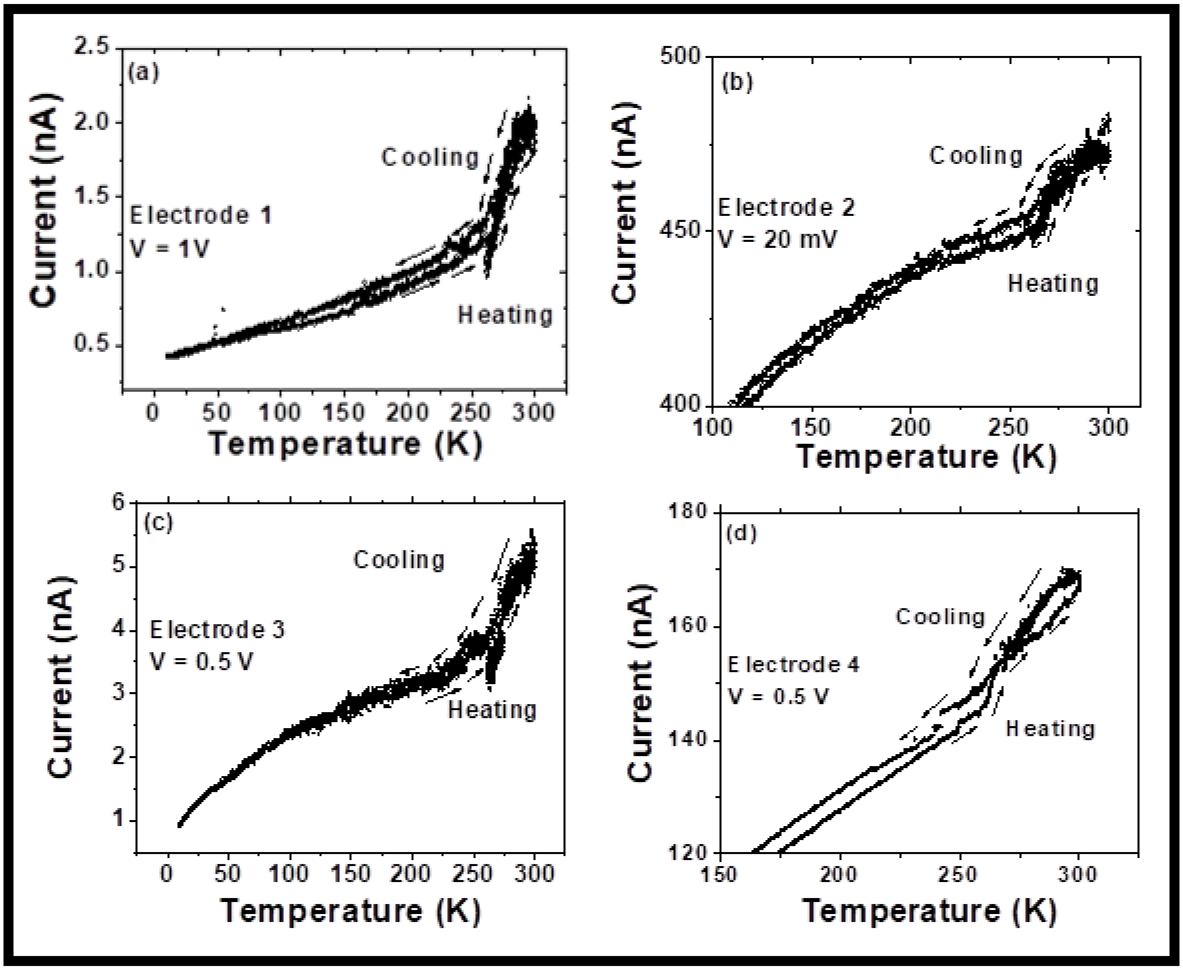

Figure 4.13: (a) Current-temperature cycles below 300 K showing a change in slope near 250 K.

Thermal cycles from 300 K and below: On decreasing (increasing) the temperature, a sharp decrease (increase) in current was observed in 4 out of the 6 measured electrodes between 300 K and 250 K. Below 250 K, the slope of the current changed where it decreased rather gradually at low temperatures. The two other electrodes showed rather monotonous decrease in current corresponding to simple Coulomb blockade behavior. Decrease in current at low temperature is a typical characteristic of nanostructure assemblies and can arise due to the less thermal energy available to overcome the charging energy. However, it would not explain the sharp decrease (increase) in current during cooling (heating) cycle observed near 250 K. Current-temperature curves for these electrodes are shown in Figure 4.13. During the measurements, the temperature was swept at the rate of 1 K per minute.

In another experiments, a hysteresis was observed in the current-temperature curve when the temperature was swept at 3 K per minute as shown in Figure 4.14 (a) and (b). We realized that faster sweeping rate may result in a temperature lag which may give rise to a hysteresis in the current-temperature cycles. Nevertheless, a change in slope is not expected due to higher sweeping rate.

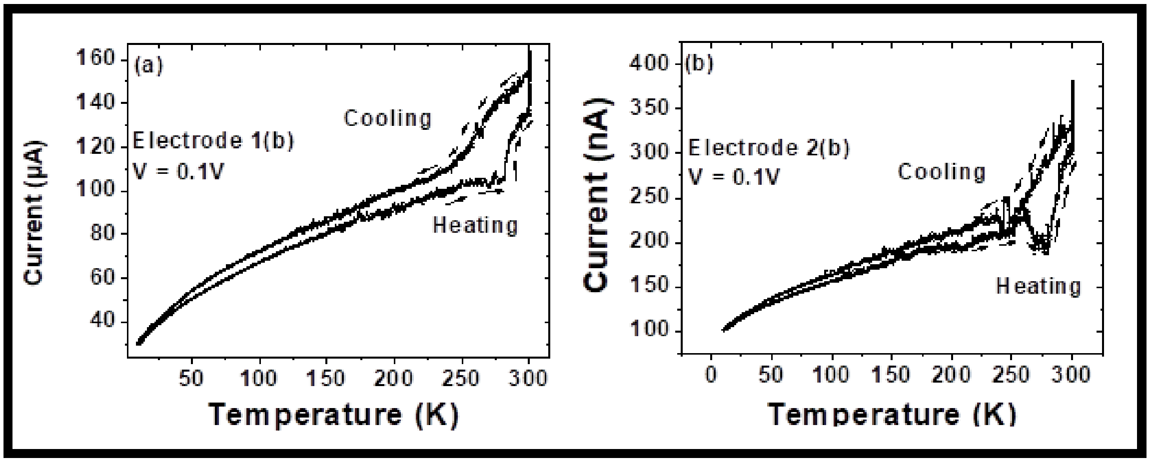

Figure 4.14: Hysteresis in the current-temperature curve observed when the sweeping rate of temperature is higher (3 K per minute).

Thermal cycles from 390 K and below: To observe the behavior of current above 300 K, we increased the temperature of the assemblies which caused the current to increase significantly. Figure 4.15 shows the increase in current at 390 K during the two hours waiting time. Thermal cycles performed after heating showed different behavior as we shall discuss here. We consider here a few interesting cases observed after heating of assemblies, which are shown in Figures 4.16 (a), (b), and (c).

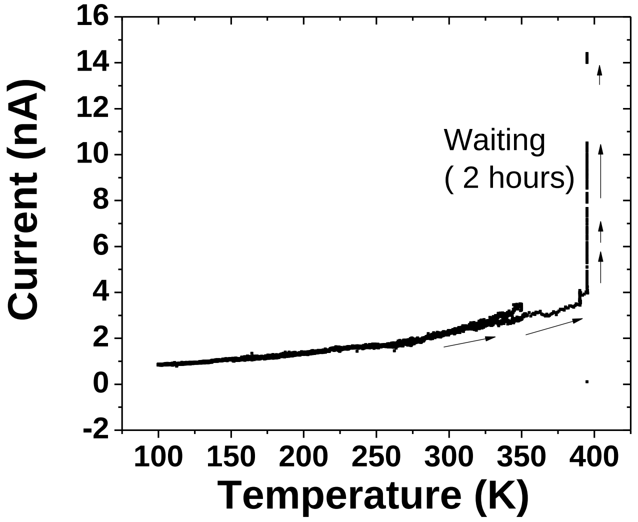

Figure 4.15: Current-temperature curve for an electrode showing a slow increase in current when the temperature is stabilized at 390 K for two hours.

Figure 4.16 (a) shows the thermal cycle of one of the electrode measured after heating up to 390 K. During cooling, a sharp decrease in current could be observed in the range of 300 K to 275 K. Below this temperature no significant decrease in current took place. On the other hand, current did not increased back during the heating cycle, and showed a small kink near 280 K. At the end of the cycle at 390 K, current remained much lower compared to the initial value. However, on typical waiting of 90 minutes at 400 K, current increased slowly to its initial value. The subsequent cycles showed similar behavior.

Figure 4.16 (b) shows the thermal cycles of another electrode after heating up to 390 K. Here also, an abrupt decrease in current was observed near 300 K during the cooling cycle. During the heating cycle, current increased gradually and then abruptly attained its previous value near 370 K. During the second cooling, similar drop in current was observed near 300 K, which was somewhat gradual compared to the first cycle. However, on heating, current showed almost no increase even at higher temperature resulting in an open wide hysteresis. After typical waiting time of two hours at 400 K, no significant increase in current was observed. During the third cycle, current value remained significantly lower and no hysteresis or sharp drops in current were observed.

Figure 4.16 (c) show current temperature cycle of another electrode which also showed large decrease in current around 300 K during cooling, and gradual incomplete cycle up to 400 K during heating. After typical waiting time of 90 minutes at 390 K, the current gradually attained a value close to the previous value. Similar behavior was observed during the second cycle with slightly diminished hysteresis.

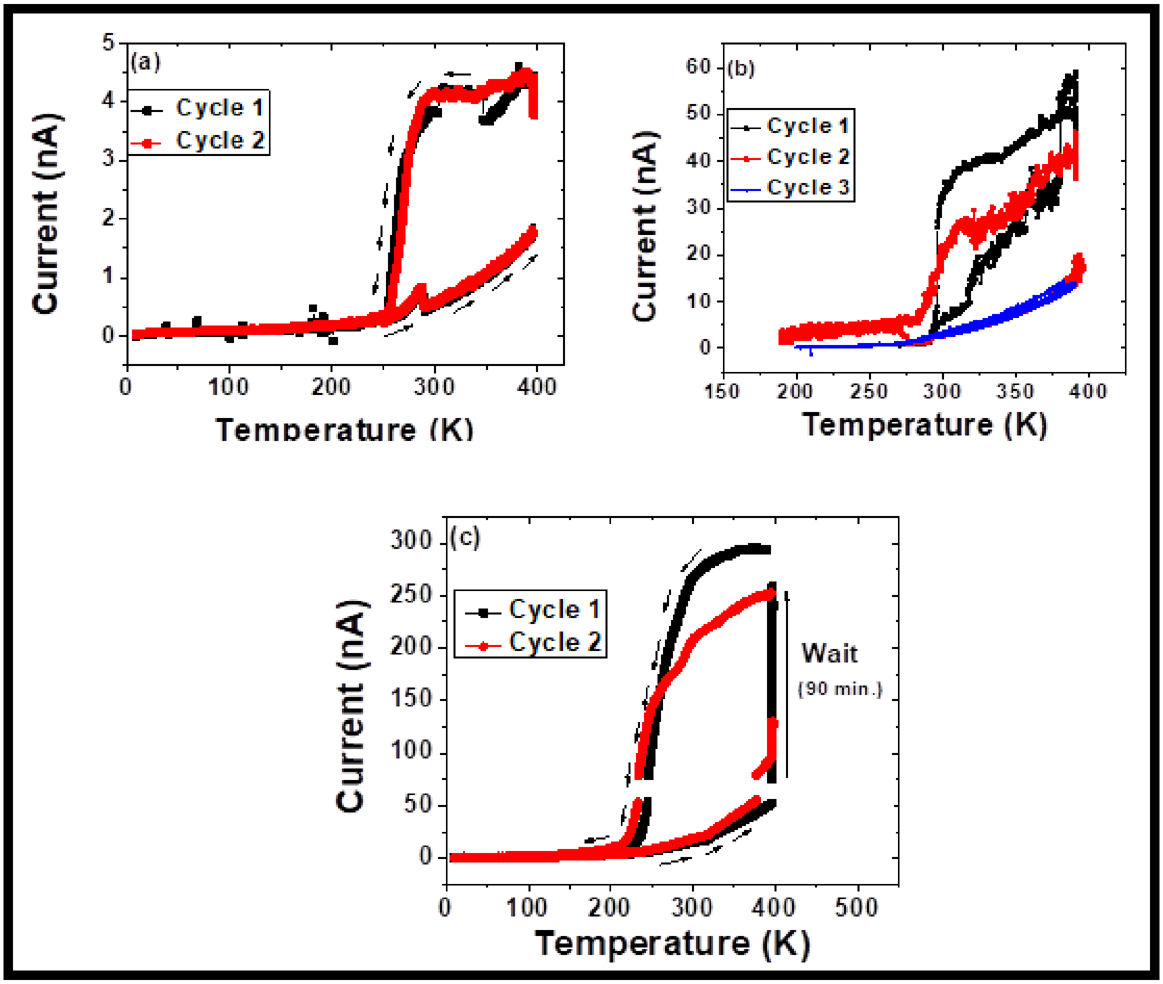

Figure 4.16: Typical thermal cycles observed after heating the assemblies. (a) Hysteresis closed at 400 K only after waiting for 1 to 2 hours. (b) Hysteresis closed abruptly at higher temperature during the first cycles but remain wide open during the second cycle. No hysteresis was observed during the third cycle (c) Diminishing of hysteresis during the second cycle observed in an assembly.

The thermal cycles performed in the temperature range 300 K and below did not show such a large hysteresis. It appears only after heating the assemblies up to 400 K. Nonetheless, a sharp changes in the conductivity could be seen during the cooling cycles. The different behavior before and after heating the assemblies suggests that there might be some changes occurring in the assemblies as a consequence of the heating. We hypothesized that such changes could come from escaping of solvent from the assembly which might be trapped between the particles during the deposition.

4.8 Comparison between magnetic and transport properties

Magnetic measurements revealed that a complete and rapid spin transition can be observed in our coordination network provided that the solvent is present in optimum quantity. For hybrid network, a rapid and incomplete transition could be observed in the temperature range of 300 K to 250 K. In charge transport measurements, we observed some uncommon behavior such as sudden increase in current in 250 K -300 K temperature range for coordination network. For hybrid network, current increased with temperature much steeply in this temperature range. While the magnetic measurements provide direct evidence of spin transition, changes in charge transport properties cannot be considered as the direct evidence. Nevertheless, magnetic measurements can be used to support the reflection of spin transition in charge transport studies. Figure 4.17 shows the $\chi_m T$ curve for the coordination network (measured in gel form) and the current-temperature curve measured in one of the assembly. In temperature regime of 300 K to 250 K, a clear spin transition could be observed in the magnetic measurements. On the other hand, charge transport measurements show some unusual behavior. During the heating cycle, an abrupt increase in current takes place near 260 K. At nearly the same temperature, spin transition from low spin to high spin starts. The current then decrease abruptly near 300 K which is also the end of transition phenomenon as observed in magnetic measurements. However such a high jump in current is not observed during the cooling cycle.

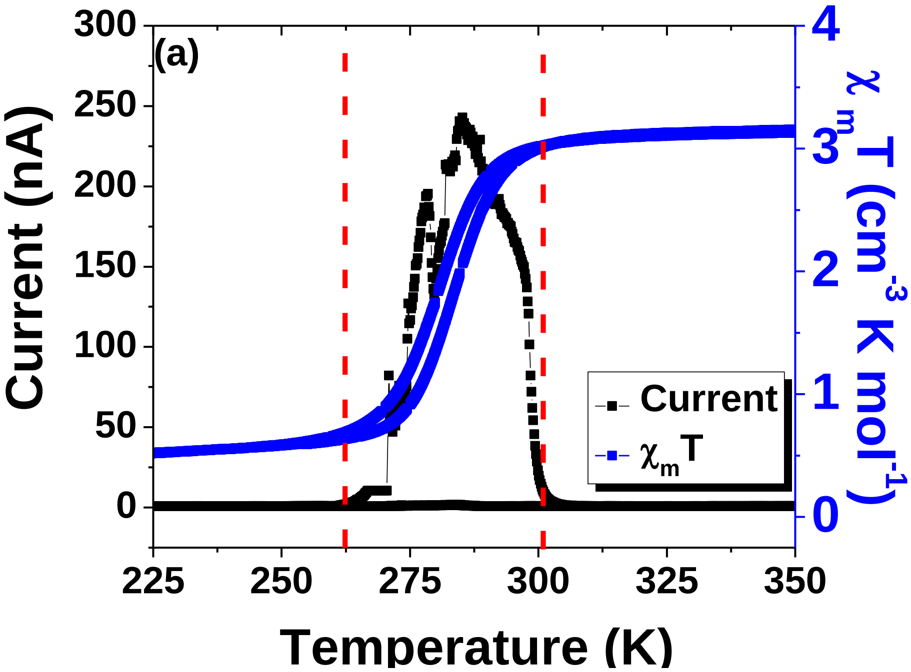

Figure 4.17: Variation in $\chi_m T$ and current as a function of temperature for coordination network. Magnetic measurements were performed in the gel form of the sample while the charge transport was measured on the assembly deposited between interdigitated electrodes.

Such a jump in the current cannot be explained on the basis of difference in conductivity between the two spin states.

Recently, composite materials of a different SCO micro-particles and cellulose fibers have been studied by our collaborative team at *LCC*. In their study, they have observed that coefficient of linear expansion and discharge current show peaks near the transition temperature of SCO [6] as shown in Figure 4.18 (a) and (b). In a different composite material they have observed peaks in the loss modulus appearing near the transition temperature [7] as shown in Figure 4.18(c). These studies indicate that spin transition in composite materials could have certain effects that might appear only near the transition temperature.

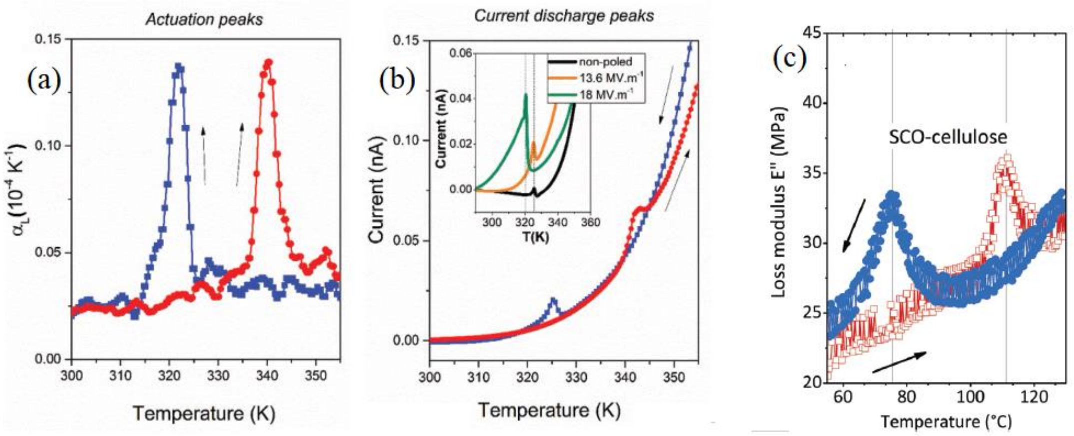

Figure 4.18: Thermal cycles of different SCO composite materials showing peaks in (a) linear expansion coefficient, (b) discharge current, and (c) loss modulus. These peaks appear near the transition temperature of the SCO complexes. [(a) and (b): Reference [6], (c) : Reference [7]].

In our case, despite of completely different system, some analogy could be made. The large changes in current near the transition temperature could be associated with the spin transition. Although, further studies would be required to approve that such hysteretic behavior is associated with spin transition, still, a possible hypothesis could be made if this were to be the case. We hypothesize that certain mixed fraction of high spin and low spin state could be more conducting than solely high or low spin state in the sample. This could explain the behavior of current observed during the heating cycle. For example, when the transition temperature is reached during heating cycle, the fraction of high spin state would start to rise, and a mixed fraction of high and low spin states will exist during the transition process. As per our hypothesis, the sample would remain in conducting state as long as this mixed state exists. This could explain the increase in current near 260 K as well as the drop near 300 K.

In an another hypothesis, such an effect can be visualised as the doping effect in semi-conductors where the inclusion of an impurity can increase the conductivity. For example, high spin state can be considered as a dopant impurity which increase the conductivity of the low spin state during the heating cycle. As the fraction of impurity (high spin state) increases beyond certain fraction, the conductivity drops down. Again, such a hypothesis does not explain the increase in current only during the heating cycle (and not during the cooling), and further explanation would be required.

On the other hand, magnetic measurement and charge transport measurements of hybrid network show similar behavior. While the $\chi_m T$ decreases rapidly from 300 K to 250 K in magnetic measurements, current also show a relatively sharp decrease in roughly the same temperature regime as shown in Figure 4.19. Such changes in conductivity can arise due to several factors. Different charge transport mechanism such as sequential tunneling and co-tunneling could result in changes in current-temperature slope. However, we discard this hypothesis because such a mechanism shift should take place at rather low temperature instead of near-room temperature. Besides, shifting from one mechanism to another takes place rather gradually over a range of temperature. In our case, we have observed a sharp change in the current near 250 K. So far the most likely explanation of the observed transport behavior comes from the spin transition process where the current follows the same behavior as magnetic moment in magnetic measurements. If we allow ourselves to consider this be the actual case, then high spin state could be the more conducting state in our case.

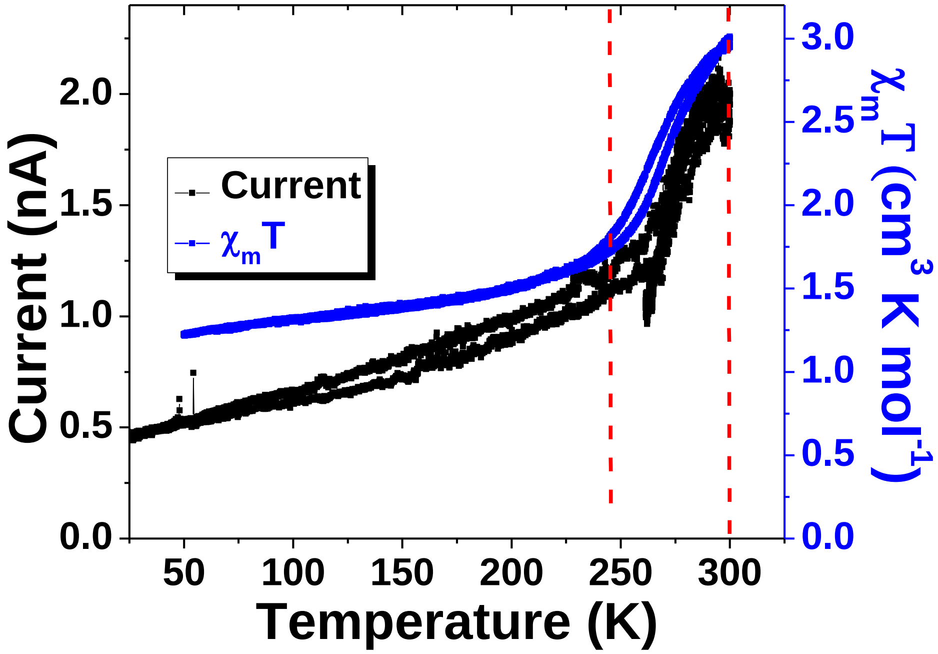

Figure 4.19: Variation in $\chi_m T$ and current as a function of temperature for hybrid coordination network. The magnetic measurements were performed in the gel form of the sample while the charge transport was measured on the assembly deposited between interdigitated electrodes. Remarkable resemblance can be noticed in transport and magnetic behavior of the hybrid network.

4.9 Conclusion

In conclusion, we have studied spin transition in triazole based Fe(II) coordination network and its hybrid network with platinum nanoparticles. TEM images showed that there might be some interaction between the particle and the coordination network which could result in auto-organization of the particles in the assemblies of hybrid network. Coordination network showed a solvent dependent spin transition where a rapid and complete transition could occur in the presence of an optimum quantity of solvent. Higher and lower quantities of the solvent may lead to gradual transition and incomplete transition. On the other hand, completely dried coordination network does not show spin transition in magnetic measurements. For hybrid network, it remained further difficult to observe the transition. However, in certain samples we could observe the transition in magnetic measurements. The different transition behavior from sample to sample is attributed to the quantity of solvent present in the sample. No sign of spin transition was observed in dried form of any of the network.

Charge transport properties of coordination network show some new type of behavior where a more conducting state prevailed in temperature range of 250 K to 300 K only during the heating cycle. Further studies are required to explain such a phenomenon. On the other hand, charge transport properties of the hybrid network show a sharp increase (decrease) in current during heating (cooling) cycles in approximately the same temperature regime where the spin transition is observed in magnetic measurements. Due to the absence of any potential reason of such behavior, and a strong similarity with the magnetic measurements, a highly probable scenario could be the role of spin transition in changing the conductivity of hybrid network assemblies near 250 K.

References: Chapter 4- Spin transition in Fe (II) complex and Pt nanoparticle- Fe(II) complex hybrid nanostructure.

[1] A. Rotaru *et al.*, "Nano-electromanipulation of Spin Crossover Nanorods: Towards Switchable Nanoelectronic Devices," *Advanced Materials,* vol. 25, no. 12, pp. 1745-1749, 2013.

[2] A. Rotaru, I. y. A. Gural'skiy, G. Molnar, L. Salmon, P. Demont, and A. Bousseksou, "Spin state dependence of electrical conductivity of spin crossover materials," *Chemical Communications,* 10.1039/C2CC30528C vol. 48, no. 35, pp. 4163-4165, 2012.

[3] H. J. Shepherd *et al.*, "Molecular actuators driven by cooperative spin-state switching," *Nature Communications,* Article vol. 4, p. 2607, 10/24/online 2013.

[4] O. Kahn and C. J. Martinez, "Spin-Transition Polymers: From Molecular Materials Toward Memory Devices," *Science,* 10.1126/science.279.5347.44 vol. 279, no. 5347, p. 44, 1998.

[5] E. J. Devid *et al.*, "Spin Transition in Arrays of Gold Nanoparticles and Spin Crossover Molecules," *ACS Nano,* vol. 9, no. 4, pp. 4496-4507, 2015/04/28 2015.

[6] S. Rat, M. Piedrahita-Bello, L. Salmon, G. Molnár, P. Demont, and A. Bousseksou, "Coupling Mechanical and Electrical Properties in Spin Crossover Polymer Composites," *Advanced Materials,* pp. 1705275-n/a, Art. no. 1705275.

[7] S. Rat *et al.*, "Elastic coupling between spin-crossover particles and cellulose fibers," *Chemical Communications,* 10.1039/C6CC06137K vol. 52, no. 75, pp. 11267-11269, 2016.

Conclusion

In conclusion, we have studied simple charge transport and magneto-transport in assemblies of different types of nano-structures. These nano-structures include chemically prepared (i) platinum particles coated with different alkyl and aryl thiols, (ii) magnetic particles of $Fe_{50}Co_{50}$ coated with HDA/HCl ligand, and (iii) triazole based Fe (II) coordination network and its hybrid network with platinum nanoparticles. The research performed during this thesis has shed light on various aspects of charge transport in these mentioned systems. At the same time, it has given rise to some new questions as well.

Firstly, we have shown that using chemical routes, systems with room-temperature Coulomb blockade properties can be prepared. We proposed the use of aryl ligands for coarse tuning of Coulomb blockade as they show significant changes in the non-linearity of the *I-V* curves on varying the substituent group at their para position. For the fine tuning of Coulomb blockade, alkyl ligands could be the better choice for small particles in the range of 1 – 2 nm. However, measuring such small changes may require large statistical data to observe any trend. Beside, we have seen some correlation between the estimated charging energy and the scaling exponent of the assembly. Theoretical studies may bring some new information about such a correlation.

On the other hand, FeCo particles have proven to be of better quality than the ones used in previous studies at LPCNO. They have been synthesized by improved chemical routes and ehxbit no problems arising due to the presence of carbon in the nanoparticles. This is evident from the TMR behavior in their assembly which could last up to ~0.5% at room-temperature and varied from ~3 to 11% at low temperature. This is a boost for further improving the quality of particles to reach even higher TMR ratios. Not only have we observed the TMR in assemblies of FeCo particles but also the potential mode of charge transport in their assembly at high and low temperature regimes. At high temperatures (above 70 K to 200 K) sequential tunneling prevails where no voltage dependency of TMR amplitude is observed. At low temperatures, presence of co-tunneling could significantly enhance the TMR amplitude. However, a new aspect of co-tunneling has been shown. We have observed a fairly good correlation between co-tunneling event (by measuring the number of junctions involved in the co-tunneling event) and TMR amplitude. However, we have observed some uncommon behavior related to the voltage dependency of TMR and co-tunneling. Our results suggest that the extent of co-tunneling could decrease at low voltages which could also affect the TMR amplitude. Experimental results should be reproduced in other systems. We suggest magnetic particles of even smaller size (than 10 nm) for an extended co-tunneling regime. On the other hand, theoretical investigation would equally be required to find the possible explanations of inverse co-tunneling behavior.

The methods used to prepared the sample could be an important factor in determining the range of temperature over which co-tunneling should prevail. Our results on assemblies prepared by dielectrophoresis and drop casting reveal a lower extent of co-tunneling in samples prepared by dielectrophoresis. This opens up several questions that need to be investigated. First, is the role of the dimension of the assembly Co-tunneling studies should be performed on assemblies with varyingdimension so as to find out how the dimension of an assembly affect the co-tunneling event. Second, whether the inter-particle coupling between be tuned with dielectrophoresis. Our analysis of assemblies prepared by dielectrophoresis shows that relatively higher inter-particle coupling prevails in samples prepared by dielectrophoresis.

At significantly low temperatures (~1.8 K), a high field negative MR is observed just above the saturation field of the assemblies, which could show a maximum of -16% amplitude. At slightly higher temperature (~2.5 K) this MR is accompanied by another high field MR which occurs at even higher field and show positive behavior i.e. decrease in resistance with field. Both the MR vanishes with increase in temperature and voltage. Similar results have been observed at LPCNO on the assemblies of FeCo superlattices and assemblies. Beside, a non-saturating TMR up to 3T has been also reported in assemblies of Fe particles. Such a high field MR is often attributed to the presence of paramagnetic impurities in the barrier.

Our study on Fe (II) coordination network and its hybrid structure has given new hope to this class of materials. We have successfully observed the transition in the coordination network in the form of gel which manifests a steep transition, as evident from magnetic measurements, when the solvent quantity is optimum. Charge transport measurements show some interesting features which could be related to the spin transition. For example the sudden increase and decrease in current during the heating cycle could indicate that a mixed state might be more conducting than low or high spin state in the assembly of coordination network. Similar changes in certain properties occurring at transition temperature has been recently reported by our collaborative teams in LCC. For example changes in loss modulus and discharge current in the composite SCO materials have been reported to occur around the transition temperatures. On the other hand, hybrid structure of this network with platinum nanoparticles could show either a gradual or complete transition or a partial and rapid transition. To our knowledge, this is the first time that a steep, though partial, transition has been observed in co-ordination network-metal nanoparticle hybrid nanostructures. However, our studies were limited by the dependency of transition on the solvent present in the sample. It has given a direction to the chemistry, which should prepare systems where the transition in SCO and its hybrid structure could take place without depending on the solvent. Charge transport studies on hybrid network have also shown changes in the conductance near the transition temperature which could be related to the spin transition as supported by magnetic measurements.